The Dissertation Committee for Katherine Amelia Koen Certifies that this is the approved version of the following dissertation:

Sub-diffraction Limited Morphology Characterization in Single Noble Metal Nanoparticles and Single Conjugated Polymer Chains Using Optical Microscopy Techniques

Committee:

David A. Vanden Bout, Supervisor

Katherine A. Willets, Co-Supervisor

Jennifer S. Brodbelt

Alan Campion

Richard M. Crooks

Xiaoqin (Elaine) Li

Sub-diffraction Limited Morphology Characterization in Single Noble Metal Nanoparticles and Single Conjugated Polymer Chains Using Optical Microscopy Techniques

by

Katherine Amelia Koen, B.S.

Dissertation

Presented to the Faculty of the Graduate School of

The University of Texas at Austin

in Partial Fulfillment

of the Requirements

for the Degree of

Doctor of Philosophy

The University of Texas at Austin

May 2015

Dedication

To my family, in blood, science, or bond.

Acknowledgments

First, I would like to thank my advisers and colleagues. Prof. Kallie Willets trained me and gave me confidence with spectroscopy and microscopy early on. Prof. David Vanden Bout has been a font of wisdom, support, and encouragement. It has been my privilege to learn from both of them. Whether I was trained by or trained my fellow Willets and Vanden Bout group members, I learned something from each of you, as well as from my EFRC collaborators. I am particularly grateful to Takuji Adachi, who helped me through a difficult transition with his characteristic positivity and unfailing energy. I admire you, Taki, and appreciate everything you have done for me. It was my pleasure to work with you.

Thank you, friends in Austin and elsewhere, for all of the happy times, and for listening during the unhappy ones.

Thank you, Max Milligan, for being a source of strength, support, joy, and love.

Thank you to my family. Brothers, I loved the "Dr. Katherine Koen" sign photos. Thank you, Jenny and Bryan, for checking on me during crunch time. Thank you all for traveling to celebrate with me. Aunt Sue, thank you for supporting and praying for me. Mom and Dad, I can't thank you enough for all you've done to support my schoolwork and every other aspect of my life over the last ten years. Finally, thank you, Prof. Edna Dudgeon, for knowing the value of an educated woman, and recognizing that both of my parents knew it, too.

Sub-diffraction Limited Morphology Characterization in Single Noble Metal Nanoparticles and Single Conjugated Polymer Chains Using Optical Microscopy Techniques

Katherine Amelia Koen, Ph.D.

The University of Texas at Austin, 2015

Supervisor: David A. Vanden Bout

Co-Supervisor: Katherine A. Willets

At the nanoscale, materials exhibit special properties not present in the bulk, which may be exploited in diverse applications that include catalysis, sensing, and energy harvest and transfer. Due to their small size, nanoscale materials also present a characterization challenge, because optical microscopy techniques cannot resolve images of structural features smaller than finite lenses may focus visible light. Optical images of nanoparticles or single molecules show diffraction-limited spots with radii of approximately half the wavelength of the light used to interrogate them, and the underlying structure of the nanoscale object is not obvious to the eye. Fortunately, manipulation of excitation conditions and image processing techniques can tease out information about the morphology of nanomaterials investigated. The first example presented in this dissertation shows how an asymmetric excitation geometry and polarization spectroscopy elucidate the orientation of single silver triangular nanoprisms in the plane of an optical microscope's stage. Characterizing this orientation using optical microscopy techniques opens possibilities for post-characterization nanoparticle functionalization and improved amplification of surface-enhanced spectroscopy signals.

Electron microscopy may characterize single noble metal nanoparticles if one is unconcerned with those benefits, but electron microscopy investigations are more challenging for soft matter samples, so optical characterization becomes even more appealing for polymer studies. Bias-induced centroid (BIC) spectroscopy, correlated with polarization spectroscopy, reports not only on the distance over which highly ordered single poly[2-methoxy-5-(2'-ethylhexyloxy)-1,4-phenylenevinylene] (MEH-PPV) chains transfer energy, but also that the rod-like structures these polymers are believed to adopt are likely to transfer this energy along their longitudinal axes. BIC relies on observable changes in the position of the fluorescence centroid, but when the bias-induced hole-injection partially quenching the fluorescence occurs symmetrically, the displacement of the fluorescence centroid is small, and defining the displacement direction becomes difficult. In this event, analysis of the ellipticity of the diffraction-limited images of the MEH-PPV fluorescence also supports the conclusion that the polymer transfers energy in the direction of the longitudinal axis of the rod-like structure. Taken together, these wide-field optical techniques allow simultaneous morphological characterization of many single nanoparticles or single polymer chains without appealing to scanning probe or electron microscopies, which can damage the sample or prevent post-characterization modification.

Table of Contents

List of Tables

List of Figures

Chapter 1: Introduction

1.1 NANOSTRUCTURED MATERIALS

Materials exhibit different properties when their overall size or feature sizes are on the nanoscale than they do in larger, or bulk, size scales. Gold, for instance, is called a noble metal because it is almost chemically inert on the macroscale, just as noble gases are chemically inert. As the size of the gold material decreases, however, gold becomes more reactive, even catalyzing a variety of oxidation-reduction (redox) reactions.[1] Gold and silver, another noble metal, have a shiny yellow or shiny grey color in macroscale items like jewelry, but the size and shape of silver nanoparticles determine whether they appear blue, green, or red, for example.[2] These special properties at the nanoscale can be exploited, as in stain-repellent clothing coated in nanostructured polymers, or must be accounted for, as in the increasing importance of quantum tunneling effects as transistor size decreases.[2, 3]

1.1.2 Noble metal nanoparticles

The rainbow of colors one can observe among noble metal nanoparticles arises from the localized surface plasmon resonance (LSPR). Silver and gold are conducting metals whether they are bulk or nanomaterials, which means that the valence electrons are loosely bound to nuclei in a mobile electron gas. In addition to moving freely, the surface conduction electrons in a silver or gold nanoparticle can move collectively in response to excitation with light. The condition under which light excites these collective oscillations most effectively is known as the plasmon resonance, and it is localized because the plasmon is confined to a nanoparticle rather than propagating along a surface. The LSPR phenomenon is not limited to noble metal nanoparticles, but appears in

materials with a negative real and small positive imaginary dielectric constant.[4] At the plasmon resonance, the nanoparticle scatters a particular wavelength of light, λ_{max}, most strongly. For example, if a silver triangular nanoprism has an LSPR at λ_{max} = 650 nm, then it will scatter red light. A vial of silver triangular nanoprisms in water would therefore appear blue-green.

In addition to giving noble metal nanoparticles a characteristic color determined by their size, shape, and material composition, the LSPR enhances electromagnetic fields at the nanoparticle surface by many orders of magnitude.[5-9] Because of the diversity in the shape and size of nanoparticles, single-particle spectroscopy has emerged as an important technique for characterizing individual particles and determining how the LSPR changes as a function of nanoparticle structure.[10-15] Understanding how the shape and size of individual nanoparticles affects the LSPR is important for both LSPR sensing experiments as well as for spectroscopic techniques that take advantage of the local electromagnetic field enhancements around nanoparticles, such as surface-enhanced Raman scattering (SERS).[15-21] The distribution and extent of local electromagnetic field enhancement around nanoparticles used in these sensing and surface-enhanced spectroscopy applications is dictated by their structure.

1.1.3 Conjugated polymers

Another class of materials whose morphology and function are intimately linked are conjugated polymers. Conjugated polymers are attractive for use in organic electronics because of their flexibility[22] and ease of manufacture,[23] but cannot yet compete with inorganic devices in efficiency when converting light to current, or vice versa.[24]

There are several levels of morphology one could investigate in conjugated polymer devices to understand the reasons behind this inefficiency. At the coarsest level, one might investigate the bulk film in a device, but this contains a range of chain morphologies, so the effects of each are convoluted.[25] At the finest level, one might investigate single conjugated polymer chains, and establish the energy transport capabilities in the morphology adopted by each chain. One of the paths by which conjugated polymer-based light-emitting diodes (LEDs) or photovoltaic devices may lose device efficiency is through exciton quenching by hole polarons (p^+). Upon electron transfer from the exciton to the hole polaron, the hole is detrapped and its position changes.[26, 27] The distance scale of this shift is smaller than the diffraction limit of visible light, so observation of exciton quenching by hole polarons or exciton migration in poly[2-methoxy-5-(2-ethylhexyloxy)-1,4-phenylenevinylene] (MEH-PPV) using optical microscopy techniques has either been indirect,[25] or has employed super-resolution microscopy techniques.[28, 29]

1.2 Observation of nanostructured material orientation

1.2.1 Sub-diffraction limited imaging

Observation of morphologies and processes is complicated at the nanoscale. Resolution in optical microscopes is fundamentally limited by the wave nature of light and the finite size of lenses (Ernst Abbe, 1873). The image of a point source will appear as an Airy disk with radius, r (Lord Rayleigh, 1896), according to Equation 1.1,

$$r = \frac{0.61\lambda}{N.A.} \tag{1.1}$$

where λ is the wavelength of the light, and *N.A.* is the numerical aperture of the lens used to collect the image. For visible light, this means that nanoscale objects and features cannot be resolved.

Electron microscopies have been used as an alternative microscopy technique, because electrons can have smaller wavelengths than visible light, and can therefore resolve nanoscale features. Scanning electron microscopy (SEM) and tunneling electron microscopy (TEM) are powerful techniques, but they have some disadvantages. Each characterizes a subset of the nanomaterial population, and requires an assumption or statistical argument that this subset is representative of that population. Once characterized, those specific nanomaterials may not be removed from their electron microscope substrates for further use. Soft matter also presents a challenge when using electron microscopy, because organic materials are likely to char as the electron beam raster scans over the sample.

Scanning probe techniques, such as atomic force microscopy (AFM), have also been used to characterize nanoscale structures. This technique is also typically used to characterize a subset of the nanomaterial population, as it would be too time-consuming to raster scan the entire ensemble. Tip-sample interactions may also bias the scan or damage the sample.

Despite the diffraction limit, optical microscopy is attractive because the resources necessary are more readily available than those for electron or scanning probe microscopies, samples may be characterized and then further functionalized or used, and soft matter samples are at less risk of damage. Observation of nanoscale structure and phenomena using far-field optical microscopy techniques requires point-spread function fitting. The Airy disk image "spread" from a point source is most commonly modeled as a 2-D Gaussian, Equation 1.2.

$$I(x,y) = z_0 + I_0 e^{\left[\frac{-1}{2}\left[\left(\frac{x-x_0}{s_x}\right)^2+\left(\frac{y-y_0}{s_y}\right)^2\right]^2\right]} \quad (1.2)$$

In Equation 1.2, each position (x,y) has an intensity, I, that can be modeled as the sum of the background, z_0, and the product of the peak intensity, I_0, with a Gaussian centered at x_0,y_0 that has a spread in the x-direction of s_x and a spread in the y-direction of s_y. The position of the peak intensity, or centroid, typically shifts positions within frames of an image stack, and these centroid shifts are used to map nanostructures or phenomena. The phenomena mapped may depend on the independent variable modified, like polarization or applied electric potential.

1.2.2 Polarization resolution in optical microscopy techniques

Polarization is an important variable for understanding how the shape of the nanoparticle dictates the measured LSPR and SERS response.[10-12, 14, 20, 30-36] For example, rod-shaped nanoparticles support two plasmon modes: the transverse mode, which is excited along the short axis of the rod, and the longitudinal mode, which is excited along the long axis of the rod.[37, 38] Exciting the rod with light polarized along the long axis will generate higher overall signals in the measured scattering spectrum, which improves the signal-to-noise in a sensing assay. Similar results can be obtained for other highly anisotropic structures such as spherical dimers, bipyramids, or asymmetrically truncated triangles.[17, 39-41] Thus, polarization-resolved single-nanoparticle LSPR studies are important for revealing local heterogeneity and orientation within diverse nanoparticle populations.

Polarization anisotropy measurements report on the degree to which an object behaves like a dipole, and on that "dipole's" orientation in the *x*–*y* plane.[42] This can be applied to noble metal nanoparticles and to single polymer chains. In the case of nanoparticles investigated in this dissertation, the light intensity arises from plasmon-mediated Rayleigh scattering. In MEH-PPV chains, the light intensity arises from fluorescence.

In polarization anisotropy experiments, the electric field of the excitation beam is rotated in the plane of the stage of the microscope (the *x*–*y* plane), and the resulting modulation in the emission signal of excited objects is observed. In this case, fluorescence arising from single MEH-PPV molecules is modulated in response to the alignment of the excitation polarization with the projection of the molecule's net dipole into the *x*–*y* plane. When the two are parallel, a maximum in fluorescence intensity is observed, and when the two are orthogonal, a minimum in fluorescence intensity is observed. By a process described in Chapter 2, polarization anisotropy experiments reveal the orientation of the projection of each molecule's net dipole in the *x*–*y* plane, as well as the degree to which the behavior of the molecule approximates a perfect dipole or an isotropic object. The structure of high molecular weight MEH-PPV has been modeled as highly anisotropic to fit polarization anisotropy experiment data.[43] According to these models, one could reasonably expect the phase angle determined from polarization anisotropy experiments to approximate the angle at which the polymer backbone of an MEH-PPV molecule was oriented in the *x*–*y* plane.

The fluorescence intensity response of each single molecule to rotating excitation polarization was fit to a $\cos(2\theta)$ function (Equation 1.3) using MATLAB scripts written in-house.

$$I = \frac{I_{max}+I_{min}}{2} - \frac{I_{max}-I_{min}}{2}(\cos 2(\theta - \phi)) \quad (1.3)$$

The phase angle, ϕ, is the angle at which the net dipole moment of the molecule was best aligned with the excitation polarization, and the angle orthogonal to ϕ in the same plane is the angle of excitation polarization that produces the least fluorescence intensity.

1.2.3 Electro-optical microscopy

In addition to reporting on nanostructure and orientation, super-resolution microscopy techniques can map nanoscale phenomena by observing the centroid shift in response to changes in an independent variable, such as applied electric potential.

Bias-modulated intensity-centroid spectroscopy (BIC) experiments previously undertaken in the Barbara group revealed long-range energy transport after the reversible injection of a single hole into an MEH-PPV chain, which suggested an extended or rod-like conformation for that molecular weight.[44] These super-resolution microscopy studies sometimes showed a fluorescence centroid trajectory that did not trace a single straight line, an unexpected result for a rod-like polymer conformation. Correlating these experiments with polarization anisotropy experiments allows us to map energy transfer in different morphologies adopted by MEH-PPV chains.

Applied electric potential may also be manipulated to report on nanoscale phenomena in optical microscopy techniques that do not use point-spread function fitting. In Appendix A, we report on in-device fluorescence voltage spectroscopy (ID-FVS), a technique to evaluate photovoltaic behavior and charge trapping in hybrid organic-inorganic solar cell prototype devices.

1.3 REFERENCES

1. Freakley, S.; He, Q.; Kiely, C.; Hutchings, G., Gold Catalysis: A Reflection on Where We are Now. *Catal Lett* **2015,** *145* (1), 71-79.
2. Liz-Marzán, L. M., Tailoring Surface Plasmons through the Morphology and Assembly of Metal Nanoparticles. *Langmuir* **2006,** *22* (1), 32-41.
3. Collaert, N.; Alian, A.; Arimura, H.; Boccardi, G.; Eneman, G.; Franco, J.; Ivanov, T.; Lin, D.; Loo, R.; Merckling, C.; Mitard, J.; Pourghaderi, M. A.; Rooyackers, R.; Sioncke, S.; Sun, J. W.; Vandooren, A.; Veloso, A.; Verhulst, A.; Waldron, N.; Witters, L.; Zhou, D.; Barla, K.; Thean, A. V. Y., Ultimate nano-electronics: New materials and device concepts for scaling nano-electronics beyond the Si roadmap. *Microelectronic Engineering* **2015,** *132* (0), 218-225.
4. Willets, K. A.; Van Duyne, R. P., Localized Surface Plasmon Resonance Spectroscopy and Sensing. *Annual Review of Physical Chemistry* **2007,** *58* (1), 267-297.
5. Angulo, A. M.; Noguez, C.; Schatz, G. C., Electromagnetic Field Enhancement for Wedge-Shaped Metal Nanostructures. *J. Phys. Chem. Lett.* **2011,** *2* (16), 1978-1983.
6. Hao, E.; Schatz, G. C., Electromagnetic fields around silver nanoparticles and dimers. *J. Chem. Phys.* **2004,** *120* (1), 357-366.
7. Kolloch, A.; Benner, D.; Baedicker, M.; Waitz, R.; Geldhauser, T.; Boneberg, J.; Leiderer, P.; Scheer, E., Characterization and applications of plasmon fields in metal nanostructures. *Proc. SPIE 8204*, 820404-820404-10.
8. Kleinman, S. L.; Bingham, J. M.; Henry, A.-I.; Wustholz, K. L.; Van Duyne, R. P., Structural and optical characterization of single nanoparticles and single molecule SERS. *Proc. SPIE* **2010,** *7757* (Plasmonics: Metallic Nanostructures and Their Optical Properties VIII), 77570J/1-77570J/10.
9. Wokaun, A., Surface-enhanced electromagnetic processes. *Solid State Phys.* **1984,** *38*, 223-94.
10. Chen, H. J.; Shao, L.; Woo, K. C.; Ming, T.; Lin, H. Q.; Wang, J. F., Shape-Dependent Refractive Index Sensitivities of Gold Nanocrystals with the Same Plasmon Resonance Wavelength. *J. Phys. Chem. C* **2009,** *113* (41), 17691-17697.
11. Slaughter, L.; Chang, W.-S.; Link, S., Characterizing Plasmons in Nanoparticles and Their Assemblies with Single Particle Spectroscopy. *J. Phys. Chem. Lett. 2* (16), 2015-2023.
12. Guo, H.; Ruan, F.; Lu, L.; Hu, J.; Pan, J.; Yang, Z.; Ren, B., Correlating the Shape, Surface Plasmon Resonance, and Surface-Enhanced Raman Scattering of Gold Nanorods. *J. Phys. Chem. C* **2009,** *113* (24), 10459-10464.
13. Hao, E.; Schatz, G. C.; Hupp, J. T., Synthesis and optical properties of anisotropic metal nanoparticles. *J. Fluoresc.* **2004,** *14* (4), 331-341.
14. Seney, C. S.; Gutzman, B. M.; Goddard, R. H., Correlation of Size and Surface-Enhanced Raman Scattering Activity of Optical and Spectroscopic Properties for Silver Nanoparticles. *J. Phys. Chem. C* **2009,** *113* (1), 74-80.

15. Tiwari, V. S.; Oleg, T.; Darbha, G. K.; Hardy, W.; Singh, J. P.; Ray, P. C., Non-resonance SERS effects of silver colloids with different shapes. *Chem. Phys. Lett.* **2007,** *446* (1-3), 77-82.
16. Brus, L., Noble metal nanocrystals: plasmon electron transfer photochemistry and single-molecule Raman spectroscopy. *Acc Chem Res* **2008,** *41* (12), 1742-9.
17. Dadosh, T.; Sperling, J.; Bryant, G. W.; Breslow, R.; Shegai, T.; Dyshel, M.; Haran, G.; Bar-Joseph, I., Plasmonic Control of the Shape of the Raman Spectrum of a Single Molecule in a Silver Nanoparticle Dimer. *ACS Nano* **2009,** *3* (7), 1988-1994.
18. Kleinman, S. L.; Bingham, J. M.; Henry, A.-I.; Wustholz, K. L.; Van, D. R. P., Structural and optical characterization of single nanoparticles and single molecule SERS. *Proc. SPIE 7757* (Plasmonics: Metallic Nanostructures and Their Optical Properties VIII), 77570J/1-77570J/10.
19. Kleinman, S. L.; Bingham, J. M.; Henry, A.-I.; Wustholz, K. L.; Van Duyne, R. P. In *Structural and optical characterization of single nanoparticles and single molecule SERS*, Plasmonics: Metallic Nanostructures and Their Optical Properties VIII, San Diego, California, USA, SPIE: San Diego, California, USA, pp 77570J-10.
20. Slaughter, L. S.; Chang, W. S.; Swanglap, P.; Tcherniak, A.; Khanal, B. P.; Zubarev, E. R.; Link, S., *J. Phys. Chem. C* **2010,** *114*, 4934.
21. Rycenga, M.; Camargo, P. H. C.; Li, W.; Moran, C. H.; Xia, Y., Understanding the SERS Effects of Single Silver Nanoparticles and Their Dimers, One at a Time. *J. Phys. Chem. Lett. 1* (4), 696-703.
22. Minaev, B.; Baryshnikov, G.; Agren, H., Principles of phosphorescent organic light emitting devices. *Physical Chemistry Chemical Physics* **2014,** *16* (5), 1719-1758.
23. Kreis, J.; Schwambera, M.; Keiper, D.; Gersdorff, M.; Long, M.; Heuken, M. In *Carrier-gas enhanced vapor phase deposition for organic thin films: addressing mass manufacturing requirements for OLED devices, and overcoming existing challenges with OVPD*, 2013; pp 88291C-88291C-11.
24. Green, M. A., Third generation photovoltaics: Ultra-high conversion efficiency at low cost. *Progress in Photovoltaics: Research and Applications* **2001,** *9* (2), 123-135.
25. Markov, D. E.; Amsterdam, E.; Blom, P. W. M.; Sieval, A. B.; Hummelen, J. C., Accurate Measurement of the Exciton Diffusion Length in a Conjugated Polymer Using a Heterostructure with a Side-Chain Cross-Linked Fullerene Layer. *The Journal of Physical Chemistry A* **2005,** *109* (24), 5266-5274.
26. Bolinger, J.; Lee, K.-J.; Palacios, R. E.; Barbara, P. F., Detailed Investigation of Light Induced Charge Injection into a Single Conjugated Polymer Chain. *The Journal of Physical Chemistry C* **2008,** *112* (47), 18608-18615.
27. Salleo, A.; Street, R. A., Light-induced bias stress reversal in polyfluorene thin-film transistors. *Journal of Applied Physics* **2003,** *94* (1), 471-479.
28. Habuchi, S.; Onda, S.; Vacha, M., Mapping the emitting sites within a single conjugated polymer molecule. *Chemical Communications* **2009,** (32), 4868-4870.
29. Bolinger, J. C.; Traub, M. C.; Adachi, T.; Barbara, P. F., Ultralong-Range Polaron-Induced Quenching of Excitons in Isolated Conjugated Polymers. *Science* **2011,** *331* (6017), 565-567.

30. Angulo, A. M.; Noguez, C.; Schatz, G. C., Electromagnetic Field Enhancement for Wedge-Shaped Metal Nanostructures. *J. Phys. Chem. Lett. 2* (16), 1978-1983.
31. Haran, G., Single-Molecule Raman Spectroscopy: A Probe of Surface Dynamics and Plasmonic Fields. *Acc. Chem. Res. 43* (8), 1135-1143.
32. Haynes, C. L.; Van, D. R. P., Nanosphere Lithography: A Versatile Nanofabrication Tool for Studies of Size-Dependent Nanoparticle Optics. *J. Phys. Chem. B* **2001,** *105* (24), 5599-5611.
33. Jain, P. K.; Lee, K. S.; El-Sayed, I. H.; El-Sayed, M. A., Calculated absorption and scattering properties of gold nanoparticles of different size, shape, and composition: Applications in biological imaging and biomedicine. *Journal of Physical Chemistry B* **2006,** *110* (14), 7238-7248.
34. Kelly, K. L.; Coronado, E.; Zhao, L. L.; Schatz, G. C., The optical properties of metal nanoparticles: The influence of size, shape, and dielectric environment. *Journal of Physical Chemistry B* **2003,** *107* (3), 668-677.
35. Mulvihill, M. J.; Ling, X. Y.; Henzie, J.; Yang, P., Anisotropic Etching of Silver Nanoparticles for Plasmonic Structures Capable of Single-Particle SERS. *J. Am. Chem. Soc. 132* (1), 268-274.
36. Sonnichsen, C.; Geier, S.; Hecker, N. E.; von, P. G.; Feldmann, J.; Ditlbacher, H.; Lamprecht, B.; Krenn, J. R.; Aussenegg, F. R.; Chan, V. Z. H.; Spatz, J. P.; Moller, M., Spectroscopy of single metallic nanoparticles using total internal reflection microscopy. *Appl. Phys. Lett.* **2000,** *77* (19), 2949-2951.
37. Alekseeva, A. V.; Bogatyrev, V. A.; Khlebtsov, B. N.; Mel'nikov, A. G.; Dykman, L. A.; Khlebtsov, N. G., Gold nanorods: Synthesis and optical properties. *Colloid J.* **2006,** *68* (6), 661-678.
38. Chang, J. A.; Rhee, J. H.; Im, S. H.; Lee, Y. H.; Kim, H.-j.; Seok, S. I.; Nazeeruddin, M. K.; Gratzel, M., High-Performance Nanostructured Inorganic–Organic Heterojunction Solar Cells. *Nano Letters* **2010,** *10* (7), 2609-2612.
39. Grecco, H. E.; Martinez, O. E., Experimental determination of distance and orientation of metallic nanodimers by polarization dependent plasmon coupling. *Pap. Phys. 2*, 020010, 9 pp.
40. Sheikholeslami, S.; Jun, Y.-w.; Jain, P. K.; Alivisatos, A. P., Coupling of optical resonances in a compositionally asymmetric plasmonic nanoparticle dimer. *Nano Lett 10* (7), 2655-60.
41. Guffey, M. J.; Miller, R. L.; Gray, S. K.; Scherer, N. F., Plasmon-Driven Selective Deposition of Au Bipyramidal Nanoparticles. *Nano Lett. 11* (10), 4058-4066.
42. Hu, D.; Yu, J.; Wong, K.; Bagchl, B.; Rossky, P. J.; Barbara, P. F., Collapse of stiff conjugated polymers with chemical defects into ordered, cylindrical conformations. *Nature (London)* **2000,** *405* (6790), 1030-1033.
43. Adachi, T.; Brazard, J.; Chokshi, P.; Bolinger, J. C.; Ganesan, V.; Barbara, P. F., Highly Ordered Single Conjugated Polymer Chain Rod Morphologies. *J. Phys. Chem. C* **2010,** *114* (48), 20896-20902.

44. Bolinger, J. C.; Traub, M. C.; Adachi, T.; Barbara, P. F., Ultralong-Range Polaron-Induced Quenching of Excitons in Isolated Conjugated Polymers. *Science (Washington, DC, U. S.)* **2011,** *331* (6017), 565-567.

Chapter 2: Methods

2.1 Sample preparation

2.1.1 Gold nanorod synthesis

Gold(III) chloride hydrate (254169), silver nitrate (S4641), hexadecyltrimethylammonium bromide (CTAB, H9151), and L-ascorbic acid (A5960) were purchased from Sigma-Aldrich. Hydrochloric acid (A144SI-212) was purchased from Fisher Scientific.

Gold nanorods were prepared by a silver-mediated seed growth process,[45] as previously described by Chen *et al*.[10] and Mayer *et al*.[46] 250 μL of 10 mM $HAuCl_4$ was combined with 9.75 mL of 100 mM CTAB and reduced with 600 μL ice-cold 10 mM $NaBH_4^+$, mixing by rapid inversion for two minutes. The color of the solution changed from vivid yellow-orange to light brown with a pink tinge. This seed solution was kept at room temperature for 2 h before use in the growth step. Growth solution was prepared in an Erlenmeyer flask with a ground glass stopper. 40 mL of 100 mM CTAB and 2 mL of 10 mM $HAuCl_4$ were combined for a vivid yellow-orange color. 600 μL of 10 mM $AgNO_3$ and 800 μL of 1M HCl were added to the Erlenmeyer flask with swirling. After 30 s of swirling in 320 μL of 100 mM ascorbic acid, the growth solution was colorless.

Low aspect ratio nanorods were prepared by adding 1.8 mL of the seed solution to the growth solution. At rest, the color of the solution gradually changed over 12 h from colorless to dark red or purple.

2.1.2 Silver nanoprism synthesis

Silver nitrate (S4641), sodium citrate tribasic dihydrate (204390), and sodium borohydride (452882) were purchased from Sigma-Aldrich. Bis(*p*-sulfonatophenyl)phenylphosphine dihydrate dipotassium salt (BSPP, 15-0463) was

purchased from Strem Chemicals. All solutions were freshly prepared immediately before synthesis.

Silver nanoprisms were prepared by light-mediated seed-based synthesis as previously described by Jin *et al*.[47] In a three-necked flask, 95 mL of deionized water (18.1 MΩ-cm) was stirred vigorously under flowing nitrogen in an ice bath. Two milliliters of 5 mM $AgNO_3$ and 1 mL of 30 mM sodium citrate were added and stirred 30 min. One milliliter of 50 mM ice-cold $NaBH_4^+$ solution was then rapidly injected, causing an immediate color change from colorless to pale yellow. Over the next 15 min, more 50 mM $NaBH_4^+$ was added dropwise at a rate of 3–5 drops every 2 min, increasing the saturation of the solution's yellow color. One milliliter of 5 mM BSPP and 0.5 mL of 50 mM $NaBH_4^+$ were added dropwise over the next five minutes. The solution was stirred overnight in the dark, then 4 mL aliquots were illuminated under a fluorescent lamp for 2 days, during which time a yellow to blue-green color change was observed. The resulting nanoprisms had 72 ± 13 nm edge lengths.

2.1.3 Optical sample preparation for nanoparticle orientation studies

Shadow deposition of aluminum through alphanumeric TEM grids was carried out at a thickness of 90 nm on indium tin oxide (ITO)-coated no. 1 borosilicate glass coverslips (15–30 nm ITO thickness, 70–100 Ω, SPI Supplies) to allow for correlated optical and scanning electron microscopy information.[48] Nanoparticles were sonicated, and, in the case of gold nanorods, heated to 38 °C, before being diluted 5× in deionized water. A 5-10 μL aliquot of this solution was drop-cast on an ITO coverslip and dried under a gentle stream of nitrogen.

2.1.4 MEH-PPV size separation

900 kDa poly[2-methoxy-5-(2-ethylhexyloxy)-1,4-phenylenevinylene] was obtained from (Polymer Source, Inc.) and separated into mass fractions using gel permeation chromatography with 2,6-di-*tert*-butyl-4-methylphenol (BHT)-stabilized tetrahydrofuran (THF, HPLC grade, Pharmco-Aaper). Fractions were dried under a stream of nitrogen gas and stored in a nitrogen-environment glovebox.

2.1.5 Hole-injection device fabrication

Hole-injection devices containing single molecule concentrations of MEH-PPV were prepared as described by Bolinger *et al*.[49] 101 kDa poly(methyl methacrylate) (PMMA), toluene (reagent grade), 4,4'-bis(N-carbazolyl)-1,1'-biphenyl (CBP, 97% pure), and *N,N'*-bis(3-methylphenyl)-*N,N'*-diphenylbenzidine (TPD, 99% pure), and gold (99.999% pure) were obtained from Sigma-Aldrich and used without further purification. Silver paint (Flash-Dry) was obtained from (SPI), and epoxy was obtained from GC Electronics (Part No. 10-347); these were used without further purification. Patterned indium tin oxide-coated glass coverslips were obtained from Evaporated Coatings, Inc. (sheet resistance of 110 Ω) and cleaned by sonicating in acetone, trichloroethylene, isopropanol, and water for 20 min each. These coverslips were dried under nitrogen and part of the ITO electrode area was protected by physical blocking with microscope slides during inductively coupled plasma chemical vapor deposition of 70 nm of SiO_2 at 200 °C using an Oxford Instruments Plasmalab 80plus.

A 6% (w/w) solution of PMMA in toluene was prepared in the glovebox with gentle heating overnight. This solution was diluted 1:8 in toluene just before spin-coating, and a 10 μL aliquot of 1,059 kDa MEH-PPV in toluene at single molecule concentration (areal density of approximately 0.1 molecules/μm^2) was added to a 1 mL volume of the diluted PMMA solution. One drop of the resulting solution was dropped onto a spinning

SiO_2/ITO/glass coverslip, producing a film thickness of 25 nm. After spin-coating, the coverslips were placed in a mask and 25 nm layers of CBP and TPD were thermally deposited, followed by a 100 nm layer of gold. The films were left under vacuum in the thermal deposition chamber for one hour before being transferred to the nitrogen environment of the glovebox for wiring. ITO electrode areas not covered by SiO_2 were scratched with tweezer points to remove the spin-coated polymer film, and wires were affixed to each ITO electrode and to the gold electrode using silver paint. A white glass coverslip was sealed to the device substrate using freshly mixed epoxy, and this seal was allowed to cure overnight for at least 12 h. After sealing, the devices were removed individually from the glovebox for optical experiments.

2.1.6 Hybrid polymer solar cell prototype device synthesis and fabrication

For this collaborative project, material synthesis and device fabrication were carried out by B. Reeja Jayan and Robert J. Ono as described in Jayan *et al*.[50] As I was not present for these steps of the project, I prefer to refer to this publication for complete experimental details in this section, rather than block quoting their writing. I have summarized key information on their synthesis and fabrication work here.

2.1.6.1 Synthesis of organic materials for hybrid solar cell prototype device

Robert J. Ono synthesized regioregular P3HT (M_n = 12.6 kDa; M_w/M_n = 1.3). His method was based on the protocol published by Loewe *et al*.[51] Molecular weight, M_n, and polydispersity index (PDI, or M_w/M_n) were established by gel permeation chromatography (GPC) analysis.

Ono also synthesized two oligomeric thiophene materials, 3,3"-dihexyl-2,2':5',2"-5",2"-quaterthiophene (referred to as oligothiophene, for simplicity), and 3,3"-dihexyl-2,2':5',2"-5",2"-quaterthiophene-5-carboxylic acid (referred to as carboxylated

oligothiophene), according to the protocol published by Tanaka *et al*.[52] Carboxylated oligothiophene was separated from oligothiophene using ion exchange chromatography, and the products' ^{1}H nuclear magnetic resonance (NMR) and mass spectra were compared favorably to literature values.

2.1.6.2 Synthesis of inorganic materials for hybrid solar cell prototype device

B. Reeja Jayan synthesized titanium(IV) oxide, TiO_2, by a sol-gel method using tetrabutyl titanate (TBT) [$Ti(OC_4H_9)_4$] and 2,4-pentanedione, as previously published in Jayan *et al*.[53]

2.1.6.3 Hybrid solar cell prototype device fabrication

B. Reeja Jayan fabricated the hybrid solar-cell prototype devices as described in Jayan *et al*.[50] Briefly, indium-doped tin oxide (ITO)-coated glass substrates (sheet resistance = 10 $\Omega \cdot cm^{-1}$, Nanocs) were cut, etched, and spin-coated with TiO_2 sol-gel, then sintered. Jayan measured the film thickness of the anatase TiO_2 film as approximately 100 nm using a scanning electron microscope (SEM).

Jayan spin-coated the oligomeric interface modifiers (unmodified or carboxylated), if used, out of chloroform, then annealed the modifier layer (approximately 50-65 nm thick, by atomic force microscopy (AFM) measurements). After cooling the oligomer-coated device substrate overnight, filtered P3HT was spin-coated out of chloroform (approximately 50 nm thick, by profilometer and AFM measurements). The coated device substrates were further annealed, then gold electrodes (approximately 150 nm thick) were thermally evaporated atop the P3HT layer through a metal shadow mask (3 mm × 3 mm active area per device, 4 devices per subtrate). The devices were annealed and stored in the dark under ambient conditions.

2.2 MICROSCOPY STUDIES

2.2.1 Optical Studies of Nanoparticle Orientation

2.2.1.1 Through-the-objective total internal reflection LSPR and polarization studies

Plasmon-induced Rayleigh scattering was excited in the nanoparticles via through-the-objective total internal reflection (TIR) microscopy using a 60× TIRF objective (Olympus, oil, 1.45 N.A.). A liquid crystal tunable filter (LCTF, CRi VariSpec) was used to select a specific wavelength from a halogen white light source (Ocean Optics DH-2000), producing linearly polarized output light centered at a fixed wavelength with a bandwidth of 7 nm. The polarization of the output light was rotated using a broadband polarization rotator (BPR, Newport, PR-550). These two devices allowed localized surface plasmon resonance (LSPR) spectra to be measured at a fixed polarization angle (by tuning the LCTF and holding the BPR at a fixed position) or measuring the polarization response of the scattering at a particular wavelength (by fixing the LCTF and tuning the BPR). A system schematic shows the relative position of these optics in Fig. 2.1.

The excitation light was focused off-axis at the back focal plane of the objective using a plano-convex lens on a translation mount, which allowed the excitation angle of the light at the sample to be tuned through a range of angles above the critical angle for TIR. The reflected TIR excitation was physically blocked to create a dark field, and the scattered light from the nanoparticles was detected using an electron-multiplying charge-coupled device (EM-CCD, Princeton Instruments PhotonMax 512B). The integration time of the EM-CCD for LSPR spectral acquisition was 1 s × 5 acquisitions, which produced a single image in the image stack, corresponding to a specific excitation

wavelength and polarization angle. In polarization spectra, the integration time was increased to 3 s × 5 acquisitions.

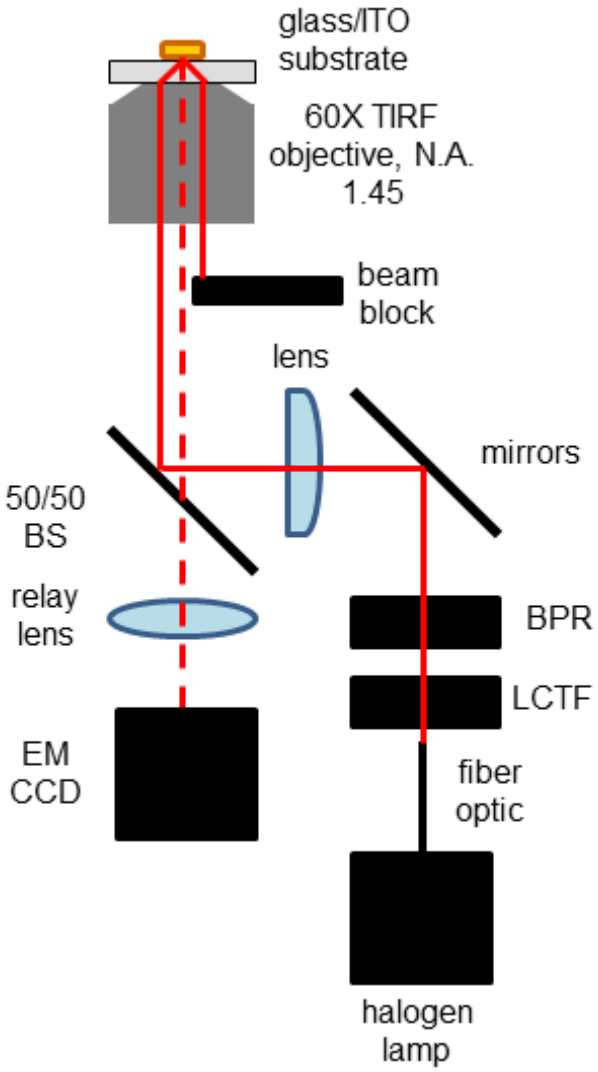

Figure 2.1

Figure 2.1: Experimental schematic for plasmon-induced Rayleigh scattering excited using through-the-objective TIR dark field microscopy. The excitation wavelength was selected by a liquid crystal tunable filter (LCTF) and polarization was set using a broadband polarization rotator (BPR). The excitation angle was controlled by a plano-convex lens on a translation mount. The reflected TIR excitation beam was blocked with a physical blocker to create a dark field, and the scattered light from nanoparticles was collected and detected using an electron-multiplying charge-coupled device (EM-CCD).

LSPR spectral data were obtained by scanning the LCTF from 450–720 nm in 1 nm steps and taking a CCD image at each wavelength step. Spectra were calculated by integrating the scattering intensity from each region of interest over the entire image stack to build up a complete spectrum. Spectra were taken under both s- and p-polarized excitation and summed to produce a final LSPR spectrum; this strategy produced excellent agreement between the LSPR spectrum measured using our TIR-LCTF approach and traditional dark field scattering. These spectra were normalized by the lamp profile. Polarization response data were obtained by rotating the BPR from 0˚ to 360˚ in 10˚ steps, and taking a CCD image at each polarization angle. As before, the scattering intensity from a region of interest was calculated for each image and then integrated over all images within the image stack. Polarization spectra were normalized by their maximum intensities at a given excitation wavelength. Samples were imaged under nitrogen to prevent oxidation.

2.2.1.2 Traditional dark field scattering and polarization studies

Traditional dark field scattering experiments were conducted using a dark field condenser (Olympus, 0.92–0.8 N.A.) and a 100× variable N.A. oil-immersion objective (Olympus). Scattered light collected through the objective was sent to a spectrometer (PI Acton, SpectraPro 2500i) with a liquid-nitrogen-cooled CCD detector (PI Acton, Spec10). LSPR spectra were collected using unpolarized light with integration times of 1 s × 5 acquisitions, as in the TIR-LCTF experiments. Polarization response data were obtained by rotating linear polarizing film (Edmund Optics) over the dark field condenser and collecting LSPR spectra at each polarization angle from 0º to 360º in 20º steps. These spectra were normalized by the lamp profile. Samples were imaged under nitrogen to prevent oxidation.

2.2.2 Optical studies of MEH-PPV in hole-injection devices

Optical experiments used an oil-immersion objective (Zeiss, 100×, N.A. 1.25), a 2.5× tube lens (Zeiss), and a fan-cooled electron-multiplying charge-coupled device (Andor, EM-CCD, 512 × 512 pixels). At this magnification, the edge of 1 pixel corresponded to 64 nm. The device was mounted on the microscope stage and the copper wires affixed to the gold anode and to the ITO electrode of the device being interrogated were connected to function generators, shown schematically in Figure 2.2. The 488-nm line of an Ar Kr ion laser (Melles Griot, model 35 LTL 835) was attenuated to a power of 600 μW, and used to excite the fluorescence of isolated MEH-PPV chains embedded in the device in a wide field inverted geometry.

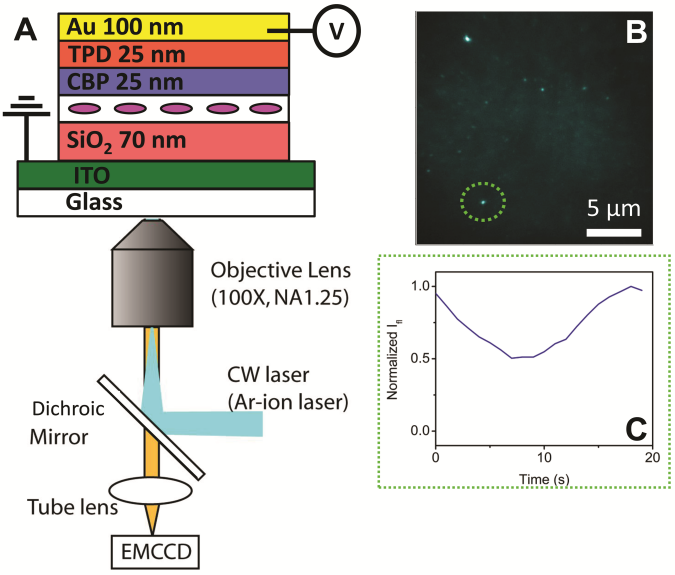

Figure 2.2

Figure 2.2: Single-molecule concentrations of MEH-PPV in a supporting PMMA film are encapsulated in a hole-injection device (A) that is optically transparent from the bottom side, allowing for observation of modulation of the fluorescence intensity of many single polymer chains simultaneously in a wide-field image The MEH-PPV chains are randomly oriented within the PMMA film. (B). This modulation is achieved through active control of the bias applied to the gold anode, injecting a varying number of holes into an MEH-PPV chain as the bias sweeps more positive, or by active control of the excitation polarization (C). The former experiment reports on energy transport in the polymer, while the latter reports on the structure each chain has adopted. Correlating these experiments gives insight into the relationship between polymer morphology and energy transport.

The function generators triggered image collection in the EM-CCD to synch with two different independent variable changes. For polarization anisotropy studies, the function generators triggered an electro-optic modulator's (EOM) rotation of the linear polarization of the excitation, so that each image frame collected by the EM-CCD corresponded to a known excitation polarization angle, while no bias was applied except during control experiments. For bias-modulated intensity-centroid (BIC) spectroscopy, the function generator triggered the bias applied to the device via the gold anode and grounded via the ITO electrode, so that each image frame collected by the EM-CCD corresponded to a known applied bias, while the excitation polarization was rotated so quickly as to be considered circular. In either case, a 1 s integration time was used, and the frequency of the waveforms generated by the function generators was chosen to match that time. In excitation polarization experiments, the bias applied to the EOM had a frequency of 50 mHz. In BIC, two applied bias regimes were explored because the bias at which fluorescence quenches varies among the single molecules. For a ramp from -5 to 5 V with a frame increment of 0.2 V and 51 frames per bias sweep cycle, a frequency of 20 mHz was used. For a ramp from -2 to 7 V with a frame increment of 0.2 V and 46 frames per bias sweep cycle, a frequency of 22 mHz was used. Eleven bias sweep cycles were collected, the first of which was used for background. Data from time points in each of the cycles where the excitation polarization or the applied bias were the same were synchronously averaged. Nineteen cycles were synchronously averaged for excitation polarization experiments, and ten cycles were synchronously averaged for BIC experiments.

2.2.3 Electro-optical studies of hybrid polymer solar cell prototype devices

In-device fluorescence spectroscopy (ID-FVS) measurements were performed on a home-built apparatus based on an inverted microscope (Zeiss, Axiovert 200) with a 5× objective lens (NA 0.12). The excitation source was the 488-nm line of an Ar-Kr ion laser (Melles Griot, model 35 LAL-030-208). The excitation beam was focused onto the device and the emission was detected by an avalanche photodiode (APD) (Perkin-Elmer Optoelectronics SPCM-AQR-15). A master function generator was used to synchronize both a function generator (Wavetek, model 29) and a multichannel scalar board (MCS, Becker Hickle PMS-400). The device and electro-optical apparatus are shown schematically in Figure 2.3.

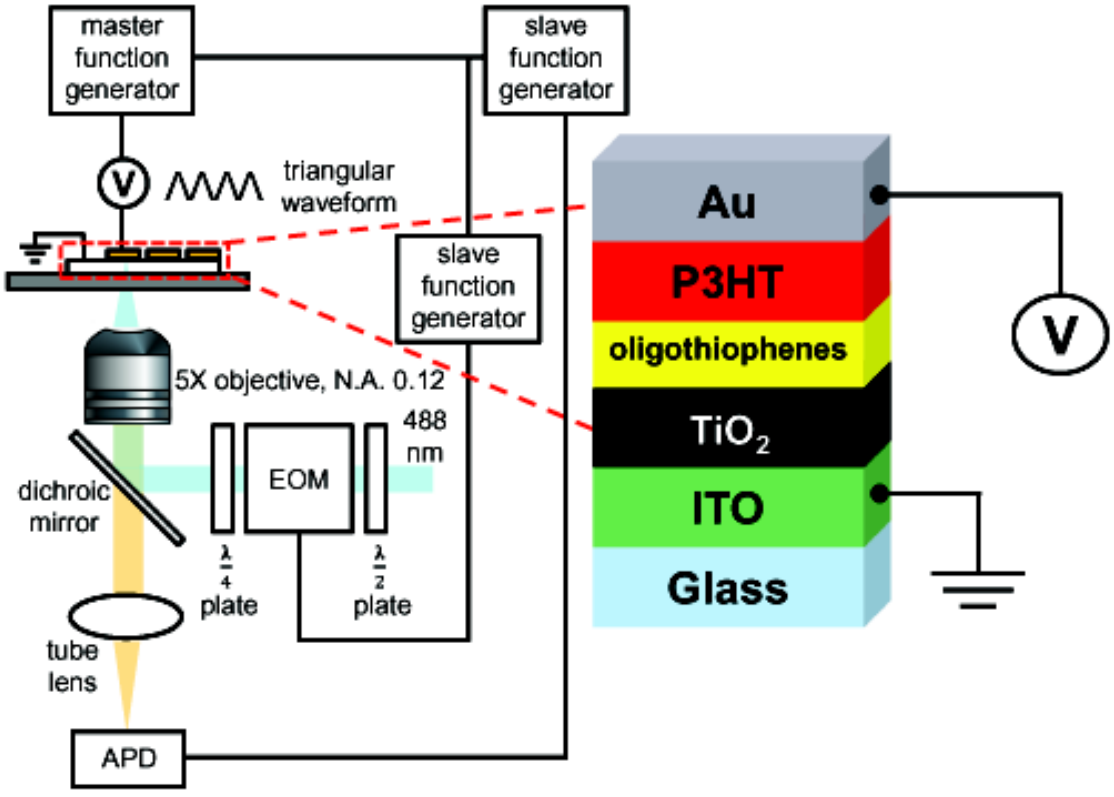

Figure 2.3

Figure 2.3: Schematic overview of the In-Device Fluorescence Voltage Spectroscopy (ID-FVS) for facile screening of bilayer devices. Half- and quarter-wave plates are used in combination with an electro-optic modulator and a function generator to create pseudo-circularly polarized light from 488 nm laser excitation. The filters used in the detection line were a dichroic mirror and a 488 nm notch filter from Chroma. The excitation line also had a 488 nm laser line filter. The beam is focused at the P3HT/oligothiophene/TiO_2 interface, and the fluorescence emission from the P3HT is collected on an avalanche photodiode for non-imaging experiments. Function generators ensure that APD collection is synced with the applied bias wave in a reproducible way.

For typical experiments, the applied bias to the device was programmed to be a triangular waveform of 0 – 1 – 0 - (-1) - 0 V as each cycle was set to be of 1 s duration (4 $V \bullet s^{-1}$). Acquisition time per point was 10 ms and 4000 points were recorded for each measurement. In these experiments, the excitation intensity was minimized (~800 $mW \bullet cm^{-2}$) to mimic the power range of a solar simulator and the voltage bias rate was adjusted to match the solar cell testing conditions used by Jayan. Fluorescence modulation results were acquired for 40 cycles and they were synchronously averaged to increase the signal-to-noise ratio. When the applied bias varied, the peak voltage changed to ± 0.5, 2, or 4 V. To determine whether changes arose from the scan rate or the expanded bias window, the scan rate was maintained at 4 V/s for one set, giving cycle times of 0.5, 2, and 4 s, respectively, and varied with another set, giving scan rates of 2, 8, and 16 $V \bullet s^{-1}$, respectively, for 1 s cycle times. The acquisition time per point was kept at 10 ms and 4000 points were still recorded for each measurement, so the number of cycles synchronously averaged varied with the applied bias. At 0.5 V, 80 cycles were averaged; at 1 V, 40 cycles; at 2 V, 20 cycles; and at 4 V, 10 cycles were averaged.

2.2.2 Scanning electron microscopy (SEM) studies

After optical studies of noble metal nanoparticles were completed, immersion oil was cleaned from the coverslip with folded lens paper moistened with acetone. The coverslip was stored in a Fluoroware container in a vacuum dessicator overnight. The gridded section of the coverslip was mounted on a standard SEM holder using colloidal graphite and dried on a hot plate. Imaging was carried out on a Hitachi S-5500 at 30.0 kV.

2.3 IMAGE PROCESSING

2.3.1 Polarization anisotropy

Polarization anisotropy studies revealed the degree to which interrogated molecules are polarized in the plane of the stage of the microscope. Using an in-house written MATLAB script, the pattern of fluorescence intensity modulation was fit to a *cos(2θ)* function, shown in Equation 2.1.

$$I = \frac{I_{\max} + I_{\min}}{2} - \frac{I_{\max} - I_{\min}}{2}(\cos(2(\theta - \varphi))) \quad (2.1)$$

The ratio of the difference between the intensity maxima and minima to their sum is referred to as the modulation depth, *M*. Barring the effect of the high N.A. excitation, an ideal transition dipole would not be excited by light polarized orthogonally to that dipole, so the intensity minimum would be zero and the modulation depth would be 1. A system with an isotropic distribution of transition dipoles would be equally excited by all polarizations of light, so the intensity maximum and minimum would be equal and *M* would be zero. The modulation depth of a single polymer chain informs on its structure. A rod-like conformation, as long as it is not oriented orthogonally to the plane of the stage, will have a projection in the plane of the stage that exhibits behavior similar to an ideal dipole, with typical *M* values of 0.7 to 0.9. An example of one single MEH-PPV chain's response to excitation polarization is shown in Figure 2.2C. A globular conformation does not align its individual chromophores as strongly, so its modulation depth is smaller. This technique cannot report on the vector portion of the net transition dipole of the polymer that is oriented orthogonally to the plane of the microscope stage. Polarization anisotropy experiments also revealed the angle, ϕ, at which the projection of the net transition dipole of the polymer was oriented in the plane of the stage. For a rod-like conformation, this angle represented the longitudinal axis of the rod.

2.3.2 Bias-induced intensity centroid (BIC) spectroscopy 2-D Gaussian point-spread function fitting

Molecules were identified and a 20 pixel × 20 pixel area centered around the molecule but excluding the molecule itself was fit to a plane and that plane was background subtracted from that area. Background-subtracted fluorescence images were then fit to a 2-D Gaussian, Equation 2.2, using least squares algorithms in MATLAB scripts written in-house.

$$I(x,y) = z_0 + I_0 e^{\left[\frac{-1}{2}\left[\left(\frac{x-x_0}{s_x}\right)^2+\left(\frac{y-y_0}{s_y}\right)^2\right]^2\right]} \quad (2.2)$$

In Equation 2.2, each position (x,y) has an intensity, I, that can be modeled as the sum of the background, z_0, and the product of the peak intensity, I_0, with a Gaussian centered at x_0,y_0 that has a spread in the x-direction of s_x and a spread in the y-direction of s_y.

As the fluorescence was reversibly quenched by the applied bias, the peak of this Gaussian, called the fluorescence centroid, moved. The direction and distance of this fluorescence centroid shift were recorded. The shift direction was compared to the phase angle determined by polarization anisotropy experiments. Synchronously averaged fluorescence centroid positions were plotted and a fit to a least squares regression line passing through the intensity-weighted center-of-mass of the plot. The anisotropy of this distribution was described by comparing the variance of the positions along the least squares regression line to the variance along its perpendicular bisector.

2.3.3 Bias-induced intensity centroid (BIC) spectroscopy bivariate normal distribution point-spread function fitting

The point-spread function of the fluorescence image of each molecule was fit to a bivariate normal distribution function, Equation 2.3, using IGOR Pro software.

$$I = \frac{1}{2\pi\sigma_x\sigma_y\sqrt{1-\rho^2}} \exp\left(\frac{-1}{2(1-\rho^2)}\left[\frac{(x-\mu_x)^2}{\sigma_x^2} + \frac{(y-\mu_y)^2}{\sigma_y^2} - \frac{2\rho(x-\mu_x)(y-\mu_y)}{\sigma_x\sigma_y}\right]\right) \quad (2.3)$$

The peak location in the *x,y* plane is given by μ_x,μ_y. The variances in the x- and y-directions, σ_x^2 and σ_y^2, are equal if the spot is circular and different if the spot is elliptical. The cross correlation coefficient, ϱ, is bounded by -1 and 1. It describes the orientation and relative asymmetry of the ellipsoidal spot. This description of the fluorescence image is given in the *x,y* lab frame. To determine its variance along the major and minor axes of the ellipse, and the angle of the major axis of the ellipse, a 2×2 rotation matrix was solved analytically as described by Clark *et al*.[54]

As the fluorescence was reversibly quenched by the applied bias, the peak, called the fluorescence centroid, of this bivariate normal distribution moved. The distance of this fluorescence centroid shift was recorded. For varying points in the quenching cycle, the ratio of the major axis variance of the elliptical fluorescence image to its minor axis variance was recorded, reflecting the degree of ellipticity of the spot. The angle at which the major axis of the elliptical fluorescence image was oriented in the plane of the microscope stage was also recorded. The major axis angle was compared to the phase angle determined by polarization anisotropy experiments; the difference was called the ellipse delta. If the elongations results form the physical extent of the long axis of the polymer this ellipse delta should be zero.

2.4 REFERENCES

1. Nikoobakht, B.; El-Sayed, M. A., Preparation and growth mechanism of gold nanorods (NRs) using seed-mediated growth method. *Chem. Mater.* **2003,** *15* (10), 1957-1962.

2. Chen, H. J.; Shao, L.; Woo, K. C.; Ming, T.; Lin, H. Q.; Wang, J. F., Shape-Dependent Refractive Index Sensitivities of Gold Nanocrystals with the Same Plasmon Resonance Wavelength. *Journal of Physical Chemistry C* **2009,** *113* (41), 17691-17697.
3. Mayer, K. M.; Lee, S.; Liao, H.; Rostro, B. C.; Fuentes, A.; Scully, P. T.; Nehl, C. L.; Hafner, J. H., A label-free immunoassay based upon localized surface plasmon resonance of gold nanorods. *ACS Nano* **2008,** *2* (4), 687-692.
4. Jin, R.; Cao, Y.; Mirkin, C. A.; Kelly, K. L.; Schatz, G. C.; Zheng, J. G., Photoinduced Conversion of Silver Nanospheres to Nanoprisms. *Science* **2001,** *294* (5548), 1901-1903.
5. Weber, M. L.; Willets, K. A., *J. Phys. Chem. Lett.* **2011,** *2*, 1766.
6. Bolinger, J. C.; Fradkin, L.; Lee, K.-J.; Palacios, R. E.; Barbara, P. F., Light-assisted deep-trapping of holes in conjugated polymers. *Proc. Natl. Acad. Sci. U. S. A., Early Ed.* **2009,** (Jan. 26 2009), 1-5, 5 pp.
7. Reeja-Jayan, B.; Koen, K. A.; Ono, R. J.; Vanden Bout, D. A.; Bielawski, C. W.; Manthiram, A., Oligomeric interface modifiers in hybrid polymer solar cell prototypes investigated by fluorescence voltage spectroscopy. *Physical Chemistry Chemical Physics* **2015,** *17* (16), 10640-10647.
8. Loewe, R. S.; Ewbank, P. C.; Liu, J.; Zhai, L.; McCullough, R. D., Regioregular, Head-to-Tail Coupled Poly(3-alkylthiophenes) Made Easy by the GRIM Method:□ Investigation of the Reaction and the Origin of Regioselectivity. *Macromolecules* **2001,** *34* (13), 4324-4333.
9. Tanaka, K.; Takimiya, K.; Otsubo, T.; Kawabuchi, K.; Kajihara, S.; Harima, Y., Development and Photovoltaic Performance of Oligothiophene-sensitized TiO₂ Solar Cells. *Chemistry Letters* **2006,** *35* (6), 592-593.
10. Reeja-Jayan, B.; Manthiram, A., Understanding the Improved Stability of Hybrid Polymer Solar Cells Fabricated with Copper Electrodes. *ACS Applied Materials & Interfaces* **2011,** *3* (5), 1492-1501.
11. Clark, K. A.; Krueger, E. L.; Vanden Bout, D. A., Direct Measurement of Energy Migration in Supramolecular Carbocyanine Dye Nanotubes. *The Journal of Physical Chemistry Letters* **2014,** *5* (13), 2274-2282.

Chapter 3: Spectrally-Resolved Polarization Anisotropy of Single Plasmonic Nanoparticles Excited by Total Internal Reflection[1]

3.1 INTRODUCTION

Noble metal nanoparticles have attracted significant attention due to their ability to support localized surface plasmons, which not only produce a unique colorimetric signature known as the localized surface plasmon resonance (LSPR), but also enhance electromagnetic fields at the nanoparticle surface by many orders of magnitude.[5-9] Because of the diversity in the shape and size of nanoparticles, single-particle spectroscopy has emerged as an important technique for characterizing individual particles and determining how the LSPR changes as a function of nanoparticle structure.[10-15] Understanding how the shape and size of individual nanoparticles affects the LSPR is important for both LSPR sensing experiments as well as for spectroscopic techniques that take advantage of the local electromagnetic field enhancements around nanoparticles, such as surface-enhanced Raman scattering (SERS).[15-21] Polarization is an important variable for understanding how the shape of the nanoparticle dictates the measured LSPR and SERS response.[10-12, 14, 20, 30-36] For example, rod-shaped nanoparticles support two plasmon modes: the transverse mode, which is excited along the short axis of the rod, and the longitudinal mode, which is excited along the long axis of the rod.[37, 38] Exciting the rod with light polarized along the long axis will generate higher overall signals in the measured scattering spectrum, which improves the signal-to-noise in a sensing assay. Similar results can be obtained for other highly anisotropic structures such as spherical dimers, bipyramids, or asymmetrically truncated triangles.[17, 39-41] Thus,

---

[1]Reprinted with permission from Koen, K. A.; Weber, M. L.; Mayer, K. M.; Fernandez, E.; Willets, K. A., Spectrally-Resolved Polarization Anisotropy of Single Plasmonic Nanoparticles Excited by Total Internal Reflection. *The Journal of Physical Chemistry C* **2012,** *116* (30), 16198-16206. Copyright 2012 American Chemical Society. Available at http://pubs.acs.org/doi/abs/10.1021/jp301878e.

polarization-resolved single-nanoparticle LSPR studies are important for revealing local heterogeneity and orientation within diverse nanoparticle populations.

Traditionally, LSPR spectra of single nanoparticles have been measured using dark field scattering, in which the nanoparticles are excited with high angle excitation light and the resulting scattering is collected using a low numerical aperture optic.[55-58] By incorporating polarization-selective optics in the excitation or detection channel, one can determine under what polarization conditions the scattering intensity is maximized and minimized. This geometry is highly useful for studying anisotropic structures such as gold nanorods, bipyramids, and nanoparticle dimers because the relationship between the nanoparticle orientation and its anisotropic scattering is easily understood.[59-61] However, for structures like ideal nanoprisms, the scattering from the nanostructure is predicted to be polarization insensitive, due to the inherent symmetry of the triangular structure. Thus, to determine the orientation of a triangular nanoparticle, traditional structural characterization techniques, such as atomic force microscopy or electron microscopy, are typically employed. These techniques characterize one subset of an ensemble, and another subset is then used in other experiments. An optical technique to determine orientation would allow subsequent use of the same nanoparticles.

The relevant orientation for these polarization-selective dark field scattering techniques is in the plane of the sample (defined here as the *x*–*y* plane, Figure 3.1). Nanorods, with only 180º of rotational symmetry, are anisotropic, with the limiting case for anisotropy being a nanorod of high aspect ratio. The limiting case for an isotropic structure would be a nanodisk or nanosphere, with infinite axes of rotational symmetry in the sample plane. We describe triangular nanoprisms as pseudoisotropic structures because they have 120º of rotational symmetry. At the excitation energies used in this

study, we do not expect to excite the out-of-plane quadrupolar modes and thus we expect a polarization-insensitive response with traditional dark field optics, as discussed below.[62]

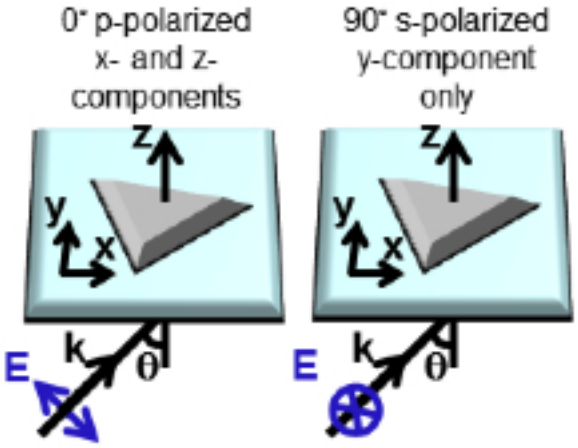

Figure 3.1: Schematic of the coordinate system for polarization-resolved through-the-objective TIR. The blue arrows represent the electric field (**E**) vector of the excitation light, which is introduced at an angle θ relative to the optical (z) axis. At the sample (x–y) plane, p-polarized light is actually elliptical, with a strong z-component and a relatively small x-component.

Total internal reflection (TIR) dark field scattering offers a unique alternative to the standard dark field geometry described above because it provides a highly anisotropic polarization-dependent excitation field. In TIR, high angle excitation light is introduced at the interface between high- and low-refractive index materials. If the angle of incidence is above the critical angle for that interface, the excitation light will be reflected back into the high-index material, with only an evanescent wave penetrating into the lower index medium. If nanoparticles are present at the interface, they will scatter light from the evanescent wave, which can be collected to produce the LSPR spectrum. Initial experiments using TIR excitation for LSPR spectroscopy used a prism to introduce the excitation light at high angle, and then collected light using an objective placed on the other side of the sample.[36, 63, 64] Recently, through-the-objective TIR has been applied to

single particle LSPR spectroscopy, which allows both the excitation and collection to be accomplished through the same optic, as shown in Chapter 2, Figure 2.1.[65-67]

Unlike the dark field scattering geometry, TIR excitation introduces added complexity to the sample excitation through the strong polarization dependence of the evanescent field.[68] As illustrated schematically in Figure 3.1, s-polarized light produces excitation light polarized in the plane of the sample only, aligned with the *y*-axis. On the other hand, p-polarized light has both an in-plane component, aligned with the *x*-axis, and an out-of-plane component, aligned along the *z*-axis; this leads to elliptically-polarized excitation light at the interface. For excitation polarization angles between s- and p-polarization, the sample will be excited by a mixture of in-plane and out-of-plane excitation, which results in a highly anisotropic excitation field. In this chapter, we explore how using an anisotropic polarization-dependent excitation field generated by TIR affects the polarization-dependent LSPR response for both anisotropic and isotropic nanostructures. Briefly, optical studies were carried out on a patterned, optically transparent, electrically active substrate such that nanoparticles studied in optical experiments could be identified during subsequent scanning electron microscopy (SEM) imaging to confirm orientation. A more detailed discussion of the methods may be found in Chapter 2.

3.2 Orientation of Gold Nanoparticles Determined Using Through-the-Objective TIR Excitation of LSPR and Polarization Anistropy

Gold nanorods were used for the initial studies to probe how the anisotropic polarization properties of the TIR excitation affected a well-known anisotropic scatterer.

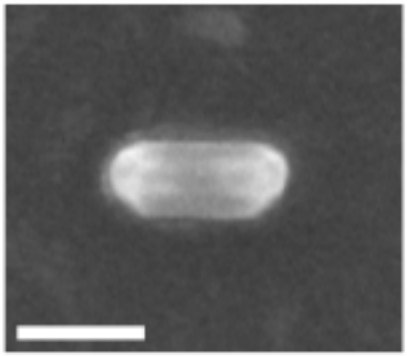

Figure 3.2: A scanning electron micrograph (SEM) image, taken at 30.0 kV, of a gold nanorod. The nanorod is approximately 70 nm long and 35 nm in diameter. Scale bar is equal to 50 nm.

In the example shown in Figure 3.2, the longitudinal axis of the nanorod is oriented horizontally. The longitudinal plasmon mode of a nanorod is excited most efficiently when the excitation polarization of resonant light is aligned with its long axis, and is not excited when the excitation polarization is orthogonal to this axis.[37,69,70] This polarization response is analogous to dipole scattering and is expected to produce an intensity response that follows Equation 3.1,

$$I(\phi) \propto \cos^2(\phi\text{-}q), \tag{3.1}$$

where ϕ is the polarization angle of the excitation and q is the orientation of the nanorod with respect to the laboratory frame. Nanorods also support a transverse plasmon mode; however, this mode does not appear in single particle scattering measurements because it is a primarily absorptive mode due to the small size of the transverse diameter of the nanorod.[33] (The nanorods used in these experiments had lengths of approximately 70 nm and transverse diameters of approximately 30 nm.)

Figure 3.3 shows the wavelength-dependent polarization response for a representative nanorod with the LSPR spectrum shown in Figure 3.3A. For each panel (Figure 3.3B–G), the excitation wavelength was held at a fixed value, and the

polarization was varied from 0˚ (p-polarized) to 360˚ in 10˚ steps. The scattering intensity was measured at each polarization angle, and is plotted along the radial axis of the polar plots shown in Figure 3.3. These polarization-dependent scattering intensity polar plots are henceforth referred to as polar plots, for conciseness. The polar plots are overlaid on the scanning electron micrograph (SEM) image of the nanorod to show the alignment of the polarization response with respect to the orientation of the nanorod. The figure-eight shape in each polar plot is characteristic of the $\cos^2$ polarization response of a dipole, as described above. Changing the excitation wavelength produced no significant change in the polarization angle associated with maximum scattering. This is consistent with our picture of the gold nanorod as containing a single scattering dipole associated with the longitudinal plasmon mode. Importantly, we are able to reproduce the previously reported dipole-like scattering response from a single nanorod, despite the complex polarization characteristics of the TIR excitation.[69,59,70]

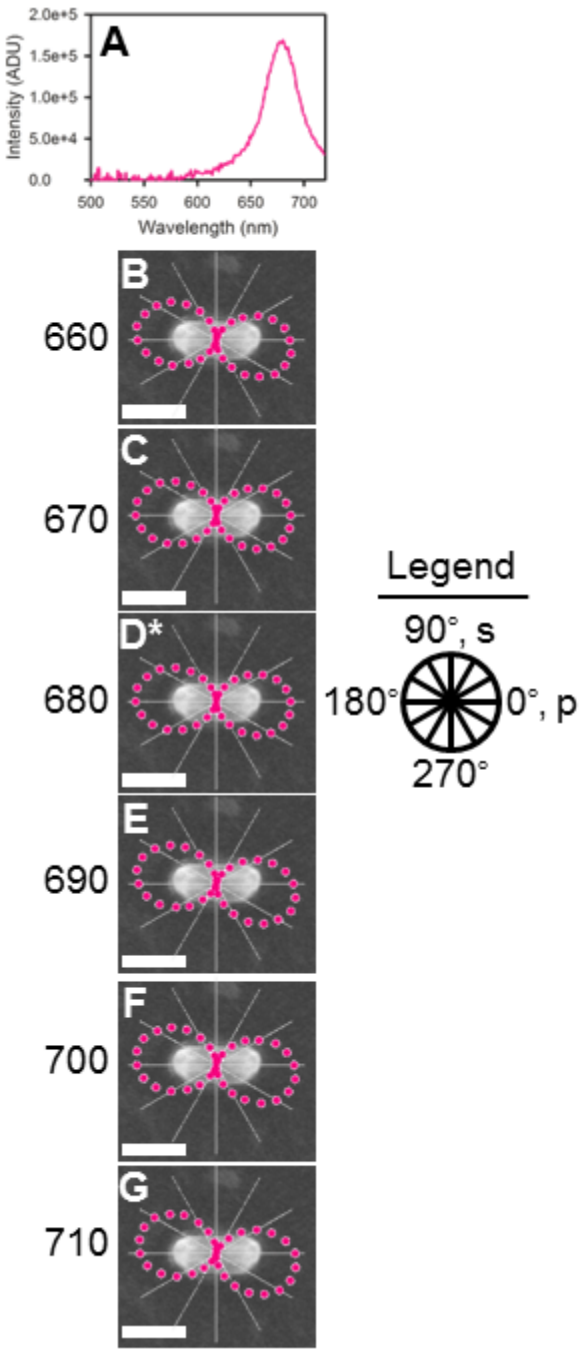
A
Intensity (ADU)
2.0e+5
1.5e+5
1.0e+5
5.0e+4
0.0
500
550
600
650
700
Wavelength (nm)
B
660
C
670
D*
680
E
690
F
700
G
710
Legend
90°, s
180°
0°, p
270°

Figure 3.3

Figure 3.3: (A) LSPR spectrum of a single gold nanorod taken with through-the-objective TIR, summed over both s- and p-polarized excitation. (B–G) Polar plots showing the scattering intensity at a fixed wavelength (radial axis) plotted against the excitation polarization angle (ϕ) in polar coordinates. A legend relating the excitation angles to the lab frame is shown at right. Polar plots are laid over the corresponding SEM image of the scattering nanorod. All plots have the same radial intensity scale, normalized to the maximum scattering intensity, and all scale bars are 50 nm. Scattering wavelengths are (B) 660 nm, (C) 670 nm, (D) 680 nm, (E) 690 nm, (F) 700 nm, and (G) 710 nm. Plot (D) is labeled with an asterisk because it is closest to the plasmon resonance of the nanoparticle.

Next, we determined whether the polarization response of the nanorod LSPR changed as the angle of incidence (θ, Figure 3.1) of the excitation light was tuned. Both the intensity of each polarization component (e.g. x, y, and z) and the overall excitation intensity at the sample surface are well-known to be sensitive to the angle of incidence of the TIR excitation, as shown in Figure 3.3.[71] Total internal reflection occurs at the interface between a higher refractive index medium and a lower refractive index medium when the excitation angle of incidence is greater than or equal to the critical angle (Equation 3.2).

$$\theta_c = \sin^{-1}\frac{n_2}{n_1} \tag{3.2}$$

An evanescent field, rather than a transmitted beam, penetrates the lower refractive index medium. The intensity of the evanescent field at the interface ($z = 0$) is defined for each polarization component according to Equations 3.3–3.5.

$$I_x = \frac{4\cos^2\theta\left(\sin^2\theta-\left(\frac{n_2}{n_1}\right)^2\right)}{\left(1-\left(\frac{n_2}{n_1}\right)^2\right)\left[\left(1+\left(\frac{n_2}{n_1}\right)^2\right)\sin^2\theta-\left(\frac{n_2}{n_1}\right)^2\right]} \tag{3.3}$$

$$I_y = \frac{4\cos^2\theta}{1-\left(\frac{n_2}{n_1}\right)^2} \tag{3.4}$$

$$I_z = \frac{4\cos^2\theta\sin^2\theta}{\left(1-\left(\frac{n_2}{n_1}\right)^2\right)\left[\left(1+\left(\frac{n_2}{n_1}\right)^2\right)\sin^2\theta-\left(\frac{n_2}{n_1}\right)^2\right]} \tag{3.5}$$

The intensity of each polarization component changes as a function of the angle of incidence, as shown for four excitation angle, θ, values in Figure 3.4 for the interface between glass ($n_1 = 1.515$) and air ($n_2 = 1.0003$).

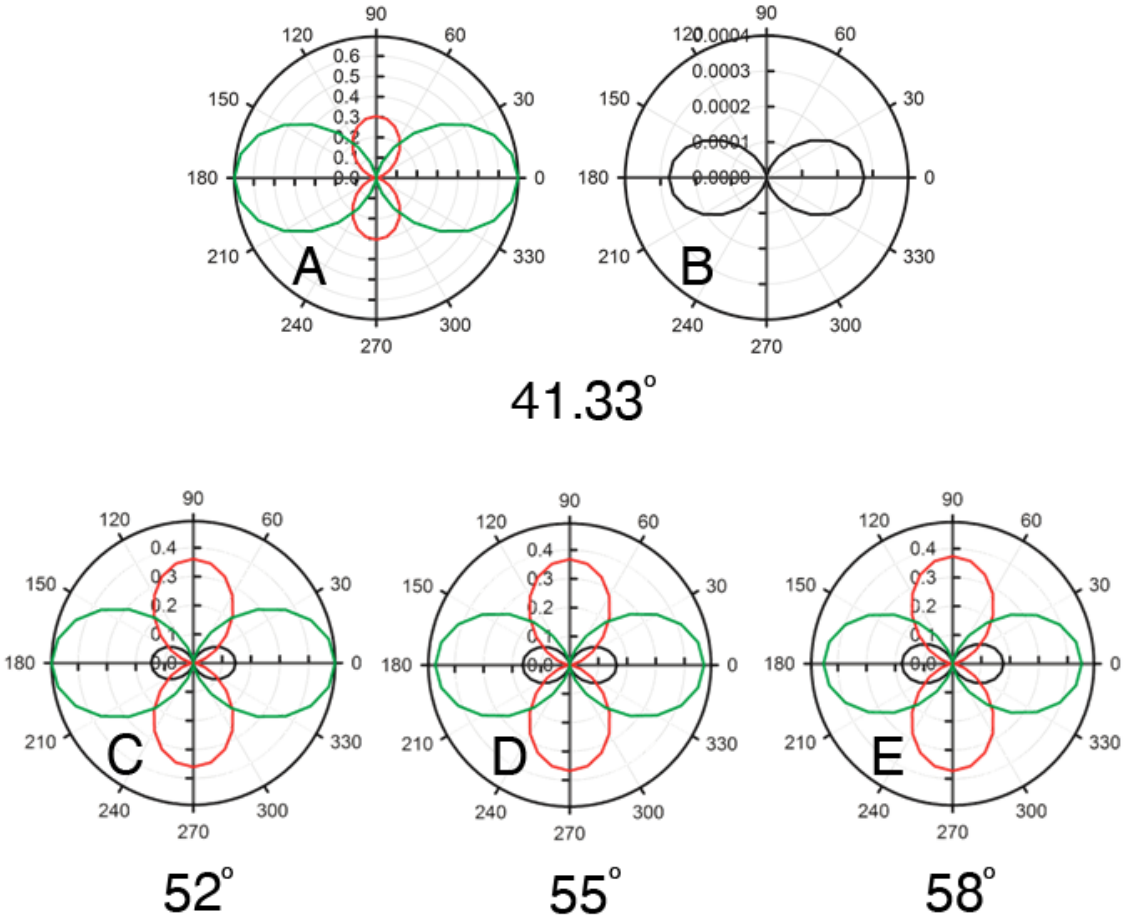

Figure 3.4: Intensity of the *x*- (black), *y*- (red), and *z*- (green) components of the evanescent field as a function of the in-plane excitation polarization angle, ϕ (polar coordinate, plotted 0–360°). Four different values of the angle of incidence are shown. All plots are normalized by total calculated intensity.

For an angle of incidence just above the critical angle, 41.33°, the intensity of the *x*-component is too low to be visible in Figure 3.4A, so a zoomed-in plot is shown as well (Figure 3.4B). As the angle of incidence increases, the relative contribution of the *x*-component (Figure 3.4B–E, black curve) increases and the *z*-component (Figure 3.4A, C–E, green curve) decreases. The relative contribution of the *y*-component (Figure 3.4A, C–

E, red curve) increases as the angle of incidence of the excitation beam increases. The total intensity of the evanescent field also decreases as the angle of incidence of the excitation beam increases. The complicated nature of the excitation warranted the control experiment whose results are shown in Figure 3.5.

For the nanorod with LSPR shown in Figure 3.5A, polarized scattering data were taken at 650 nm as the angle of incidence was increased from 52° to 58°, as shown in Figure 3.5B–D (details on measuring the angle of incidence were described previously by Kaplan-Ashiri *et al.*[72]). These angles of incidence correspond to a range of evanescent field penetration depths from 96 nm to 52 nm, respectively, which extend beyond the expected height of the nanoparticle (approximately 30 nm for nanorods, up to 17 nm for nanoprisms).[73] Both the orientation of the scattering response in the polar plots as well as the $\cos^2$ response remained constant as the excitation incidence angle increased (Figure 3.5B–D), indicating that the nanorod retained its dipole-like scattering character, even as the relative intensities of the polarization components of the excitation field changed. In this example, we did not normalize the scattering intensity in the polar plots, so we could track how the scattering intensity changed as the angle of incidence was increased. The overall intensity, I, of the scattering decreased as θ increased, as expected for an evanescent wave.[74] We also calculated the modulation depth, defined in Equation 3.6 as

$$M = (I_{max} - I_{min})/(I_{max} + I_{min}) \tag{3.6}$$

where $M = 1$ indicates a dipole-like scatterer and $M = 0$ represents an isotropic scatterer.[75,76,43] In all three cases, $M \approx 0.9$, indicating a highly anisotropic scattering signal, as expected, but also showing that the modulation depth was consistent as θ changed. As above, we note that the complex polarization characteristics of the TIR excitation do not influence the observed polarization response of the nanorod LSPR.

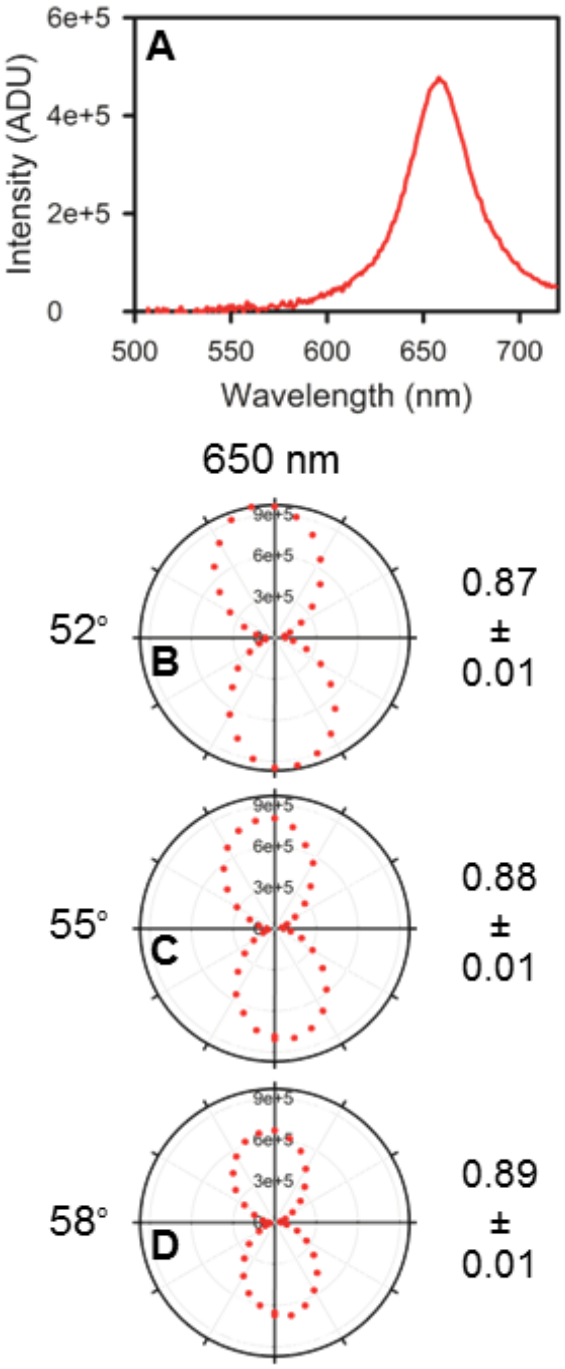
A
6e+5
4e+5
2e+5
0
Intensity (ADU)
500
550
600
650
700
Wavelength (nm)
650 nm
52°
B
0.87
±
0.01
55°
C
0.88
±
0.01
58°
D
0.89
±
0.01

Figure 3.5

Figure 3.5. (A) LSPR spectrum of a gold nanorod, summed over s- and p-polarized excitation and at 52º angle of incidence. (B–D) Polar plots showing the Rayleigh scattering intensity at 650 nm as a function of excitation polarization angle (ϕ) for varying angle of incidence, θ: (B) 52˚, (C) 55˚, and (D) 58˚. The calculated modulation depth, M, for each excitation angle is listed next to each polar plot.

3.3 Orientation of Silver Nanoprisms Determined Using Through-the-Objective TIR Excitation of LSPR and Polarization Anistropy

We next turned to silver nanoprisms to determine their polarization-dependent LSPR response under TIR excitation. The nanoprisms used in these experiments were flat triangular particles with reported widths of approximately 70 nm and thicknesses between 14.2 and 17.0 nm.[47]

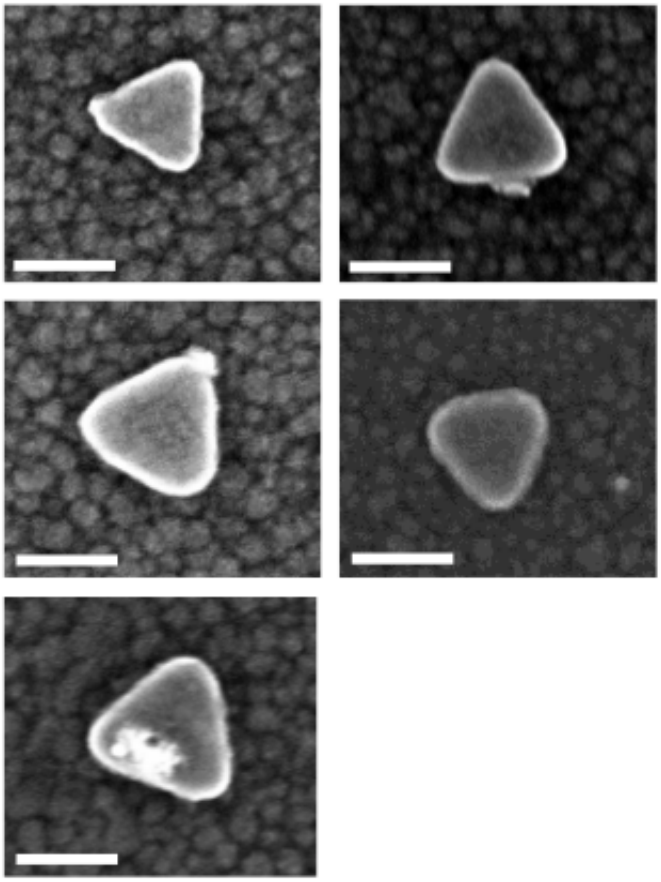

Figure 3.6: SEM images, taken at 30.0 kV, of silver triangular nanoprisms. Variation in size, tip sharpness, and the presence of defects is expected in single nanoparticle experiments.

These structures are not expected to be excited by the *z*-component of the evanescent field, making them interesting candidates for these studies.[6,77] Previous work from Sönnichsen and co-workers showed LSPR data for a silver nanoprism with a wavelength-dependent polarization response, but the corresponding LSPR spectrum was double-peaked, which is unusual for single nanoprisms.[36,78] Moreover, these data lacked structure correlation, so there was no straightforward means of comparing the polarized response to the orientation of the triangle. Here, we hoped to determine whether the use of an anisotropic excitation field would yield information about the orientation of an isotropic scatterer, using wavelength- and polarization-resolved TIR excitation. SEM images are provided for proof of principle via structure correlation, but are not necessary for future applications of this all-optical technique.

Previously, we described the nanoprisms as pseudoisotropic due to their expected polarization-insensitivity under traditional dark field scattering. To verify this, we measured the scattering response of a single silver nanoprism using traditional dark field scattering, while rotating the polarization of the excitation light.[79] For a purely isotropic nanostructure, we would expect the intensity data as a function of excitation angle to appear circular when plotted in polar coordinates.[80] Figure 3.7 shows the resulting polarization-dependent scattering of a nanoprism under traditional dark field excitation. At all excitation wavelengths shown in Figure 3.7B–E, the polarization response mirrors the response of a typical isotropic scatterer. This is typical for all silver triangular nanoprisms studied under traditional dark field scattering. As a result, the designation of nanoprisms as pseudoisotropic within the sample plane is reasonable. Moreover, these data indicate that there is no way to determine the orientation of the nanoprism within the sample plane using this approach.

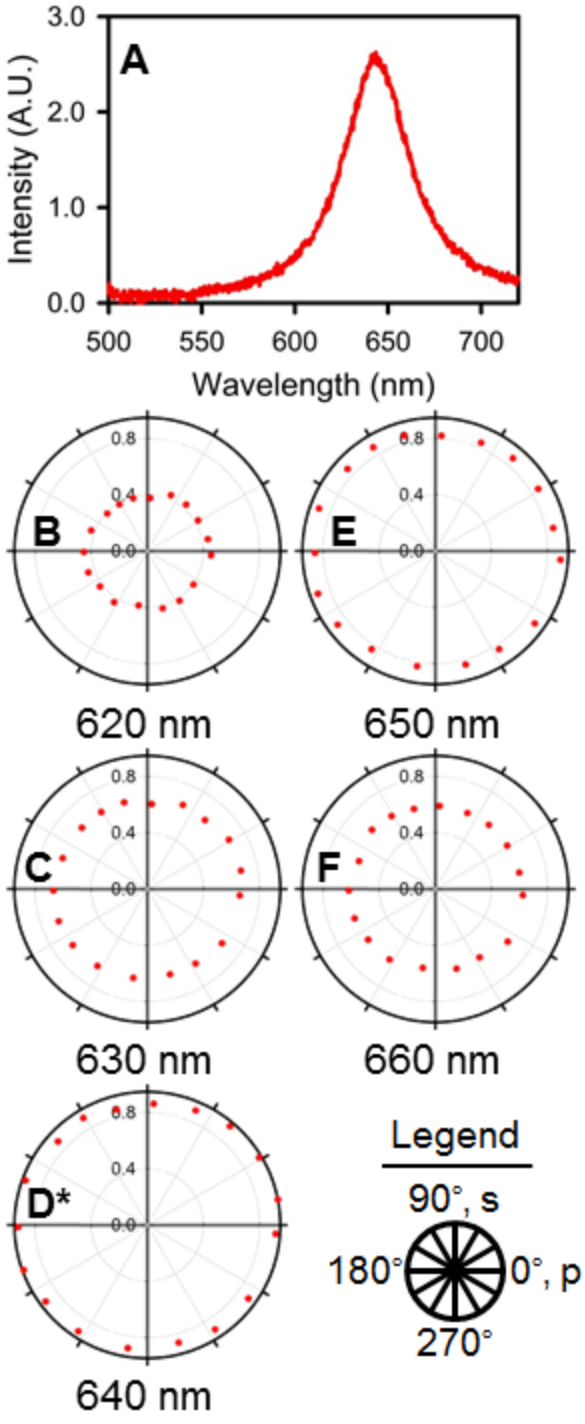
A
Intensity (A.U.)
3.0
2.0
1.0
0.0
500
550
600
650
700
Wavelength (nm)
B
620 nm
E
650 nm
C
630 nm
F
660 nm
D*
640 nm
0.8
0.4
0.0
Legend
90°, s
180°
0°, p
270°

Figure 3.7

Figure 3.7: LSPR spectrum (A) and associated wavelength-dependent polarization anisotropy plots (B–E) for a representative silver triangular nanoprism collected using traditional dark field scattering techniques.

Next, we examined the silver nanoprisms using TIR dark field excitation. Figure 3.8 shows the LSPR spectra and wavelength-dependent polar plots for three different triangular nanoprisms with one perpendicular bisector aligned with the s-component of the p-polarized (0º) excitation light as determined by SEM. In each example, the polar plot taken at the wavelength closest to the plasmon resonance is labeled with a "*" for clarity. Unlike the traditional dark field scattering polar plots from Figure 3.7, the TIR data set in Figure 3.8 shows some degree of anisotropy in each polar plot, as evidenced by a preferential alignment of the polar plots toward a specific polarization angle at a given excitation wavelength. Moreover, we find that the polarization anisotropy is wavelength dependent and rotates as the excitation wavelength is tuned.

For the triangle with the LSPR spectrum shown in Figure 3.8A, we observe that the polar plots favor two primary orientations, as shown in Figure 3.8B–G. For a scattering wavelength of 640 nm, the orientation of the polar plot points along the triangular bisector highlighted in green in Figure 3.8B. This alignment plane indicates that scattering is preferentially excited when the in-plane component of the light is polarized along this axis of the nanoprism; we call this the dominant bisector for clarity. However, as the excitation wavelength is tuned to the red, the anisotropy plot rotates clockwise (Figure 3.8C,D) until it is oriented orthogonal to the dominant bisector (Figure 3.8E,F). Moreover, the polar plots show a stronger anisotropic response as the wavelength shifts to the red, as indicated by the pinching in of the polar plot toward the center. Interestingly, for 690 nm excitation light, the polar plot rotates back toward the original alignment and loses some of the associated anisotropy (Figure 3.8G).

The second triangle in Figure 3.8 shows a very similar wavelength-dependent polarization response to that of the previous example. Its LSPR maximum (Figure 3.8H) is slightly red-shifted from that of the previous nanoprism, as expected due to its larger

size;[77] however, the trends in the orientation of the polar plots track the previous example very strongly. For a scattering wavelength of 650 nm, the orientation of the polar plot is aligned with the perpendicular bisector labeled in green in Figure 3.8I; both the orientation of the dominant bisector and the polar plot agree with the data shown in Figure 3.8B. As before, when the excitation wavelength is tuned to the red, the anisotropy plot rotates clockwise (Figure 3.8J,K) until it is oriented orthogonal to the original orientation (Figure 3.8L). Under 690 nm excitation, the polar plot rotates counter-clockwise to roughly 30º and loses some of the associated anisotropy (Figure 3.8M), but this anisotropy increases at 700 nm (Figure 3.8N). Although the two triangles shown in Figure 3.8A–N do not agree perfectly, the dominant bisector and the general trends track quite well, suggesting that the anisotropic excitation field is generating a wavelength-specific orientation-dependent polarization response in these nanostructures.

The final triangle in Figure 3.8O–U is a mirror image of the first two triangles with respect to the *y*-axis, and we define the dominant bisector as the mirror image as well (Figure 3.8S), for reasons that will become clear. Because it is slightly smaller than the nanoprism in Figure 3.8B–G, its LSPR maximum (Figure 3.8O) is slightly blue-shifted from that shown in Figure 3.8A. For a scattering wavelength of 630 or 640 nm (Figure 3.8P,Q), to the blue of λ_{max} produced polar plots aligned with the dominant bisector. As the excitation wavelength is tuned to the red toward λ_{max}, the polar plot rotates clockwise (Figure 3.8R,S) until it is oriented orthogonal to the original plot orientation (Figure 3.8T,U), similar to the behavior in the previous two triangles. However, in this case, the polar plot is now aligned with the dominant bisector, rather than against it (Figure 3.8S). With the exception of the scattering under 680 nm (Figure 3.8U), the degree of anisotropy increases as the excitation wavelength is tuned to the red (Figure 3.8S, T), similar to previous examples.

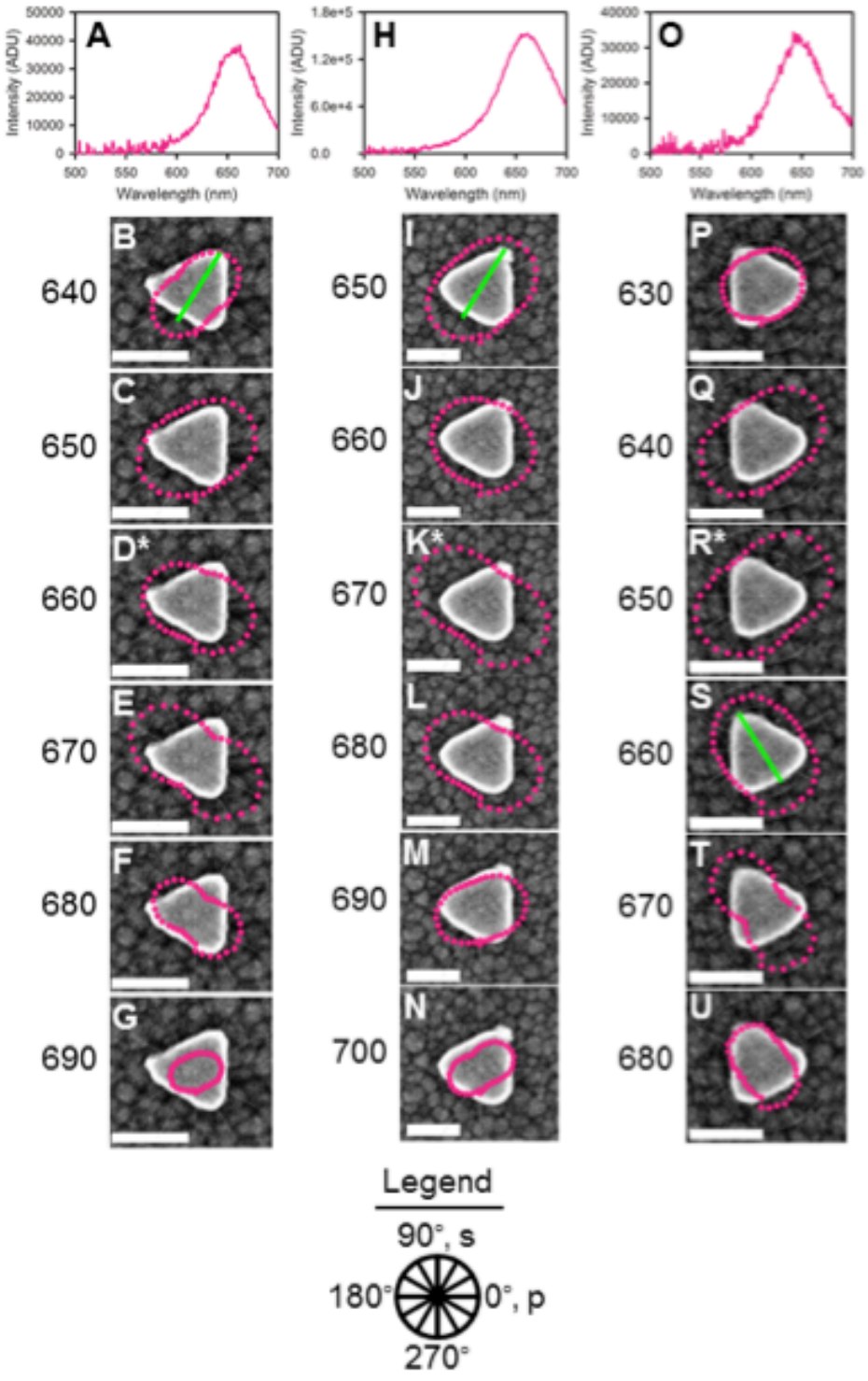
A
H
O
Intensity (ADU)
Wavelength (nm)
B
C
D*
E
F
G
I
J
K*
L
M
N
P
Q
R*
S
T
U
640
650
660
670
680
690
700
630
Legend
90°, s
180°
0°, p
270°

Figure 3.8

Figure 3.8: LSPR spectra and associated wavelength-dependent polarization anisotropy plots for three representative triangles with one perpendicular bisector aligned with the *x*-component of the p-polarized excitation (0º). Perpendicular bisectors dominating the polarization response are shown in green. (A) LSPR spectrum and (B–G) associated wavelength-dependent polarization anisotropy plots overlaid on the SEM image of the corresponding triangle. Excitation wavelengths corresponding to each polar plot are shown at left. Experimental details are as described in the text. (H) LSPR spectrum and (I–N) associated wavelength-dependent polarization anisotropy plots for a second triangle, as shown in the SEM image. (O) LSPR spectrum and (P–U) associated wavelength-dependent polarization anisotropy plots for a third triangle, as shown in the SEM images. Note that this triangle is a mirror image of the first two triangles. All scale bars are 50 nm.

All of these horizontally oriented nanoprisms (Figure 3.8) displayed wavelength-dependent polarization anisotropy with initial orientations in the 30-60º range that rotate to orthogonal orientations as the excitation wavelength is tuned to the red through λ_{max}, then rotate back towards the initial orientation under the extremes of the red. When the triangle's point faces left, the major axis of the response is oriented with the perpendicular bisector oriented at 60º when the excitation wavelength is to the blue of λ_{max}, and when the point faces right, the major axis of the response is oriented with perpendicular bisector oriented at 120º when the excitation wavelength is to the red of λ_{max}. This mirror-image preferential excitation allows distinction of left or right orientations among horizontally oriented nanoprisms. Generally, as the excitation wavelength increases from that of the LSPR maximum, the degree of anisotropy, visible in the pinching of the polar plot at excitation angles orthogonal to the major axis, also increases. We observe that this behavior is not a function of the scattered wavelength, but is rather related to the LSPR spectrum of the individual nanostructure; this is clear by comparing the polar plots at a given wavelength (i.e. 660 nm, Figure 3.8D,J,S) for each of the three individual nanostructures.

Next, we examined the wavelength- and polarization-dependent response of triangles with a perpendicular bisector oriented along the s-polarized excitation axis (*y*-axis). As before, we observe that the polar plots rotate with excitation wavelength, but the behavior is markedly different from the examples in Figure 3.8. For the first example (Figure 3.9A–G), the triangle shows near-isotropic scattering at the wavelengths closest to λ_{max} (Figure 3.9C, D), but demonstrates increased anisotropy as the scattering wavelength shifts to the blue (Figure 3.9B) or red (Figure 3.9E–G). As before, there are two dominant axes in the polar plots oriented at roughly 160˚ (Figure 3.9B) and 70˚

(Figure 3.9E–G), which show a 90˚ offset as observed previously in Figure 3.8. The 160˚ axis is aligned with the dominant bisector labeled in Figure 3.9B.

The second triangle in Figure 3.9 follows the same trend, although it is a mirror image of the first triangle with respect to the *x*-axis. Its LSPR maximum is blue-shifted relative to the previous example, as expected because it is smaller (Figure 3.9H). At a scattering wavelength of 590 nm, the polar plot shows strong anisotropy along the 160˚ axis, aligned with the dominant bisector (Figure 3.9I). This anisotropy decreases near the plasmon resonance (Figure 3.9J,K), then returns and increases as the excitation wavelength is tuned to the red (Figure 3.9L–N). The anisotropy plot rotates clockwise until it is oriented at 70˚, orthogonal to its original orientation (Figure 3.9J–N). We note that despite the fact that the two triangles are mirror images across the *x*-axis, the two show identical orientations in their wavelength-dependent polar plots, unlike the previous case for the horizontally oriented triangles (Figure 3.8).

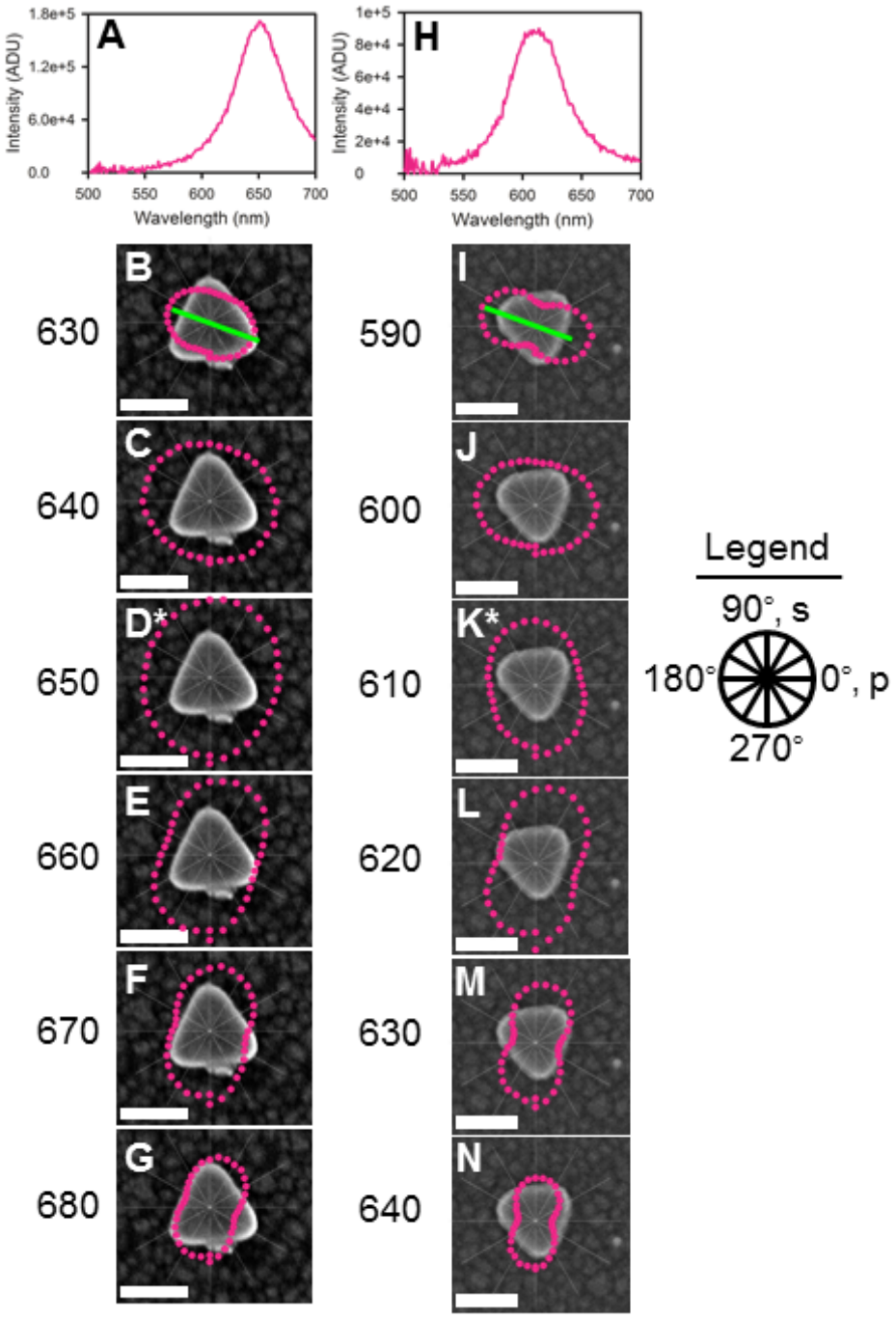
A
H
Intensity (ADU)
Wavelength (nm)
1.8e+5
1.2e+5
6.0e+4
0.0
1e+5
8e+4
6e+4
4e+4
2e+4
0
500
550
600
650
700
B
C
D*
E
F
G
I
J
K*
L
M
N
630
640
650
660
670
680
590
600
610
620
630
640
Legend
90°, s
180°
0°, p
270°

Figure 3.9

Figure 3.9: LSPR spectra and associated wavelength-dependent polarization anisotropy plots for two representative triangles with one perpendicular bisector aligned with the s-polarized excitation (90º). Perpendicular bisectors dominating the polarization response are shown in green. (A) LSPR spectrum and (B–G) associated wavelength-dependent polarization anisotropy plots overlaid on the SEM image of the corresponding triangle. Excitation wavelengths corresponding to each polar plot are shown at left. Experimental details are as described in the text. (H) LSPR spectrum and (I–N) associated wavelength-dependent polarization anisotropy plots for a second triangle, as shown in the SEM image.

In contrast to nanorods, nanoprisms do not have one clearly dominant dipole axis that would lead to an anisotropic polarization dependence. Based on DDA calculations from the Schatz group, each of the three perpendicular bisectors of an ideal triangular nanoprism can act as an in-plane dipole axis when preferentially excited.[34, 13] Moreover, plasmons can also propagate along the three edges of the nanoprism, with an LSPR frequency that is nearly identical to the mode traveling along the perpendicular bisectors.[81] At the excitation energies used, we expect to excite these two in-plane dipole modes in the triangular nanoprisms.[82,77,83] However, these dipole modes cannot be excited and therefore treated independently; thus, we expect all six in-plane dipole modes to be excited to varying extents as the polarization is rotated. Because of the symmetry of these two sets of dipole modes, when a nanoprism is excited by a rotating linearly-polarized isotropic excitation field, one would expect a pseudoisotropic scattering response from the nanoprisms, which would lead to a circular shape in the associated polar plots, as in Figure 3.5. However, due to the anisotropic nature of the TIR excitation field, we are able to break this symmetry and generate an anisotropic response from these pseudoisotropic structures, as in Figure 3.8 and Figure 3.9. As the data show, the polarization anisotropy behavior is consistent for particular orientations of the nanoprisms.

One could argue that the observed polarization dependence in the polar plots is due to defects within each nanoprism that lead to preferential excitation of one dipole axis above the others. For example, in Figure 3.8B, there is a small defect on the leftmost vertex of the triangle, which could bias the measured polarization response. However, Figure 3.8I shows a similar defect, but located on the upper right vertex of the triangle. Despite the different locations of these defect sites, the two triangles show nearly identical behavior in their wavelength-dependent polar plots, indicating that the

orientation of the nanoprism, rather than the defect location, dictates the measured response. This further supports our hypothesis that it is the anisotropic excitation field that produces the observed polarization anisotropy in these pseudoisotropic nanostructures.

Returning to our observation that the orientation of the polar plots as a function of wavelength is insensitive to the mirror flip in the case of the vertically-oriented triangles (Figure 3.9), unlike the horizontally-oriented cases (Figure 3.8), we speculate that this is due to the symmetry of the **k**-vector of the excitation field, as shown in Figure 3.1. The **k**-vector of the excitation is insensitive to a mirror flip across the *x*-axis, but approaches from the opposite edge of the sample upon a mirror flip across the *y*-axis. Thus, the high angle of excitation, in addition to the anisotropic polarization-dependent excitation field, may also contribute to the observed polarization response of the nanoprisms. This further supports our hypothesis that the anisotropic field due to TIR creates symmetry breaking in these nanostructures, generating an anisotropic scattering response.

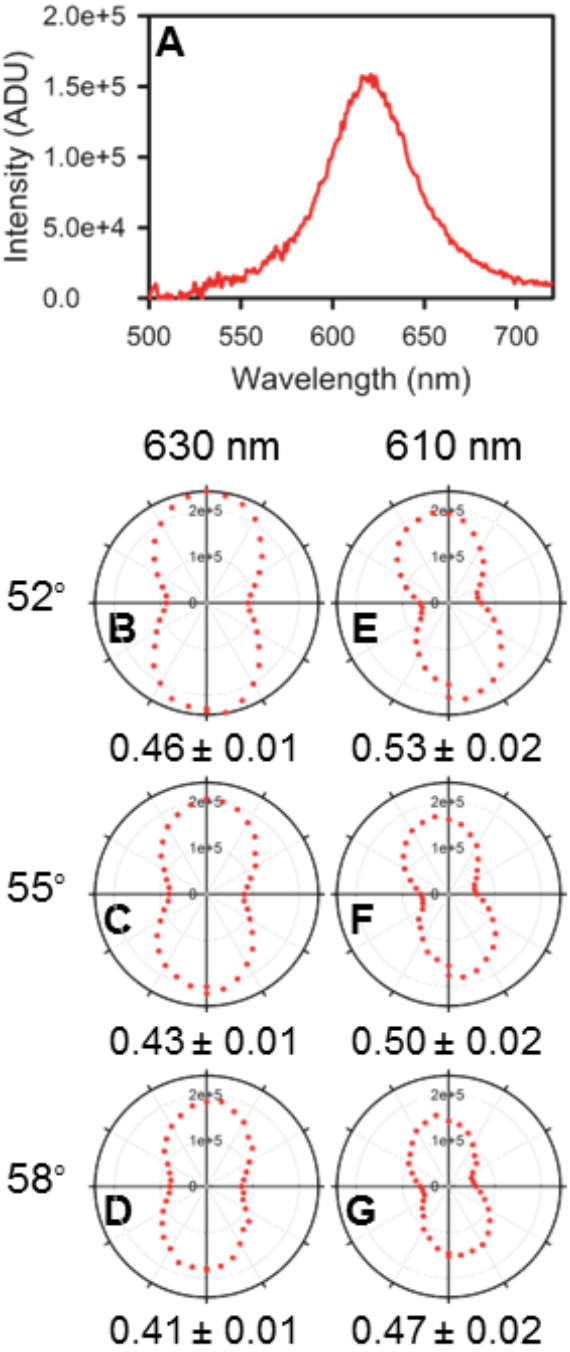
A
2.0e+5
1.5e+5
1.0e+5
5.0e+4
0.0
Intensity (ADU)
500
550
600
650
700
Wavelength (nm)
630 nm
610 nm
52°
55°
58°
B
C
D
E
F
G
0.46 ± 0.01
0.53 ± 0.02
0.43 ± 0.01
0.50 ± 0.02
0.41 ± 0.01
0.47 ± 0.02

Figure 3.10

Figure 3.10: (A) LSPR spectrum of a single silver nanoprism, summed over s- and p-polarized excitation at 52° angle of incidence. (B–G) Polar plots showing the Rayleigh scattering at (B–D) 630 nm and (E–G) 610 nm as a function of excitation polarization angle (ϕ) for varying angle of incidence, θ: (B,E) 52°, (C,F) 55°, (D,G) 58°. Values for the modulation depth, M, are shown below each plot.

To further explore how the TIR excitation affects the polarized LSPR response of a single nanoprism, we varied the angle of incidence of the TIR field and measured polar plots at two different excitation wavelengths (Figure 3.10). As the angle of incidence increases, the contribution of the *x*-component in the p-polarized light increases relative to the *z*-component (Figure 3.4). Figure 3.10 shows that as the angle of incidence increases, the orientation of the polar plot at a specific wavelength does not change, but the anisotropy decreases as evidenced by the systematic decrease in the value of the modulation depth, *M*. This is true for both wavelengths tested and is consistent with an increasingly isotropic excitation field as the angle of incidence increases. We also note that the anisotropy at 610 nm remains stronger relative to 630 nm excitation for all angles tested. This fits with our observation that as the excitation wavelength goes farther from λ_{max} to the blue or to the red, the observed anisotropy of the polarization response increases. Thus, these observations remain consistent with our claim that the anisotropic excitation field offered by TIR can generate an anisotropic scattering response in pseudoisotropic nanostructures.

3.4 CONCLUSIONS

The response of gold nanorods and silver triangular nanoprisms to an anisotropic polarization-dependent excitation field generated by through-the-objective TIR excitation was studied. The anisotropic nanorod structures behaved as they do under traditional dark field scattering with polarization optics, allowing collection of LSPR spectrum and orientation determination via preferential excitation of the longitudinal axis of the nanorod. The pseudoisotropic nanoprisms also scattered anisotropically due to the broken symmetry of the excitation, preferentially exciting one perpendicular bisector of the nanoprism in a manner dictated by its orientation. This wavelength-dependent anisotropic

response to polarization allowed us to distinguish between nanoprisms along different horizontal and vertical orientations, and within the former group, between left-pointing and right-pointing structures using diagnostic patterns. These studies indicate that it is possible to determine the single particle LSPR spectra and orientation of a single silver triangular nanoprism on a surface using wavelength- and polarization-resolved TIR excitation.

3.5 Acknowledgments

We thank the Welch Foundation (Award No. F-1699) and the Air Force Office of Scientific Research (AFOSR Award No. FA9550-09-0112) for funding. We also thank the National Science Foundation (Grant No. 0821312) for funding the Hitachi S-5500 scanning electron microscope/scanning transmission electron microscopy used in this work and Texas Materials Institute for supporting this facility.

I would also like to thank Katherine A. Willets and Kathryn M. Mayer for their assistance in writing and editing this manuscript, and Maggie L. Weber for her beautiful work in collecting correlated SEM images of the nanoparticles investigated.

3.6 References

1. Angulo, A. M.; Noguez, C.; Schatz, G. C., Electromagnetic Field Enhancement for Wedge-Shaped Metal Nanostructures. *J. Phys. Chem. Lett.* **2011,** *2* (16), 1978-1983.
2. Hao, E.; Schatz, G. C., Electromagnetic fields around silver nanoparticles and dimers. *J. Chem. Phys.* **2004,** *120* (1), 357-366.
3. Kolloch, A.; Benner, D.; Baedicker, M.; Waitz, R.; Geldhauser, T.; Boneberg, J.; Leiderer, P.; Scheer, E., Characterization and applications of plasmon fields in metal nanostructures. *Proc. SPIE 8204*, 820404-820404-10.
4. Kleinman, S. L.; Bingham, J. M.; Henry, A.-I.; Wustholz, K. L.; Van Duyne, R. P., Structural and optical characterization of single nanoparticles and single molecule SERS. *Proc. SPIE* **2010,** *7757* (Plasmonics: Metallic Nanostructures and Their Optical Properties VIII), 77570J/1-77570J/10.
5. Wokaun, A., Surface-enhanced electromagnetic processes. *Solid State Phys.* **1984,** *38*, 223-94.

6. Chen, H. J.; Shao, L.; Woo, K. C.; Ming, T.; Lin, H. Q.; Wang, J. F., Shape-Dependent Refractive Index Sensitivities of Gold Nanocrystals with the Same Plasmon Resonance Wavelength. *J. Phys. Chem. C* **2009,** *113* (41), 17691-17697.
7. Slaughter, L.; Chang, W.-S.; Link, S., Characterizing Plasmons in Nanoparticles and Their Assemblies with Single Particle Spectroscopy. *J. Phys. Chem. Lett. 2* (16), 2015-2023.
8. Guo, H.; Ruan, F.; Lu, L.; Hu, J.; Pan, J.; Yang, Z.; Ren, B., Correlating the Shape, Surface Plasmon Resonance, and Surface-Enhanced Raman Scattering of Gold Nanorods. *J. Phys. Chem. C* **2009,** *113* (24), 10459-10464.
9. Hao, E.; Schatz, G. C.; Hupp, J. T., Synthesis and optical properties of anisotropic metal nanoparticles. *J. Fluoresc.* **2004,** *14* (4), 331-341.
10. Seney, C. S.; Gutzman, B. M.; Goddard, R. H., Correlation of Size and Surface-Enhanced Raman Scattering Activity of Optical and Spectroscopic Properties for Silver Nanoparticles. *J. Phys. Chem. C* **2009,** *113* (1), 74-80.
11. Tiwari, V. S.; Oleg, T.; Darbha, G. K.; Hardy, W.; Singh, J. P.; Ray, P. C., Non-resonance SERS effects of silver colloids with different shapes. *Chem. Phys. Lett.* **2007,** *446* (1-3), 77-82.
12. Brus, L., Noble metal nanocrystals: plasmon electron transfer photochemistry and single-molecule Raman spectroscopy. *Acc Chem Res* **2008,** *41* (12), 1742-9.
13. Dadosh, T.; Sperling, J.; Bryant, G. W.; Breslow, R.; Shegai, T.; Dyshel, M.; Haran, G.; Bar-Joseph, I., Plasmonic Control of the Shape of the Raman Spectrum of a Single Molecule in a Silver Nanoparticle Dimer. *ACS Nano* **2009,** *3* (7), 1988-1994.
14. Kleinman, S. L.; Bingham, J. M.; Henry, A.-I.; Wustholz, K. L.; Van, D. R. P., Structural and optical characterization of single nanoparticles and single molecule SERS. *Proc. SPIE 7757* (Plasmonics: Metallic Nanostructures and Their Optical Properties VIII), 77570J/1-77570J/10.
15. Kleinman, S. L.; Bingham, J. M.; Henry, A.-I.; Wustholz, K. L.; Van Duyne, R. P. In *Structural and optical characterization of single nanoparticles and single molecule SERS*, Plasmonics: Metallic Nanostructures and Their Optical Properties VIII, San Diego, California, USA, SPIE: San Diego, California, USA, pp 77570J-10.
16. Slaughter, L. S.; Chang, W. S.; Swanglap, P.; Tcherniak, A.; Khanal, B. P.; Zubarev, E. R.; Link, S., *J. Phys. Chem. C* **2010,** *114*, 4934.
17. Rycenga, M.; Camargo, P. H. C.; Li, W.; Moran, C. H.; Xia, Y., Understanding the SERS Effects of Single Silver Nanoparticles and Their Dimers, One at a Time. *J. Phys. Chem. Lett. 1* (4), 696-703.
18. Angulo, A. M.; Noguez, C.; Schatz, G. C., Electromagnetic Field Enhancement for Wedge-Shaped Metal Nanostructures. *J. Phys. Chem. Lett. 2* (16), 1978-1983.
19. Haran, G., Single-Molecule Raman Spectroscopy: A Probe of Surface Dynamics and Plasmonic Fields. *Acc. Chem. Res. 43* (8), 1135-1143.
20. Haynes, C. L.; Van, D. R. P., Nanosphere Lithography: A Versatile Nanofabrication Tool for Studies of Size-Dependent Nanoparticle Optics. *J. Phys. Chem. B* **2001,** *105* (24), 5599-5611.

21. Jain, P. K.; Lee, K. S.; El-Sayed, I. H.; El-Sayed, M. A., Calculated absorption and scattering properties of gold nanoparticles of different size, shape, and composition: Applications in biological imaging and biomedicine. *Journal of Physical Chemistry B* **2006,** *110* (14), 7238-7248.
22. Kelly, K. L.; Coronado, E.; Zhao, L. L.; Schatz, G. C., The optical properties of metal nanoparticles: The influence of size, shape, and dielectric environment. *Journal of Physical Chemistry B* **2003,** *107* (3), 668-677.
23. Mulvihill, M. J.; Ling, X. Y.; Henzie, J.; Yang, P., Anisotropic Etching of Silver Nanoparticles for Plasmonic Structures Capable of Single-Particle SERS. *J. Am. Chem. Soc. 132* (1), 268-274.
24. Sonnichsen, C.; Geier, S.; Hecker, N. E.; von, P. G.; Feldmann, J.; Ditlbacher, H.; Lamprecht, B.; Krenn, J. R.; Aussenegg, F. R.; Chan, V. Z. H.; Spatz, J. P.; Moller, M., Spectroscopy of single metallic nanoparticles using total internal reflection microscopy. *Appl. Phys. Lett.* **2000,** *77* (19), 2949-2951.
25. Alekseeva, A. V.; Bogatyrev, V. A.; Khlebtsov, B. N.; Mel'nikov, A. G.; Dykman, L. A.; Khlebtsov, N. G., Gold nanorods: Synthesis and optical properties. *Colloid J.* **2006,** *68* (6), 661-678.
26. Chang, J. A.; Rhee, J. H.; Im, S. H.; Lee, Y. H.; Kim, H.-j.; Seok, S. I.; Nazeeruddin, M. K.; Gratzel, M., High-Performance Nanostructured Inorganic–Organic Heterojunction Solar Cells. *Nano Letters* **2010,** *10* (7), 2609-2612.
27. Grecco, H. E.; Martinez, O. E., Experimental determination of distance and orientation of metallic nanodimers by polarization dependent plasmon coupling. *Pap. Phys. 2*, 020010, 9 pp.
28. Sheikholeslami, S.; Jun, Y.-w.; Jain, P. K.; Alivisatos, A. P., Coupling of optical resonances in a compositionally asymmetric plasmonic nanoparticle dimer. *Nano Lett 10* (7), 2655-60.
29. Guffey, M. J.; Miller, R. L.; Gray, S. K.; Scherer, N. F., Plasmon-Driven Selective Deposition of Au Bipyramidal Nanoparticles. *Nano Lett. 11* (10), 4058-4066.
30. Sherry, L. J.; Jin, R.; Mirkin, C. A.; Schatz, G. C.; Van Duyne, R. P., Localized Surface Plasmon Resonance Spectroscopy of Single Silver Triangular Nanoprisms. *Nano Letters* **2006,** *6* (9), 2060-2065.
31. Munechika, K.; Smith, J. M.; Chen, Y.; Ginger, D. S., Plasmon Line Widths of Single Silver Nanoprisms as a Function of Particle Size and Plasmon Peak Position. *J. Phys. Chem. C* **2007,** *111* (51), 18906-18911.
32. Knight, M. W.; Wu, Y.; Lassiter, J. B.; Nordlander, P.; Halas, N. J., Substrates Matter: Influence of an Adjacent Dielectric on an Individual Plasmonic Nanoparticle. *Nano Lett.* **2009,** *9* (5), 2188-2192.
33. Knight, M. W.; Fan, J.; Capasso, F.; Halas, N. J., Influence of excitation and collection geometry on the dark field spectra of individual plasmonic nanostructures. *Optics Express 18* (3), 2579-2587.
34. Soennichsen, C.; Alivisatos, A. P., Gold Nanorods as Novel Nonbleaching Plasmon-Based Orientation Sensors for Polarized Single-Particle Microscopy. *Nano Lett.* **2005,** *5* (2), 301-304.

35. Failla, A. V.; Qian, H.; Qian, H.; Hartschuh, A.; Meixner, A. J., Orientational Imaging of Subwavelength Au Particles with Higher Order Laser Modes. *Nano Letters* **2006,** *6* (7), 1374-1378.
36. Tang, W. T.; Yew, E. Y. S.; Sheppard, C. J. R., Polarization conversion in confocal microscopy with radially polarized illumination. *Opt Lett* **2009,** *34* (14), 2147-9.
37. Hao, E.; Schatz, G. C.; Hupp, J. T., Synthesis and Optical Properties of Anisotropic Metal Nanoparticles. *J. Fluoresc.* **2004,** *14* (4), 331-341.
38. Hiep, H. M.; Nakayama, T.; Saito, M.; Yamamura, S.; Takamura, Y.; Tamiya, E., A microfluidic chip based on localized surface plasmon resonance for real-time monitoring of antigen-antibody reactions. *Jpn. J. Appl. Phys.* **2008,** *47* (2, Pt. 2), 1337-1341.
39. Live, L. S.; Masson, J.-F., Optical properties of gold particles with near micron size: localized and propagating surface plasmons. *Proc. SPIE* **2009,** *7386* (Pt. 1, Photonics North 2009), 73861M/1-73861M/7.
40. Stiles, R. L.; Willets, K. A.; Sherry, L. J.; Roden, J. M.; Van Duyne, R. P., Investigating tip-nanoparticle interactions in spatially correlated total internal reflection plasmon spectroscopy and atomic force microscopy. *J. Phys. Chem. C* **2008,** *112* (31), 11696-11701.
41. Lu, G.; Li, W.; Zhang, T.; Yue, S.; Liu, J.; Hou, L.; Li, Z.; Gong, Q., Plasmonic-Enhanced Molecular Fluorescence within Isolated Bowtie Nano-Apertures. *ACS Nano*, Ahead of Print.
42. Stranahan, S. M.; Titus, E. J.; Willets, K. A., SERS Orientational Imaging of Silver Nanoparticle Dimers. *J. Phys. Chem. Lett. 2* (21), 2711-2715.
43. Yang, S.-C.; Kobori, H.; He, C.-L.; Lin, M.-H.; Chen, H.-Y.; Li, C.; Kanehara, M.; Teranishi, T.; Gwo, S., Plasmon Hybridization in Individual Gold Nanocrystal Dimers: Direct Observation of Bright and Dark Modes. *Nano Letters 10* (2), 632-637.
44. Chang, W.-S.; Ha, J. W.; Slaughter, L. S.; Link, S., Plasmonic nanorod absorbers as orientation sensors. *Proc. Natl. Acad. Sci. U. S. A.* **2010,** *107* (7), 2781-2786, S2781/1-S2781/3.
45. Tabor, C.; Van Haute, D.; El-Sayed, M. A., Effect of Orientation on Plasmonic Coupling between Gold Nanorods. *ACS Nano* **2009,** *3* (11), 3670-3678.
46. Kaplan-Ashiri, I.; Titus, E. J.; Willets, K. A., Subdiffraction-Limited Far-Field Raman Spectroscopy of Single Carbon Nanotubes: An Unenhanced Approach. *ACS Nano 5* (2), 1033-1041.
47. Kaplan-Ashiri, I.; Titus, E. J.; Willets, K. A., Subdiffraction-Limited Far-Field Raman Spectroscopy of Single Carbon Nanotubes: An Unenhanced Approach. *ACS Nano* **2011,** *5* (2), 1033-1041.
48. Jin, R.; Cao, Y.; Mirkin, C. A.; Kelly, K. L.; Schatz, G. C.; Zheng, J. G., Photoinduced conversion of silver nanospheres to nanoprisms. *Science (Washington, DC, U. S.)* **2001,** *294* (5548), 1901-1903.
49. Quinten, M.; Pack, A.; Wannemacher, R., Scattering and extinction of evanescent waves by small particles. *Appl. Phys. B: Lasers Opt.* **1999,** *68* (1), 87-92.

50. Tian, Y.-X.; Camacho, R.; Thomsson, D.; Reus, M.; Holzwarth, A. R.; Scheblykin, I. G., Organization of Bacteriochlorophylls in Individual Chlorosomes from Chlorobaculum tepidum Studied by 2-Dimensional Polarization Fluorescence Microscopy. *J. Am. Chem. Soc.* **2011,** *133* (43), 17192-17199.
51. Traub, M. C.; Lakhwani, G.; Bolinger, J. C.; Vanden Bout, D.; Barbara, P. F., Electronic Energy Transfer in Highly Aligned MEH-PPV Single Chains. *J. Phys. Chem. B* **2011,** *115* (33), 9941-9947.
52. Adachi, T.; Brazard, J.; Chokshi, P.; Bolinger, J. C.; Ganesan, V.; Barbara, P. F., Highly Ordered Single Conjugated Polymer Chain Rod Morphologies. *J. Phys. Chem. C* **2010,** *114* (48), 20896-20902.
53. Jin, R.; Cao, Y.; Mirkin, C. A.; Kelly, K. L.; Schatz, G. C.; Zheng, J. G., Photoinduced Conversion of Silver Nanospheres to Nanoprisms. *Science* **2001,** *294* (5548), 1901-1903.
54. Sherry, L. J.; Jin, R.; Mirkin, C. A.; Schatz, G. C.; Van Duyne, R. P., Localized Surface Plasmon Resonance Spectroscopy of Single Silver Triangular Nanoprisms. *Nano Lett.* **2006,** *6* (9), 2060-2065.
55. Munechika, K.; Smith, J. M.; Chen, Y.; Ginger, D. S., Plasmon Line Widths of Single Silver Nanoprisms as a Function of Particle Size and Plasmon Peak Position. *J. Phys. Chem. C* **2007,** *111* (51), 18906-18911.
56. Heckel, J. C.; Chumanov, G., Depolarized Light Scattering From Single Silver Nanoparticles. *J. Phys. Chem. C* **2011,** *115* (15), 7261-7269.
57. Soni, J.; Purwar, H.; Ghosh, N., Quantitative polarimetry of plasmon resonant spheroidal metal nanoparticles: A Mueller matrix decomposition study. *Opt. Commun.* **2012,** *285* (6), 1599-1607.
58. Blaber, M. G.; Henry, A.-I.; Bingham, J. M.; Schatz, G. C.; Van Duyne, R. P., LSPR Imaging of Silver Triangular Nanoprisms: Correlating Scattering with Structure Using Electrodynamics for Plasmon Lifetime Analysis. *J. Phys. Chem. C* **2012,** *116* (1), 393-403.
59. Kelly, K. L.; Coronado, E.; Zhao, L. L.; Schatz, G. C., The Optical Properties of Metal Nanoparticles: The Influence of Size, Shape, and Dielectric Environment. *J. Phys. Chem. B* **2003,** *107* (3), 668-677.
60. Aherne, D.; Ledwith, D. M.; Gara, M.; Kelly, J. M., Optical properties and growth aspects of silver nanoprisms produced by a highly reproducible and rapid synthesis at room temperature. *Adv. Funct. Mater.* **2008,** *18* (14), 2005-2016.

Chapter 4: Long-range exciton migration along the MEH-PPV backbone: a common occurrence uncommonly observed[2]

4.1 INTRODUCTION

Organic electronics offer flexible substrates[22] and manufacturing benefits[23] inaccessible in inorganic devices, but compare poorly in efficiency.[84] The conjugated polymer materials used in organic light-emitting diodes (OLEDs) contain hole traps.[49] The effect of these hole traps may either increase[85,86] or decrease[87,88] device efficiency.

In OLEDs, electron transfer from excitons to trapped holes de-traps them and changes their position.[87, 89] This phenomenon takes place on the nanoscale, so its observation using far-field microscopy techniques requires point-spread function fitting.[90] An electro-optical super-resolution microscopy technique, bias-induced intensity centroid (BIC) spectroscopy, reveals distance and direction of fluorescence centroid displacement in the *x*–*y* plane of isolated poly[2-methoxy-5-(2-ethylhexyloxy)-1,4-phenylenevinylene] (MEH-PPV) polymer chains embedded in capacitor-like devices.[44] The method relies on the displacement of the overall fluorescence intensity peak, the fluorescence centroid, for one diffraction-limited spot from its unquenched position to a new position when a hole is injected to a site in the polymer chain causing local quenching. These fluorescence centroid positions were determined by fitting the point-spread function of the diffraction-limited spot to a 2-D Gaussian, and the fit comparisons were made over repeated applied bias cycles in order to lower uncertainty. This repetition also demonstrated the tendency of the hole to inject at the same site in the polymer chain.

Polarization anisotropy measurements report on local order of polymer chains and orientation in the *x*–*y* plane.[42] Correlating BIC and polarization anisotropy experiments allows investigation of whether energy transfer occurs along the polymer backbone. This

[2]Koen, K. A.; Vanden Bout, D. A. in preparation.

single molecule model system for conjugated polymer devices may offer guidance in driving polymers to adopt more advantageous conformations when used in bulk films.

In polarization anisotropy experiments, the electric field of the excitation beam is rotated in the plane of the stage of the microscope (the *x*–*y* plane), and the resulting modulation in the emission signal of excited objects is observed. In this case, fluorescence arising from single MEH-PPV molecules is modulated in response to the alignment of the excitation polarization with the projection of the molecule's net dipole into the *x*–*y* plane. When the two are parallel, a maximum in fluorescence intensity is observed, and when the two are orthogonal, a minimum in fluorescence intensity is observed. By a process described in Chapter 2, polarization anisotropy experiments reveal the orientation of the projection of each molecule's net dipole in the *x*–*y* plane, as well as the degree to which the behavior of the molecule approximates a perfect dipole or an isotropic object. The structure of high molecular weight MEH-PPV has been modeled as highly anisotropic to fit polarization anisotropy experiment data.[43] According to these models, one could reasonably expect the phase angle determined from polarization anisotropy experiments to approximate the angle at which the polymer backbone of an MEH-PPV molecule was oriented in the *x*–*y* plane.

The fluorescence intensity response of each single molecule to rotating excitation polarization was fit to a cos(2θ) function (Equation 4.1) using MATLAB scripts written in-house.

$$I = \frac{I_{max}+I_{min}}{2} - \frac{I_{max}-I_{min}}{2}\left(\cos 2\left(\theta-\phi\right)\right) \qquad (4.1)$$

The phase angle, ϕ, is the angle at which the net dipole moment of the molecule was best aligned with the excitation polarization, and the angle orthogonal to ϕ in the same plane is the angle of excitation polarization that produces the least fluorescence intensity.

Bias-modulated intensity-centroid spectroscopy (BIC) experiments previously undertaken in the Barbara group revealed long-range energy transport after the reversible injection of a single hole into an MEH-PPV chain, which suggested an extended or rod-like conformation for that molecular weight.[44] These super-resolution microscopy studies sometimes showed a fluorescence centroid trajectory that did not trace a single straight line, an unexpected result for a rod-like polymer conformation. We hypothesized that these anisotropic structures should show exciton migration along the polymer backbone, whose orientation in the *x*–*y* plane would be revealed through correlated polarization anisotropy experiments.

The point-spread function of the fluorescence image of each molecule was fit to a 2-D Gaussian, Equation 2.2, reprinted here, using MATLAB scripts written in-house.

$$I(x,y) = z_0 + I_0 e^{\left[\frac{-1}{2}\left[\left(\frac{x-x_0}{s_x}\right)^2 + \left(\frac{y-y_0}{s_y}\right)^2\right]^2\right]} \tag{2.2}$$

In Equation 2.2, each position (*x*,*y*) has an intensity, *I*, that can be modeled as the sum of the background, z_0, and the product of the peak intensity, I_0, with a Gaussian centered at x_0,y_0 that has a spread in the x-direction of s_x and a spread in the y-direction of s_y.

As the fluorescence was reversibly quenched by the applied bias, the peak of this Gaussian, called the fluorescence centroid, moved. The direction and distance of this fluorescence centroid shift were recorded. Data for each time point under the same applied bias conditions was averaged to improve signal-to-noise. The shift direction was compared to the phase angle determined by polarization anisotropy experiments. Synchronously averaged fluorescence centroid positions were plotted and the anisotropy

of this distribution was described by comparing the variance of the positions along the least squares regression line to the variance along its perpendicular bisector.

In order to carry out BIC experiments, MEH-PPV polymer chains had to be embedded at single molecule concentrations in hole-injection devices[49] (Figure 4.1A). The electrode material at the substrate was chosen to be optically transparent so that the device could be illuminated with a laser beam in an inverted microscope geometry. Fluorescence images (Figure 4.1B) were collected at high magnification on an electron-multiplying charge-coupled device (EM-CCD) detector so that each diffraction-limited spot took up as many pixels as possible for better point-spread function fitting. Partial quenching of the fluorescence intensity of the molecules was controlled by a bias applied to the device, reversibly injecting holes over many cycles (Figure 4.1C). In response to the applied bias, the position of the peak intensity, or fluorescence centroid, shifted in x (Figure 4.1D, black) and in y (Figure 4.1D, red). These intensity (Figure 4.1E) and position changes (Figure 4.1F) were synchronously averaged and the fluorescence centroid positions were re-plotted as a function of fluorescence intensity (Figure 4.1G). The highest positional certainty in fluorescence centroid positions is determined under unquenched fluorescence conditions, because uncertainty in the 2-D Gaussian peak fitting depends on signal-to-noise ratio. Therefore, lines of best fit through these fluorescence centroid maps were weighted by fluorescence intensity at each frame in the bias cycle and forced to go through the center-of-mass of the plot. The slope of this line was taken to be the overall direction of fluorescence centroid displacement, and was compared to the phase angle calculated from correlated polarization anisotropy experiments.

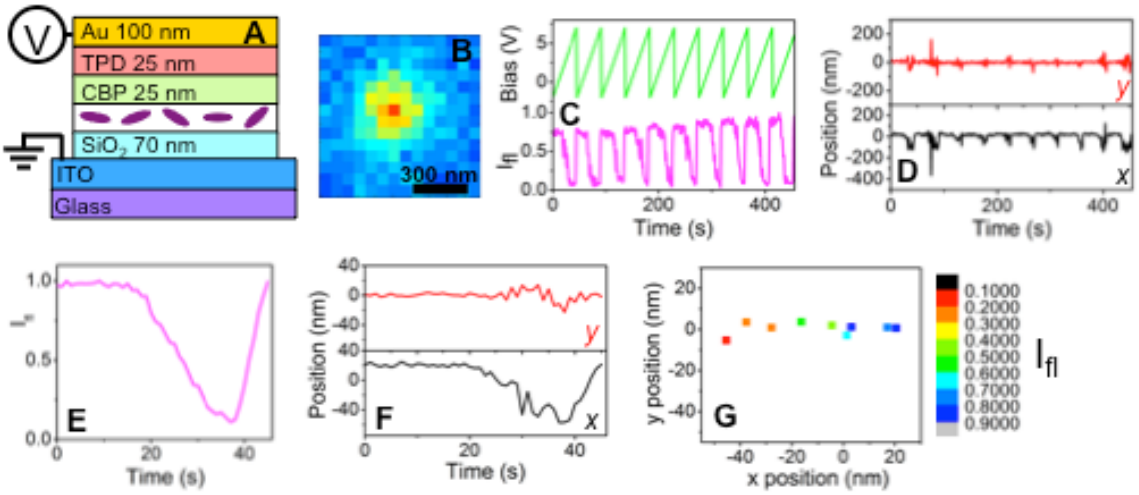

Figure 4.1: A) The device diagram (not to scale) shows that the device was constructed in layers, from four-electrode patterned ITO on glass coverslips, with a 70 nm silica layer plasma-deposited, a 25 nm PMMA layer with single chains of 1,059 kDa MEH-PPV suspended in the film at random angles spin-coated, 25 nm layers of CBP and TPD for hole-transport, and a 100 nm Au anode thermally deposited. The device was mounted on a microscope with a 488 nm laser exciting fluorescence in single MEH-PPV chains. Each chain's fluorescence image appeared as a diffraction-limited spot (B), which was fit to a 2-D Gaussian using a house-written MATLAB script. A bias applied to the device (C, green) reversibly injected holes into the MEH-PPV chains, partially quenching the fluorescence intensity of the MEH-PPV (C, pink). The position of the fit peak maximum in x (D, black) and y (D, red) was tracked through each frame in the image stack. The normalized fluorescence intensity (E) and fluorescence centroid position in x (F, black) and y (F, red) was synchronously averaged for each point in one applied bias cycle. These synchronously averaged fluorescence centroid positions are mapped as a function of normalized fluorescence intensity (G), revealing an anisotropic distribution.

4.2 Correlated polarization anisotropy and bias-induced intensity centroid spectroscopy measurements of single MEH-PPV chains

BIC experiments allowed mapping of the fluorescence centroid position as the molecule's fluorescence intensity was partially quenched under an increasingly positive applied bias, rather than at two discrete applied biases[44] (Figure 4.2A). The displacement,

d, of the fluorescence centroid from its unquenched position was calculated using the distance formula. Most often, this resulted in small overall displacements of the fluorescence centroid from most to least intense positions, and the map of the fluorescence centroid position showed little to no anisotropy (Figure 4.2B). In these cases, the slope of a line calculated using weighted least squares fitting was generated to show a direction of fluorescence centroid displacement to which the phase angle could be compared. This fit, however, could not be defined with great confidence, because the degree to which one direction is explored by the fluorescence centroid compared to other possible directions in a near-isotropic distribution of fluorescence centroid positions is slight. The difference, δ, between the direction of fluorescence centroid displacement and the phase angle, ϕ, was significantly different from zero degrees for isotropic maps such as the example shown in Figure 4.2C.

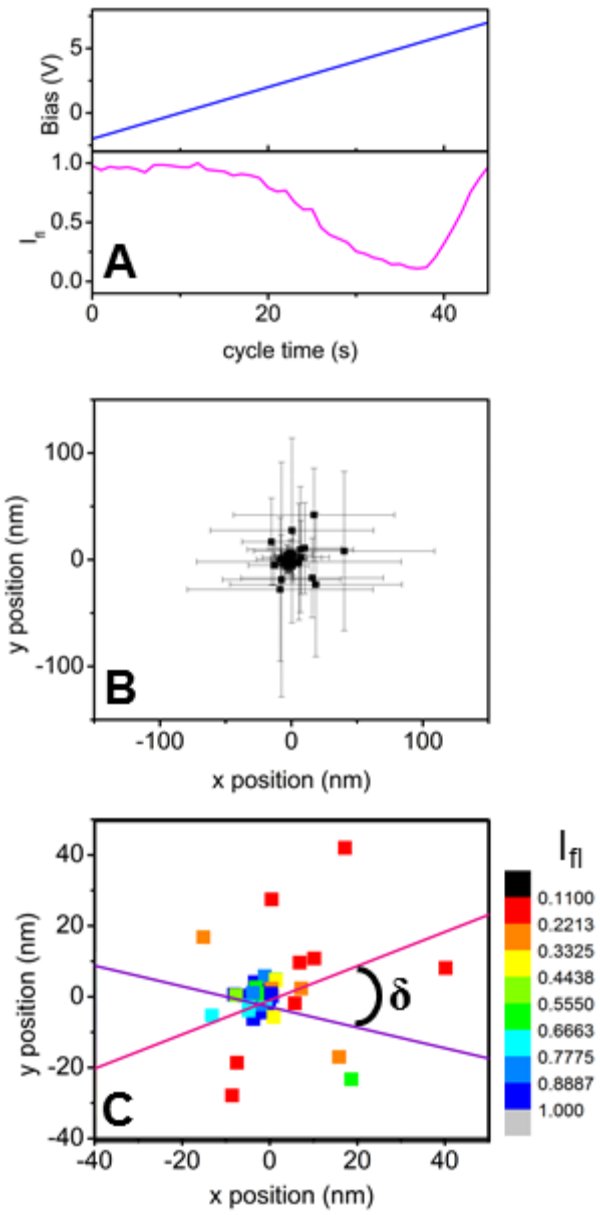
Bias (V)
5
0
1.0
0.5
0.0
I_n
A
0
20
40
cycle time (s)
100
0
-100
y position (nm)
B
-100
0
100
x position (nm)
40
20
0
-20
-40
y position (nm)
C
δ
-40
-20
0
20
40
x position (nm)
I_{fl}
0.1100
0.2213
0.3325
0.4438
0.5550
0.6663
0.7775
0.8887
1.000

Figure 4.2

Figure 4.2: A single MEH-PPV chain's synchronously-averaged, normalized fluorescence intensity (A, magenta) showed quenching as the applied sawtooth bias (A, blue) swept more positive, injecting more hole polarons from the gold anode into the conjugated polymer. At a point in this cycle with cycle time and bias varying per molecule, the fluorescence intensity began to recover. The physical meaning of this recovery point is not yet understood. The synchronously-averaged fluorescence centroid position in the plane of the microscope stage (x–y) was plotted for each time point in the applied bias cycle with error bars shown (B) and color mapped by the synchronously-averaged, normalized fluorescence intensity (C). This distribution was not highly anisotropic. The least squares fit line going through the intensity-weighted center-of-mass in the centroid position plot (C, violet) determines the displacement direction, while the phase angle determined by correlated polarization anisotropy experiments (C, magenta) implied the angle of the majority of the polymer backbone. The angle between these two lines, δ, showed poor agreement when the distribution of fluorescence centroid positions was not highly anisotropic.

Though not the most common result from BIC mapping experiments, there were instances in which large displacements of the fluorescence centroid were observed. One such example, under the same applied bias conditions as the example shown in Figure 4.2, showed more quenching (Figure 4.3A) and a more anisotropic fluorescence centroid position map (Figure 4.3B). Here, δ was clearly much smaller, indicating good agreement between the direction of fluorescence centroid displacement and the phase angle, ϕ (Figure 4.3C). This result implied that long-range exciton migration indeed can happen along the polymer backbone, as one would expect if the model of the polymer conformation as a highly anisotropic, rod-like structure[43] were accurate.

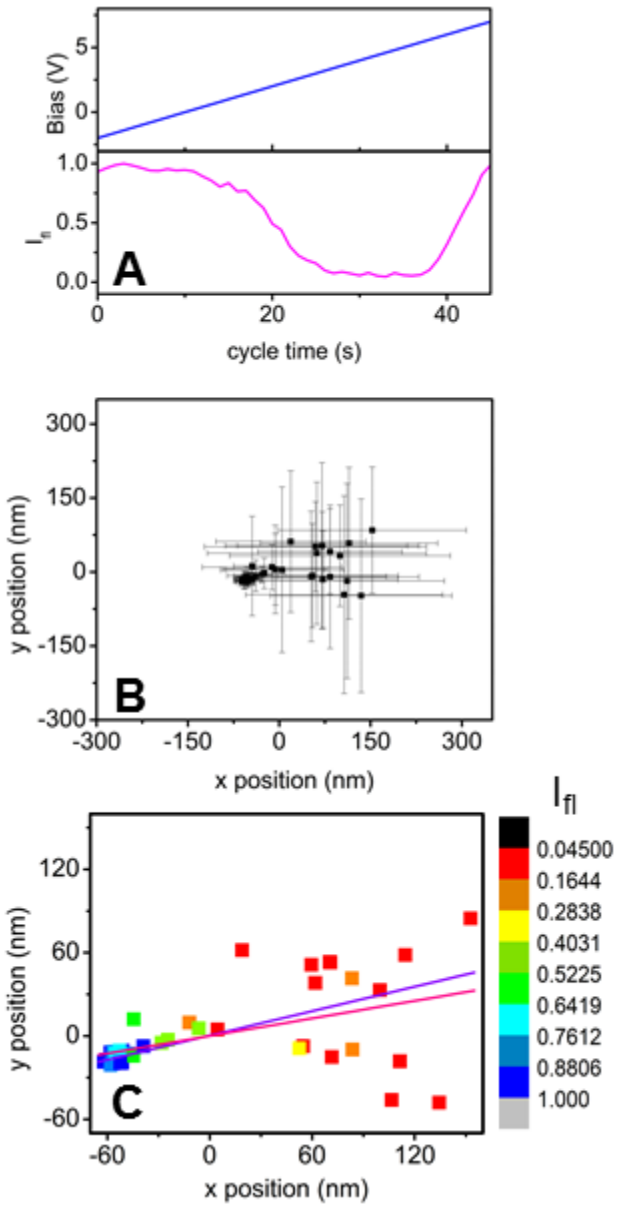
Bias (V)
5
0
1.0
0.5
0.0
I_{fl}
A
0
20
40
cycle time (s)
300
150
0
-150
-300
y position (nm)
B
-300
-150
0
150
300
x position (nm)
I_{fl}
0.04500
0.1644
0.2838
0.4031
0.5225
0.6419
0.7612
0.8806
1.000
120
60
0
-60
y position (nm)
C
-60
0
60
120
x position (nm)

Figure 4.3

Figure 4.3: A different single MEH-PPV chain in the same field of view and under the same applied sawtooth bias (A, blue) as the chain used in Figure 4.2 showed a deeper, more long-lasting quenching effect in its synchronously-averaged, normalized fluorescence intensity (A, magenta). The synchronously-averaged fluorescence centroid position maps (B, with error bars; C, color mapped by synchronously-averaged, normalized fluorescence intensity) showed a high degree of anisotropy. The least squares fit line through the intensity-weighted center-of-mass of the plot (C, violet) showed that the direction of fluorescence centroid displacement agreed well with the angle of the polymer backbone, determined by the phase angle (C, magenta) of correlated polarization anisotropy measurements. Though large displacements in the fluorescence centroid were statistically rare, they revealed that long-range energy transfer was highly directional. This supported simulated structures of MEH-PPV in highly anisotropic conformations.

We had hypothesized that this would be the dominant behavior, so we investigated why this was not more frequently observed. Taken as an ensemble, the data show that large displacements of the fluorescence centroid, d, upon partial quenching of the MEH-PPV fluorescence were observed, but that small displacements were most common (Figure 4.4A). The difference, δ, between the direction of fluorescence centroid displacement and the phase angle, ϕ, was normally distributed about zero degrees, with a peak near positive 90° (Figure 4.4B). This feature prompted closer investigation of the dependence of d and δ on the degree of anisotropy exhibited by the fluorescence centroid position map (Figure 4.4C). This anisotropy was characterized by the ratio of the variances along the intensity-weighted best fit line to the variances along its perpendicular bisector, *i.e.* the on-axis/perpendicular variance ratio. The anisotropy of the fluorescence centroid position map is higher at higher on-axis/perpendicular variance ratios. The color map on Figure 4.4C shows that larger fluorescence centroid displacements correlated with more anisotropic fluorescence centroid position maps, and tended to show good agreement between the direction of fluorescence centroid displacement and the phase angle, *i.e.* small values of δ. Where δ values deviated more from 0°, there was a correlation with smaller d values and more isotropic maps. In such cases, the uncertainty in defining the direction of fluorescence centroid displacement is greater; therefore, the uncertainty in δ is greater. To test our expectations for how often anisotropic structures should yield anisotropic fluorescence centroid maps in BIC experiments, we turned to lattice models.

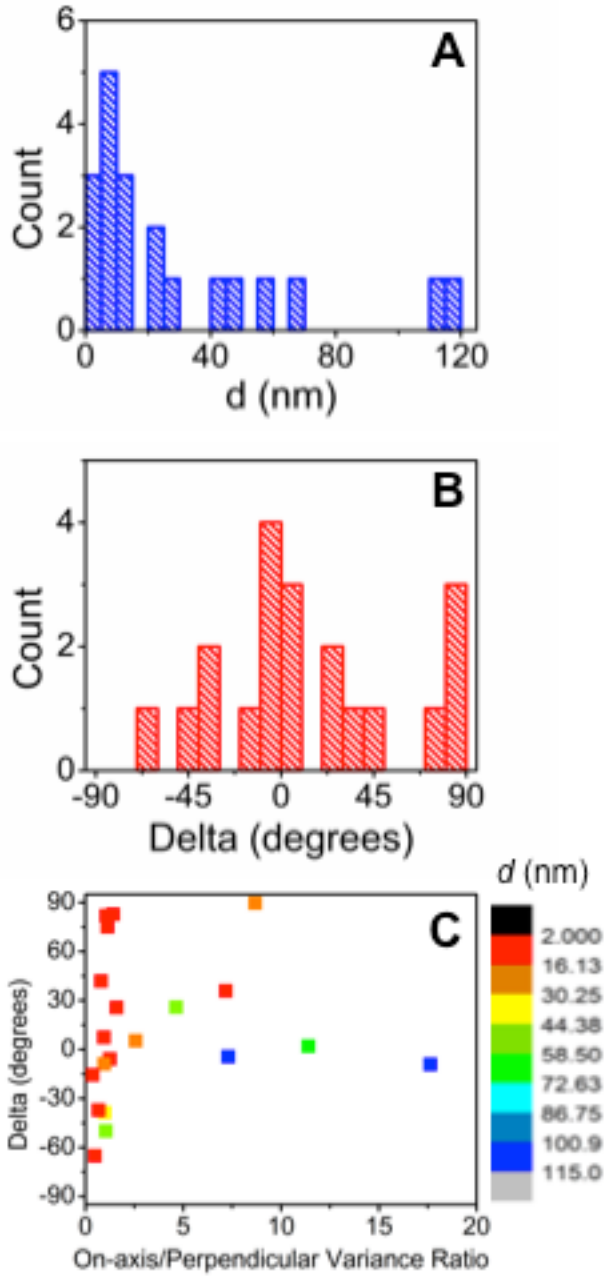
A
Count
d (nm)
B
Count
Delta (degrees)
C
Delta (degrees)
On-axis/Perpendicular Variance Ratio
d (nm)
2.000
16.13
30.25
44.38
58.50
72.63
86.75
100.9
115.0

Figure 4.4

Figure 4.4: The fluorescence centroid displacement distance, d (A), and difference between the fluorescence centroid displacement direction and the phase angle determined by polarization anisotropy, δ (B), were described for a population of single MEH-PPV chains. Small displacements were most common, as was good agreement between the polarization phase angle and the displacement direction. Typically, for a large disagreement between the polarization phase angle and the displacement direction, there was a small displacement distance, making the displacement direction ambiguous.

In these simulations, a single hole polaron was assigned a quenching radius of 40 nm because for radius values ranging 5-45 nm, 40 nm best fit the data. Each cubic nanometer voxel of the highly anisotropic (110 nm × 3 nm × 3 nm) rectangular prism (rod) lattice was treated as an independent emitter (Figure 4.5A).[44] A single hole polaron was injected into each lattice position along the length of the rod and the emitters were quenched as a function of their position relative to the hole polaron and to the hole's quenching radius. The displacement of the fluorescence centroid as a result of fluorescence quenching at that hole position relative to the position of the unquenched fluorescence centroid was plotted as a function of the hole position (Figure 4.5B). This confirmed that displacement of the fluorescence centroid as a result of quenching by a single hole was minimized at 0 nm if the hole was injected at the center of the rod due to symmetry (Figure 4.5B). The simulation also showed that this centered hole position maximized fluorescence quenching (Figure 4.5C). Histograms of the fluorescence centroid displacement and quenching depth (the fraction of fluorescence intensity quenched) data showed that displacements of 20-40 nm were statistically more likely to be observed, and that observed quenching depths (Figure 4.5E) were not tightly confined. The displacement histogram (Figure 4.5D) did not agree well with our ensemble data (Figure 4.4A). Observed quenching depths in our experiment were typically greater than 60%. These data led us to investigate the behavior of two hole polarons injected into the lattice.

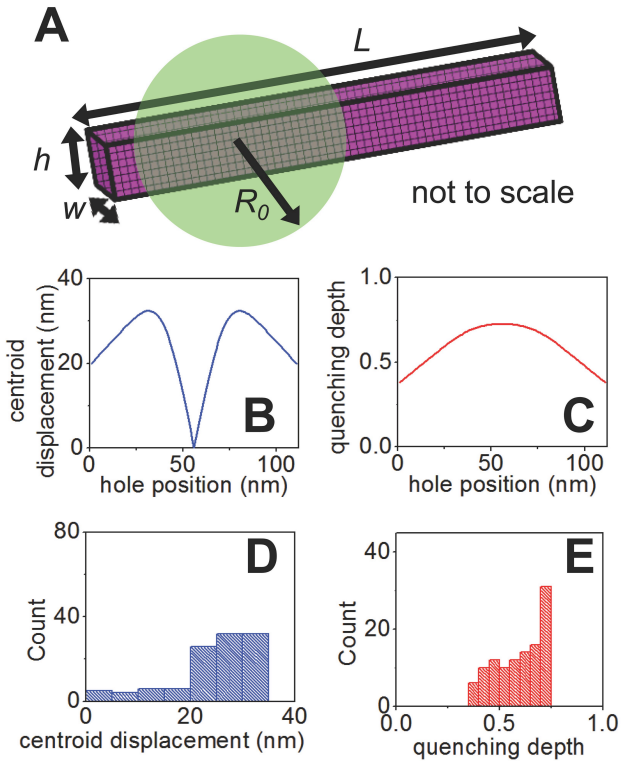

Figure 4.5: A lattice model of a single MEH-PPV chain in a rod-like conformation (A) showed the effect of hole injection at varying positions along the longitudinal axis of the rod. In this model, the rod was 110 × 3 × 3 nm (L × w × h), and the quenching radius, R_0, of the hole was 40 nm. Each point in the lattice was treated as an independent chromophore whose fluorescence was quenched as a function of its distance from the position of the hole and of the hole's quenching radius. The magnitude of the displacement of the fluorescence centroid as a function of the hole's position in L was minimal when the hole was centered in the rod (B). That was also the position that resulted in the greatest quenching of fluorescence intensity (C). When the hole was allowed to explore all available positions in L, the distribution of fluorescence centroid displacements (D) was weighted toward displacements larger than 20 nm, while the distribution of fluorescence quenching depth (E) explored a wide range.

For the multiple-quencher simulation, the position of the first hole was fixed in the lattice at three different positions, one at a time: at the center, at one-quarter of the

total length, and at the end of the rod. The second hole explored all possible longitudinal positions. Both holes were assigned the same quenching radius as in the single-hole simulation, 40 nm (Figure 4.6A). Similarly to the single-hole behavior, when both holes were centered longitudinally (but occupying different voxels because of differences in height and width), the fluorescence centroid displacement was minimized, although unlike the single quencher case, the minimum was nonzero (Figure 4.6B). As the second hole moved away from the longitudinal center, the fluorescence centroid displacement increased and decreased in a similar shape to that observed for a single hole, but with a smaller magnitude. The configuration with the first hole fixed at the center produced the highest quenching depth of the multiple-quencher cases, with a narrower range than the single-quencher case (Figure 4.6C). The histogram of the fluorescence centroid displacements shows that large displacements were most statistically likely, which does not match our observations (Figure 4.6D). The histogram of the quenching depths shows that quenching depths were observed over a narrower range than in the single-quencher case (Figure 4.6E). When the first hole was fixed at one-quarter of the length of the rod, or at the end of the rod, there were more positions the second hole could occupy that would produce small fluorescence centroid displacements, and larger displacements were observed at other positions, compared with the case in which the first hole was centered longitudinally (Figure 4.6B). This produced lower quenching depths than the case in which the first hole was centered longitudinally (Figure 4.6C). Histograms of the fluorescence centroid displacements for either case in which the first hole was fixed off-center showed a statistical likelihood of exploring especially small or large displacements (Figure 4.6F,H). Histograms of the quenching depths showed that as the first hole's fixed position moved away from the center of the rod, lower quenching depths were observed, with comparable ranges to the case in which the first hole was centered (Figure 4.6G, I).

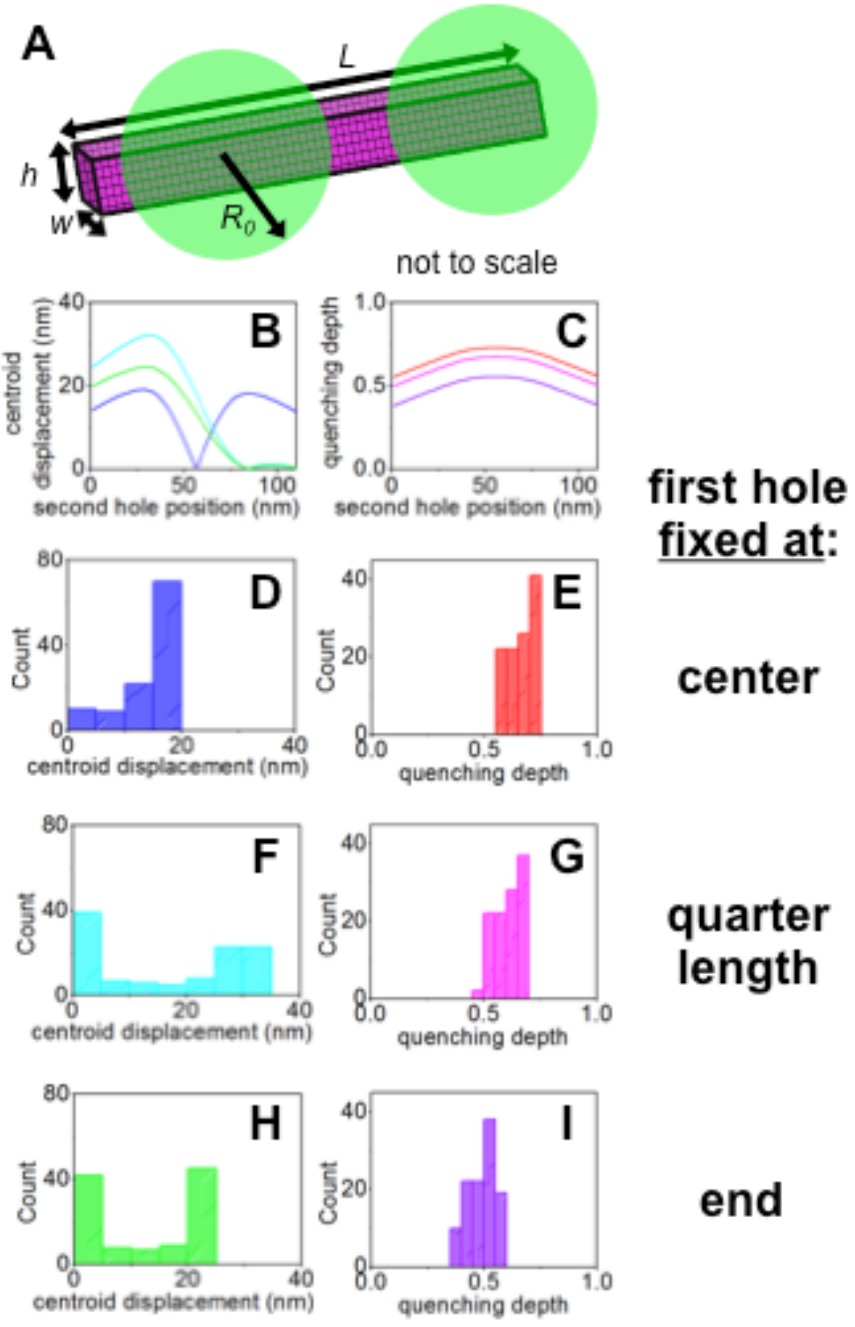
A
L
h
w
R_0
not to scale
B
centroid displacement (nm)
second hole position (nm)
C
quenching depth
second hole position (nm)
first hole fixed at:
D
Count
centroid displacement (nm)
E
Count
quenching depth
center
F
Count
centroid displacement (nm)
G
Count
quenching depth
quarter length
H
Count
centroid displacement (nm)
I
Count
quenching depth
end

Figure 4.6

Figure 4.6: A lattice model of a single MEH-PPV chain of the same dimensions as in Figure 4.5 showed the effect of two injected holes with quenching radii of 40 nm. The position of the first hole was fixed at different positions along the length of the rod, while the second hole explored every possible longitudinal position. The centroid displacement was minimized at a nonzero value when the first hole was fixed in the center of the rod (B, blue) and the second hole was also centered longitudinally (the height and width positions differ). When the first hole was fixed at one-quarter the length of the rod (B, cyan) or at the end of the rod (B, green) there was a position for the second hole that resulted in zero displacement of the fluorescence centroid, and there were more positions that resulted in exploration of extremes of fluorescence centroid displacement. The distributions of centroid displacement for each fixed position of the first hole (centered, D; one-quarter length, F; at the end, H) showed the likelihood of observing very small and very large fluorescence centroid displacements. Larger displacements were apparent when the holes were farther from the center of the rod, which met with symmetry-based expectations. The quenching depth trend was also explored for each fixed position of the first hole (centered, red, E; one-quarter length, magenta, G; at the end, violet, I). Multiple holes quenched more of the fluorescence intensity when distributed over more of the rod, not clustered together.

4.3 CONCLUSIONS

In conclusion, experimental observations and lattice simulations demonstrated that long-range exciton migration occurs along the polymer backbone, but observation of this phenomenon using BIC spectroscopy correlated with polarization anisotropy spectroscopy should be expected to be rare, because there are few hole positions that would clearly show this behavior. When two holes were injected into a lattice model chain in a rod-like conformation, with the first hole fixed at one-quarter of the length of the rod, simulations best represented experimental observations. These showed higher quenching depths than those observed in the single-quencher case, and explored the extremes of fluorescence centroid displacement.

4.4 ACKNOWLEDGMENTS

The MATLAB scripts used to analyze BIC data and to simulate the quenching behavior in holes in a rectangular lattice were written in-house by Paul F. Barbara, Joshua C. Bolinger, Matthew C. Traub, and Takuji Adachi. Special thanks to Takuji Adachi and Zhongjian Hu for training me and for helpful discussions.

4.5 REFERENCES

1. Minaev, B.; Baryshnikov, G.; Agren, H., Principles of phosphorescent organic light emitting devices. *Physical Chemistry Chemical Physics* **2014,** *16* (5), 1719-1758.
2. Kreis, J.; Schwambera, M.; Keiper, D.; Gersdorff, M.; Long, M.; Heuken, M. In *Carrier-gas enhanced vapor phase deposition for organic thin films: addressing mass manufacturing requirements for OLED devices, and overcoming existing challenges with OVPD*, 2013; pp 88291C-88291C-11.
3. Green, M. A. In *Third generation photovoltaics: assessment of progress over the last decade*, Institute of Electrical and Electronics Engineers: 2009; pp 2125-2128.
4. Bolinger, J. C.; Fradkin, L.; Lee, K.-J.; Palacios, R. E.; Barbara, P. F., Light-assisted deep-trapping of holes in conjugated polymers. *Proc. Natl. Acad. Sci. U. S. A., Early Ed.* **2009,** (Jan. 26 2009), 1-5, 5 pp.

5. Seeley, A. J. A. B.; Friend, R. H.; Kim, J.-S.; Burroughes, J. H., Trap-assisted hole injection and quantum efficiency enhancement in poly(9,9' dioctylfluorene-alt-benzothiadiazole) polymer light-emitting diodes. *J. Appl. Phys.* **2004,** *96* (12), 7643-7649.
6. Yakimov, A. V.; Savvate'ev, V. N.; Davidov, D., The role of traps in polymer-based light-emitting devices. *Synth. Met.* **2000,** *115* (1-3), 51-56.
7. Salleo, A.; Street, R. A., Light-induced bias stress reversal in polyfluorene thin-film transistors. *J. Appl. Phys.* **2003,** *94* (1), 471-479.
8. Gundlach, D. J.; Jackson, T. N.; Schlom, D. G.; Nelson, S. F., Solvent-induced phase transition in thermally evaporated pentacene films. *Appl. Phys. Lett.* **1999,** *74* (22), 3302-3304.
9. Bolinger, J.; Lee, K.-J.; Palacios, R. E.; Barbara, P. F., Detailed investigation of light induced charge injection into a single conjugated polymer chain. *J. Phys. Chem. C* **2008,** *112* (47), 18608-18615.
10. Yildiz, A.; Forkey, J. N.; McKinney, S. A.; Ha, T.; Goldman, Y. E.; Selvin, P. R., Myosin V Walks Hand-Over-Hand: Single Fluorophore Imaging with 1.5-nm Localization. *Science (Washington, DC, U. S.)* **2003,** *300* (5628), 2061-2065.
11. Bolinger, J. C.; Traub, M. C.; Adachi, T.; Barbara, P. F., Ultralong-Range Polaron-Induced Quenching of Excitons in Isolated Conjugated Polymers. *Science (Washington, DC, U. S.)* **2011,** *331* (6017), 565-567.
12. Hu, D.; Yu, J.; Wong, K.; Bagchl, B.; Rossky, P. J.; Barbara, P. F., Collapse of stiff conjugated polymers with chemical defects into ordered, cylindrical conformations. *Nature (London)* **2000,** *405* (6790), 1030-1033.
13. Adachi, T.; Brazard, J.; Chokshi, P.; Bolinger, J. C.; Ganesan, V.; Barbara, P. F., Highly Ordered Single Conjugated Polymer Chain Rod Morphologies. *J. Phys. Chem. C* **2010,** *114* (48), 20896-20902.

Chapter 5: Measurement of Exciton Migration in Single MEH-PPV Chains Using Ellipticity Modeling[3]

5.1 Introduction

In Chapter 4, single chain studies of MEH-PPV used the shift in position of the fluorescence centroid to track the direction of exciton migration. Experimental results and simulations, however, showed that observation of clear shifts in a particular direction was statistically unlikely, and comparison of that direction to the orientation measured via polarization anisotropy measurements was therefore hindered. In Chapter 5, a new method of comparing optically-established polymer chain orientation to that measured via polarization anisotropy is discussed.

Organic electronic devices are attractive for their flexibility[22] and ease of manufacture,[23] but cannot yet compete with inorganic devices in efficiency when converting light to current, or vice versa.[24] One of the paths by which conjugated polymer-based light-emitting diodes (LEDs) or photovoltaic devices may lose device efficiency is through exciton quenching by hole polarons (p^+). Upon electron transfer from the exciton to the hole polaron, the hole is detrapped and its position changes.[26, 27] The distance scale of this shift is smaller than the diffraction limit of visible light, so observation of exciton quenching by hole polarons or exciton migration in poly[2-methoxy-5-(2-ethylhexyloxy)-1,4-phenylenevinylene] (MEH-PPV) using optical microscopy techniques has either been indirect,[25] or has employed super-resolution microscopy techniques.[28, 29]

 Koen, K.A.; Clark, K.A.; Vanden Bout, D.A. Direct measurement of energy transport in organic nanosystems. *Proc. SPIE*, **2014**, *Physical Chemistry of Interfaces and Nanomaterials XIII* 9165, 91650K-91650K-6. Available at http://dx.doi.org/10.1117/12.2063866.

Exciton quenching by hole polarons has been indirectly measured in bulk samples[25] by observing the modulation of fluorescence of many molecules by injected charges and directly measured in single polymer chains as discussed in Chapter 4.[91] The single molecule techniques have the advantage of observing the heterogeneous behaviors hidden in the ensemble average and reporting on the effect of specific morphologies.

Morphology of MEH-PPV chains reported from excitation polarization spectroscopy[92] or from modeling[92, 93] suggested that a rod-like conformation was favored for varying molecular weights. The amount of fluorescence quenching observed upon the injection of a single hole polaron into a polymer chain also varied with the molecular weight: 60% quenching for 150 kDa[29], 40% quenching for 1000 kDa.[26, 94]

Point-spread function fitting techniques used to track nanometer-scale position changes of fluorophores[95] were combined with an electro-optical technique developed in the Barbara group[96] to produce bias-modulated intensity-centroid spectroscopy (BIC), used to monitor exciton migration in MEH-PPV as holes were reversibly injected into single polymer chains.[29] This study revealed remarkably long-range energy transfer in the chain, but also showed a curious change in direction of the fluorescence centroid shift when more than one hole was injected into the polymer. Due to the high aspect ratio of the rod-like polymer expected from modeling, a cylinder of about 5 nm × 200 nm,[92] this shift in direction warranted further investigation.

Direct measurements of energy transfer in artificial light-harvesting systems[97] and nanotubular J-aggregates of cyanine dye[54] showed elongated images, in which the axis of elongation matched the longer axis of the nanostructures probed. Here, we correlated excitation polarization spectroscopy measurements with BIC measurements in order to compare the longitudinal axis of the rod-like MEH-PPV chain from the polarization measurements to the axis of elongation of its diffraction-limited fluorescence image.

Experimental details are provided in Chapter 2, and the excitation schematic is shown in Figure 5.1.

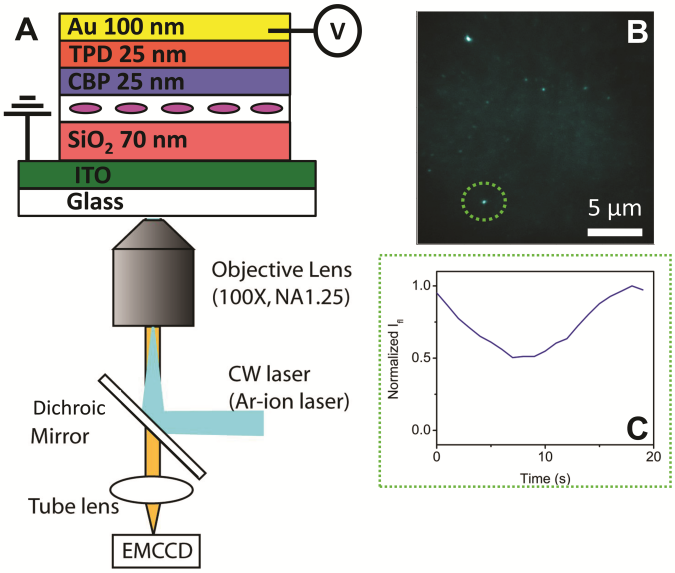

Figure 5.1. Single-molecule concentrations of MEH-PPV in a supporting PMMA film are encapsulated in a hole-injection device (A) that is optically transparent from the bottom side, allowing for observation of modulation of the fluorescence intensity of many single polymer chains simultaneously in a wide-field image MEH-PPV chains are randomly oriented within the PMMA layer. (B). This modulation is achieved through active control of the bias applied to the gold anode, injecting a varying number of holes into an MEH-PPV chain as the bias sweeps more positive, or by active control of the excitation polarization (C). The BIC experiment reports on energy transport in the polymer, while the polarization anisotropy experiment reports on the structure each chain has adopted. Correlating these experiments gives insight into the relationship between polymer morphology and energy transport.

Function generators triggered image collection in the EM-CCD to synch with two different independent variable changes: the orientation of excitation polarization and the applied potential. For excitation polarization spectroscopy, the function generators triggered an electro-optic modulator's (EOM) rotation of the linear polarization of the

excitation, so that each image frame collected by the EM-CCD corresponded to a known excitation polarization angle, while no bias was applied except during control experiments. For bias-modulated intensity-centroid spectroscopy, the function generator triggered the bias applied to the device between the gold anode and the grounded ITO electrode, so that each image frame collected by the EM-CCD corresponded to a known applied bias, while the excitation polarization was rotated so quickly as to be considered circular. In either case, a 1 s integration time was used, and the frequency of the waveforms generated by the function generators was chosen to match that time. In excitation polarization experiments, the bias applied to the EOM had a frequency of 50 mHz. In BIC, two applied bias regimes were explored because the bias at which fluorescence is quenched varies among single molecules. For a ramp from -5 to 5 V with a frame increment of 0.2 V and 51 frames per bias sweep cycle, a frequency of 20 mHz was used. For a ramp from -2 to 7 V with a frame increment of 0.2 V and 46 frames per bias sweep cycle, a frequency of 22 mHz was used. Eleven bias sweep cycles were collected, the first of which was used for background, with the excitation beam shuttered. Data from points in each of the cycles where the excitation polarization or the applied bias were the same were synchronously averaged. Nineteen cycles were synchronously averaged for excitation polarization experiments, and ten cycles were synchronously averaged for BIC experiments.

Excitation polarization spectroscopy revealed the degree to which interrogated molecules are polarized in the plane of the stage of the microscope. The pattern of fluorescence intensity modulation was fit to a $\cos(2\theta)$ function, shown in Equation 4.1, reprinted here.

$$I = \frac{I_{\max} + I_{\min}}{2} - \frac{I_{\max} - I_{\min}}{2}(\cos(2(\theta - \phi)) \qquad (4.1)$$

The ratio of the difference between the intensity maxima and minima to their sum is referred to as the modulation depth, *M*. Barring the effect of the high numerical aperture objective used in the excitation geometry, an ideal transition dipole would not be excited by light polarized orthogonally to that dipole, so the intensity minimum would be zero and the modulation depth would be 1. A system with an isotropic distribution of transition dipoles would be equally excited by all polarizations of light, so the intensity maximum and minimum would be equal and *M* would be zero. The modulation depth of a single polymer chain informs on its structure. In one limiting case, a rod-like conformation, as long as it is not oriented orthogonally to the plane of the stage, will have a projection in the plane of the stage that exhibits behavior similar to an ideal dipole, with typical *M* values of 0.7 to 0.9. An example of one single MEH-PPV chain's response to excitation polarization is shown in Figure 5.1C. In the other limiting case, a globular conformation, the polymer chain does not align its individual chromophores as strongly, so its modulation depth is smaller. This technique cannot report on the vector portion of the net transition dipole of the polymer that is oriented orthogonally to the plane of the microscope stage. Excitation polarization spectroscopy also revealed the angle, ϕ, at which the electric field of the excitation beam was best aligned with the orientation of the projection of the net transition dipole of the polymer, q, in the (*x*–*y*) plane of the stage. For a rod-like conformation, this angle represented the longitudinal axis of the rod.

Bias-induced centroid spectroscopy reversibly partially quenched the fluorescence of the molecules under pseudo-circularly polarized excitation by reversibly injecting holes that quenched part of the polymer chain's fluorescence intensity. When the contribution of this part of the molecule's fluorescence was eliminated, the peak intensity, or centroid, of its fluorescence point-spread function shifted positions. The applied waveform used here was typically a sawtooth bias sweeping more positive over

time. The sawtooth bias was applied over ten cycles. Bias-induced centroid spectroscopy showed the distance over which energy was transferred in the polymer chain, as well as the direction of that energy transfer.

The point-spread function of the fluorescence image of each molecule was fit to a bivariate normal distribution function, Equation 2, using IGOR Pro software.

$$I = \frac{1}{2\pi\sigma_x\sigma_y\sqrt{1-\rho^2}} \exp\left(\frac{-1}{2(1-\rho^2)} \left[\frac{(x-\mu_x)^2}{\sigma_x^2} + \frac{(y-\mu_y)^2}{\sigma_y^2} - \frac{2\rho(x-\mu_x)(y-\mu_y)}{\sigma_x\sigma_y} \right] \right) \quad (2)$$

The peak location in the *x*–*y* plane is given by μ_x,μ_y. The variances in the *x*- and *y*-directions, σ_x^2 and σ_y^2, are equal if the spot is circular and different if the spot is elliptical. The cross correlation coefficient, ϱ, is bounded by -1 and 1. It describes the orientation and relative asymmetry of the ellipsoidal spot. This description of the fluorescence image is given in the *x*–*y* lab frame. To determine its variance along the major and minor axes of the ellipse, and the angle of the major axis of the ellipse, a 2×2 rotation matrix was solved analytically as described by Clark *et al*.[54]

As the fluorescence was reversibly quenched by the applied bias, the peak of this bivariate normal distribution, called the fluorescence centroid, moved, and the distance was recorded. For varying points in the quenching cycle, the ratio of the major axis variance of the elliptical fluorescence image to its minor axis variance was recorded, reflecting the degree of ellipticity of the spot. The angle at which the major axis of the elliptical fluorescence image was oriented in the *x*–*y* plane was also recorded. The major axis angle was compared to the phase angle determined by polarization anisotropy experiments; the difference was called the ellipse delta. If the elongations in the

fluorescence image result from the physical extent of the long axis of the polymer this ellipse delta should be zero.

5.2 Point-spread function fitting to a bivariate normal distribution function

A single MEH-PPV chain fluoresces brightly until one or more holes are injected. The fluorescence intensity decreased as the applied bias swept more positive, Figure 5.2, top row.

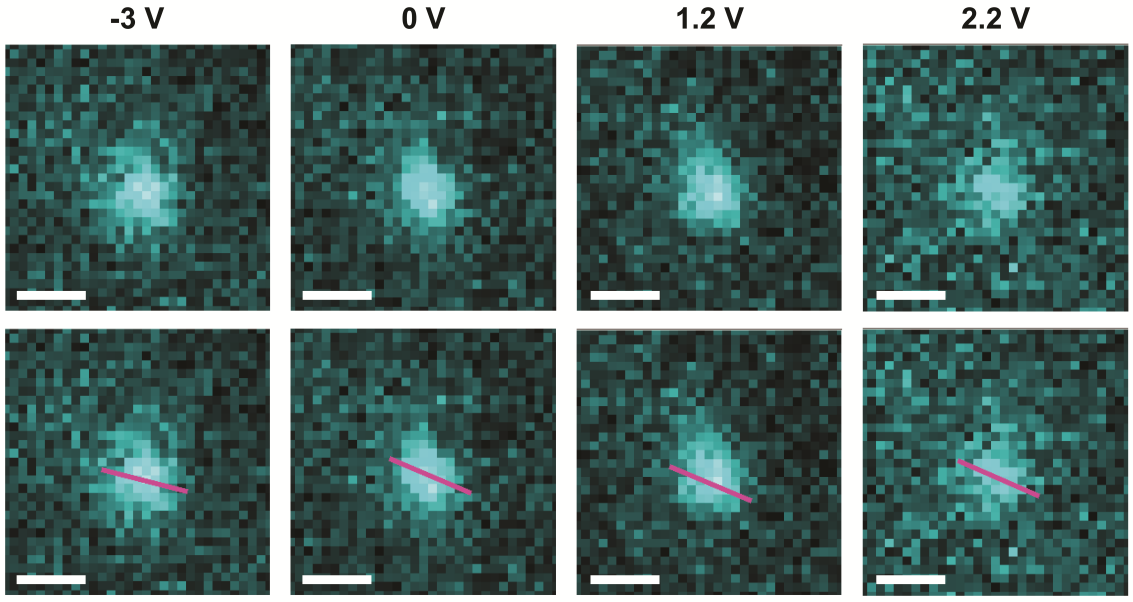

Figure 5.2: One or more holes injected into a single MEH-PPV chain partially quench the fluorescence intensity under more positive applied bias conditions. The top row provides an unoccluded view of the fluorescence images. The point-spread function of each diffraction-limited spot is fit to a 2-D bivariate Gaussian and the angle of the major axis (magenta) determined at various points in the hole-injection fluorescence quenching cycle, shown in the bottom row. The magenta line describes only the orientation, q, of the major axis; its length has no physical meaning. This orientation remains relatively consistent over many applied bias conditions, suggesting that the energy is transported in a consistent direction. All scale bars are 500 nm.

The orientation of the major axis of the elliptical spot shown in Figure 5.2 under each applied bias (bottom row, magenta) changes only slightly, from -14.2^{o}, to -22.9^{o}, to -22.5^{o}, to -23.4^{o}, from left to right in Figure 5.2. This is consistent with a rod-like conformation model of the polymer, whose aspect ratio would limit the spread of fluorescence intensity in the direction of its transverse axis. Information about this elliptical spot's fluorescence quenching under bias, its ellipse delta, and its variance ratio are also shown in Figure 5.3 (J, K, L).

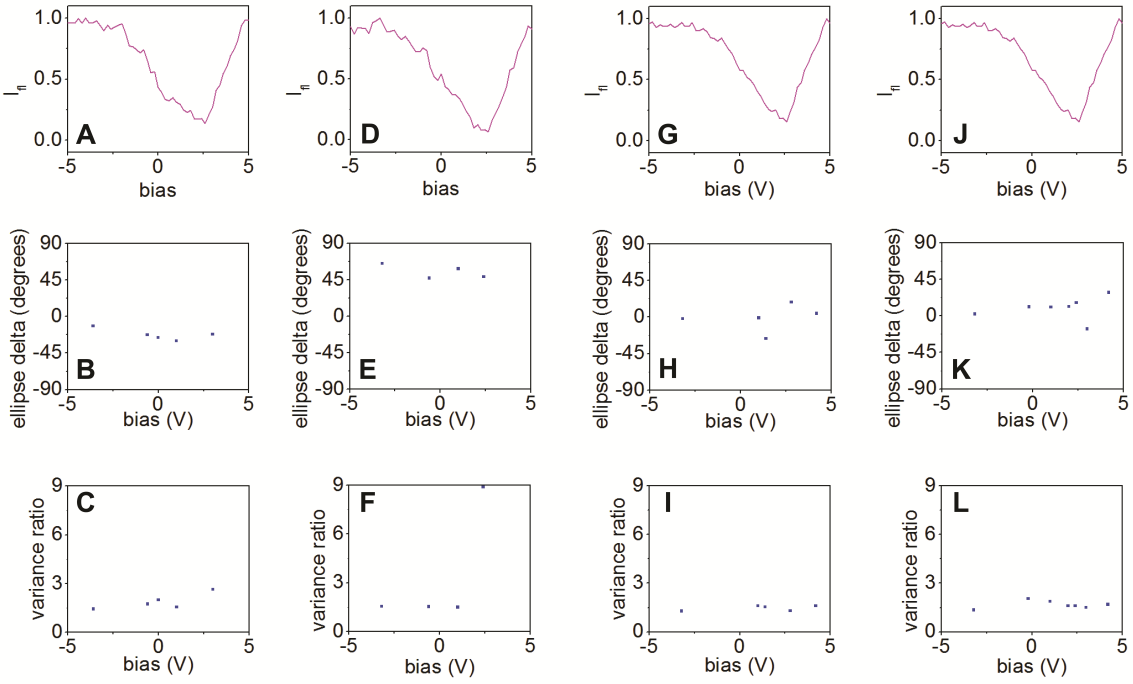

Figure 5.3: While the difference between the orientation, q, of the major axis of the elliptical spot and the phase angle, ϕ, determined by excitation polarization spectroscopy, referred to as the ellipse delta (B, E, H, K), doesn't change much as the fluorescence is quenched (A, D, G, J), the degree of ellipticity does. The ratio of the variance in the direction of the major axis of the elliptical spot to that in the direction of the minor axis (C, F, I, L) sometimes increases as the fluorescence intensity decreases, though not monotonically, and this behavior cannot be said to dominate with statistical certainty.

For each sawtooth cycle, the fluorescence intensity of the molecules started at its highest value. As the bias was swept more positive (in Figure 5.3, the applied bias was from -5 to 5 V), the fluorescence intensity decreased until it reached a local minimum and then began increasing again (Figure 5.3; A, D, G, J). The physical meaning of this fluorescence recovery is not yet known. The local minimum was not observed at the same applied bias for every molecule within the same wide-field image. The ellipse delta, or the difference between the orientation angle, q, of the major axis of the elliptical spot and the phase angle, ϕ, determined by excitation polarization spectroscopy, was generally centered about a fixed value across all applied biases (Figure 5.3; B, E, H, K), with some deviations from that value that did not occur in a pattern. For most molecules, this value was close to zero, indicating that the excitation polarization spectroscopy experiments and the elliptical analysis of the BIC spots concurred that there was a longitudinal axis to the molecule, and the orientation of that axis was predicted similarly by each method. In Figure 5.3E, it is clear that the consistent value of the ellipse delta is nonzero. This single chain's M value was 0.33, so it is reasonable to assume that this molecule was not in a rod-like conformation. The axis along which it had a net dipole could have differed from the axis along which fluorescence emission lengthened. The degree of ellipticity of the fluorescence point-spread function, described by their variance ratios, showed several subsets of behavior, none of which is statistically dominant. In Figure 5.3C and 5.3L, there was a local maximum in ellipticity at 0 V, when each molecule's fluorescence was quenched to about half of its maximum value. In Figure 5.3F, the ellipticity was consistent until quenching was at its strongest, when the ellipticity became especially high. In Figure 5.3I, the ellipticity was consistent across all applied biases. The ellipticity subsets in these example molecules represented those explored by single polymer chains in the data set as a whole. The sites most vulnerable to

hole-injection might have varied from molecule to molecule, and the portion of the molecule's fluorescence that was quenched would affect the degree of ellipticity.

In Figure 5.4, the δ was the difference between the direction of fluorescence centroid displacement, described in Chapter 4, and the phase angle, ϕ, determined by excitation polarization spectroscopy. The mean ellipse delta was the mean value of the ellipse delta for the frames in which it was determined, with the standard deviation shown in error bars. For many cases, the elliptical analysis proved to agree better with the polarization phase angle, i.e. give a mean ellipse delta closer to zero, than the fluorescence centroid displacement analysis did for its δ value, as seen in the -45 to 45 domain of Figure 5.4.

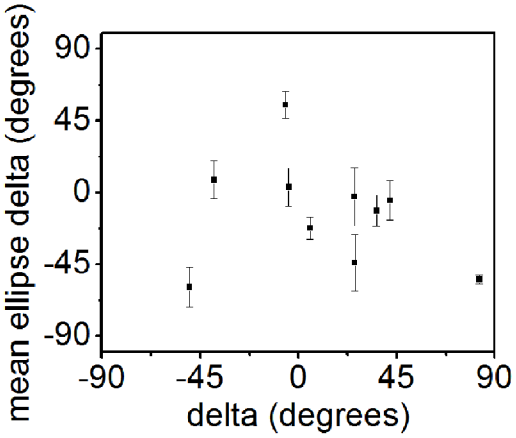

Figure 5.4: The elliptical analysis is more consistent in matching the polarization phase angle, ϕ, than the analysis of the centroid displacement direction described in Chapter 5. This means that the elliptical analysis method does not suffer from the statistical limitations of the centroid displacement direction method, which relies on the injection of multiple holes in an asymmetric configuration to reveal long-distance energy transfer along the longitudinal axis of rod-like conformation of MEH-PPV. The elliptical analysis still works for symmetric hole injection and small fluorescence centroid displacements.

5.3 Conclusions

In single polymer chains for which the fluorescence centroid displacement was small but the fluorescence intensity was strongly quenched, modeling indicates that multiple holes were quenching individual contributors in a symmetric or nearly symmetric way, such that the peak of the fluorescence envelope would not have shifted by more than 10 nm. In such cases, assignment of the displacement direction had a greater uncertainty and was more likely to show a large difference from the polarization phase angle. The elliptical analysis was especially useful for these cases.

5.4 Acknowledgments

My idea for exploring this method of analysis was prompted by a fascinating group meeting presentation by Katie A. Clark, who also taught me to use Igor.

5.5 References

1. Minaev, B.; Baryshnikov, G.; Agren, H., Principles of phosphorescent organic light emitting devices. *Physical Chemistry Chemical Physics* **2014,** *16* (5), 1719-1758.
2. Kreis, J.; Schwambera, M.; Keiper, D.; Gersdorff, M.; Long, M.; Heuken, M. In *Carrier-gas enhanced vapor phase deposition for organic thin films: addressing mass manufacturing requirements for OLED devices, and overcoming existing challenges with OVPD*, 2013; pp 88291C-88291C-11.
3. Green, M. A., Third generation photovoltaics: Ultra-high conversion efficiency at low cost. *Progress in Photovoltaics: Research and Applications* **2001,** *9* (2), 123-135.
4. Bolinger, J.; Lee, K.-J.; Palacios, R. E.; Barbara, P. F., Detailed Investigation of Light Induced Charge Injection into a Single Conjugated Polymer Chain. *The Journal of Physical Chemistry C* **2008,** *112* (47), 18608-18615.
5. Salleo, A.; Street, R. A., Light-induced bias stress reversal in polyfluorene thin-film transistors. *Journal of Applied Physics* **2003,** *94* (1), 471-479.
6. Markov, D. E.; Amsterdam, E.; Blom, P. W. M.; Sieval, A. B.; Hummelen, J. C., Accurate Measurement of the Exciton Diffusion Length in a Conjugated Polymer Using a Heterostructure with a Side-Chain Cross-Linked Fullerene Layer. *The Journal of Physical Chemistry A* **2005,** *109* (24), 5266-5274.
7. Habuchi, S.; Onda, S.; Vacha, M., Mapping the emitting sites within a single conjugated polymer molecule. *Chemical Communications* **2009,** (32), 4868-4870.

8. Bolinger, J. C.; Traub, M. C.; Adachi, T.; Barbara, P. F., Ultralong-Range Polaron-Induced Quenching of Excitons in Isolated Conjugated Polymers. *Science* **2011,** *331* (6017), 565-567.
9. Yu, J.; Hu, D.; Barbara, P. F., Unmasking Electronic Energy Transfer of Conjugated Polymers by Suppression of O2 Quenching. *Science* **2000,** *289* (5483), 1327-1330.
10. Hu, D.; Yu, J.; Wong, K.; Bagchi, B.; Rossky, P. J.; Barbara, P. F., Collapse of stiff conjugated polymers with chemical defects into ordered, cylindrical conformations. *Nature* **2000,** *405* (6790), 1030-1033.
11. Adachi, T.; Brazard, J.; Chokshi, P.; Bolinger, J. C.; Ganesan, V.; Barbara, P. F., Highly Ordered Single Conjugated Polymer Chain Rod Morphologies†. *The Journal of Physical Chemistry C* **2010,** *114* (48), 20896-20902.
12. Bolinger, J. C.; Fradkin, L.; Lee, K.-J.; Palacios, R. E.; Barbara, P. F.; Barbara, P. F., Light-Assisted Deep-Trapping of Holes in Conjugated Polymers. *Proceedings of the National Academy of Sciences of the United States of America* **2009,** *106* (5), 1342-1346.
13. Yildiz, A.; Forkey, J. N.; McKinney, S. A.; Ha, T.; Goldman, Y. E.; Selvin, P. R., Myosin V Walks Hand-Over-Hand: Single Fluorophore Imaging with 1.5-nm Localization. *Science* **2003,** *300* (5628), 2061-2065.
14. Gesquiere, A. J.; Park, S.-J.; Barbara, P. F., F–V/SMS:□ A New Technique for Studying the Structure and Dynamics of Single Molecules and Nanoparticles†. *The Journal of Physical Chemistry B* **2004,** *108* (29), 10301-10308.
15. Escalante, M.; Lenferink, A.; Zhao, Y.; Tas, N.; Huskens, J.; Hunter, C. N.; Subramaniam, V.; Otto, C., Long-Range Energy Propagation in Nanometer Arrays of Light Harvesting Antenna Complexes. *Nano Letters* **2010,** *10* (4), 1450-1457.
16. Clark, K. A.; Krueger, E. L.; Vanden Bout, D. A., Direct Measurement of Energy Migration in Supramolecular Carbocyanine Dye Nanotubes. *The Journal of Physical Chemistry Letters* **2014,** *5* (13), 2274-2282.

Appendix A: Oligomeric Interface Modifiers in Hybrid Polymer Solar Cell Prototypes Investigated by Fluorescence Voltage Spectroscopy[4]

A.1 Introduction

NOTE: The content of this Appendix, as well as the methods sections on this work in Chapter 2 (2.1.6, 2.2.3) is drawn from a collaborative project, and our publication on this topic, cited in footnote 1, was collaboratively written. The words and ideas presented here should not be considered my sole, original work, but should be attributed to all of these collaborators: especially B. Reeja Jayan, the first author, but also Robert J. Ono, David A. Vanden Bout, Christopher W. Bielawski, Arumugam Manthiram, and me.

In Chapters 4-5, optical microscopy techniques were combined with the application of an electrical potential to investigate the morphology-function relationship in single polymer chains. Here, electro-optical microscopy is used in evaluating a bulk film in a hybrid polymer solar cell prototype device.

As discussed in Chapters 4-5, electronic devices based on organic materials compare poorly in efficiency to inorganic electronics, particularly photovoltaics.[24] In addition to studying the structure-function relationship of the polymers used in organic solar cells, such as poly(3-hexylthiophene) (P3HT), the interface between donor and acceptor materials in these devices is being investigated by scientists and engineers.

Interface modifiers are thought to increase device efficiencies in a variety of ways. They may reduce the recombination rate of charge carriers, absorb more photons, improve open-circuit voltage (V_{oc}), enhance charge transfer, or increase contact between

[4] Jayan, B. R.; Koen, K. A.; Ono, R. J.; Vanden Bout, D. A.; Bielawski, C. W.; Manthiram, A., Oligomeric interface modifiers in hybrid polymer solar cell prototypes investigated by fluorescence voltage spectroscopy. Physical Chemistry Chemical Physics 2015, 17 (16), 10640-10647. – Reproduced by permission of the PCCP Owner Societies. Available at http://pubs.rsc.org/en/Content/ArticleLanding/2015/CP/C5CP00012B - !divAbstract

donor and acceptor materials. In bulk heterojunction (BHJ) devices composed of a P3HT donor and a phenyl-C_{61}-butyric acid methyl ester (PCBM) acceptor, for example, power conversion efficiency increased by 30% when a thiophene polymer, modified to contain a terminal pentafluorophenoxy moiety in its side chains, was added at 0.25 wt %.[98] Lobez and coworkers suggested that the introduction of a dipole at the P3HT-PCBM interface by the aromatic moiety was responsible for the increase in efficiency by facilitating charge separation. Other interface modifiers to the donor-acceptor interface in BHJ and hybrid polymer bilayer photovoltaic devices have also demonstrated improved device efficiencies, including dyes, small molecules, functionalized oligomers, perovskites, and antimony(III) sulfide.[38, 99-105] Experimenters in this field are still working toward mechanistic understanding of these improvements. One area of investigation is the complicated landscape for charges inside hybrid organic-inorganic solar cells, which can include energetic charge traps in the polymer (organic) layer, in the titanium(IV) oxide layer (inorganic), or at the interface between these layers. These charge traps can enhance the recombination rate of charge carriers and influence device performance.

Jayan *et al*. previously reported an indirect method of studying charge traps in a hybrid organic-inorganic interface.[106] Solar cell prototype devices were constructed with a thin bilayer of titanium(IV) oxide and regioregular or carboxylated P3HT. These devices were similar in architecture to those described in Chapter 2 (Figure 2.3), without the oligothiophene interface modifier. The optically transparent ITO electrode allowed for the excitation and observation of P3HT fluorescence response to an applied electric potential within these device prototypes so the technique is called in-device fluorescence voltage spectroscopy (ID-FVS). This technique is said to be probing the interface because the layers of each material are thinner than in typical photovoltaic devices. P3HT fluorescence reports indirectly on charge traps because excess charges act as fluorescence

quenchers, so the modulation of fluorescence intensity by an applied bias describes the injection or ejection of charge into the π–electron system of the conjugated polymer donor layer. In devices constructed using regioregular P3HT, large hysteresis in the fluorescence intensity response to applied bias was observed, but this hysteresis greatly decreased in devices constructed using carboxylated P3HT (P3HT-COOH). This suggested that the presence of the terminal carboxyl moiety decreased charge trapping, either within the polymer layer, or at the interface with titanium(IV) oxide. Carboxylated P3HT hybrid solar cell prototype devices also showed improved V_{oc} and fill factor relative to regioregular P3HT devices, implying that this decrease in charge trapping was responsible for increased device efficiency. This work showed that carboxylation was a promising avenue for interfacial modification of hybrid P3HT–TiO_2 photovoltaic devices. Synthetically, this presented a challenge, because P3HT carboxylation is incomplete and the P3HT-COOH product cannot be easily separated from the unmodified reactant P3HT. In response to this challenge, Robert J. Ono synthesized and functionalized oligothiophenes, as described in Chapter 2 (2.1.6.1).

Oligomers are advantageous over polymers in that they are monodisperse, whereas polymers have a distribution of molecular weights; and their carboxylated products can be separated from unmodified reactant via column chromatography and recrystallization. These attributes allow us to define the systems being compared more precisely and improve our understanding of the role the carboxyl moiety plays in hybrid P3HT-TiO_2 solar cell prototype devices.

A.2 Results and Discussion

Experimental methods were described in Chapter 2 (2.1.6, 2.2.3). The full results of this collaborative project are published in Jayan *et al*.[50] Here, I have focused on the results of my own contribution to the project, the ID-FVS experiments.

The thin film (~50 nm per organic material layer, ~100 nm for TiO_2 layer) bilayer device architecture and application of the interface modifier through a spin-coating step were chosen to allow for easy generalization of this technique to study the effect of varying modifiers[38, 99-101] specifically on the interface of a hybrid organic-inorganic photovoltaic device. If more conventional film thicknesses were used, the influence of phenomena in the "bulk" material would become difficult to separate from interface effects. In this device architecture, P3HT is the electron donor, or the primary hole transporter, and TiO_2 is the electron acceptor, or the primary electron transporter.

A.2.1 In-Device Fluorescence Voltage Spectroscopy (ID-FVS)

In order to understand the effect of the carboxyl moiety as an interface modifier, we compared three device types. As a control, we tested a simple P3HT–TiO_2 bilayer device, with no oligomeric interface modifier layer. In order to separate the effects of the oligomeric interfacial layer from those of the carboxyl moiety attached to the oligothiophene, we also tested a P3HT–oligothiophene–TiO_2 device and a P3HT–carboxylated oligothiophene–TiO_2 device. Figure A.1A-B show the effect of a triangular bias sweep on the fluorescence intensity observed from the P3HT layer in each type of bilayer P3HT–TiO_2 device tested.

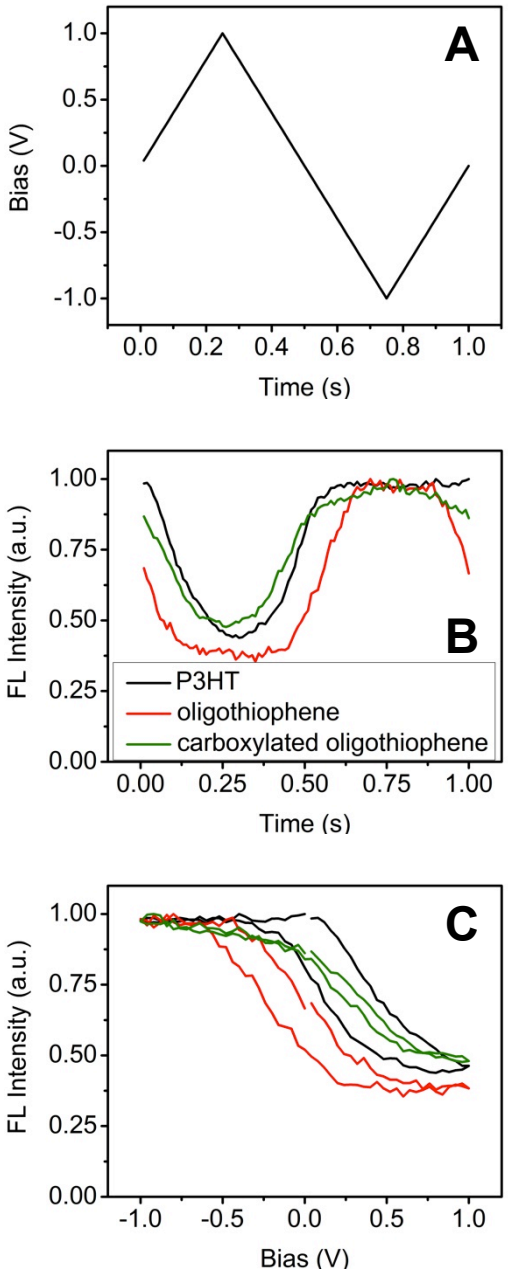

Figure A.1: (a) Triangular bias applied to the P3HT–TiO_2 bilayer devices. (b) Bias-induced fluorescence intensity as a function of time. (c) Comparison of the fluorescence intensity as a function of applied bias for P3HT–TiO_2, P3HT–oligothiophene–TiO_2, and P3HT–carboxylated oligothiophene–TiO_2 devices.

In each case, the fluorescence intensity decreased (quenched) during the application of a positive bias and recovered during the application of a negative bias. This unique polarity of the bias phenomena can be attributed to a backward electron transfer process from the TiO_2 into the P3HT layer, as previously reported.[106-108] The devices (P3HT–TiO_2, P3HT–oligothiophene–TiO_2, and P3HT–carboxylated oligothiophene–TiO_2) differed, however, in the extent of quenching observed, as shown in Table A.1.

Parameter	P3HT–TiO_2	P3HT–oligothiophene–TiO_2	P3HT–carboxylated oligothiophene–TiO_2
Median fluorescence quenching depth (%)	67	24	52
Average fluorescence quenching depth (%)	64	29	50
Standard deviation of fluorescence quenching depth (%)	18	14	10

Table A.1: Statistics of fluorescence quenching depths for each type of hybrid bilayer P3HT–TiO_2 device tested.

The primary difference observed among the device types was in the amount of hysteresis seen in the plots of fluorescence intensity as a function of applied bias, shown in Figure A.1C. A large hysteresis was clearly visible in the case of P3HT–TiO_2 bilayer devices (Figure A.1C, black), which decreased slightly when an unmodified oligothiophene layer was introduced at the P3HT–TiO_2 interface (Figure A.1C, red). The biggest change was observed upon introducing carboxylated oligothiophenes at the P3HT–TiO_2 interface, as in this case the hysteresis was almost completely eliminated

(Figure A.1C, green). This confirms previously reported results from this collaboration with carboxylated polythiophenes (P3HT-COOH), where hysteresis was also observed to greatly diminish relative to control devices.[106] Wide-field fluorescence images, shown in Figure A.2, reveal the degree of aggregation in the P3HT layer spun on top of TiO_2 layers modified with unmodified and carboxylated oligothiophenes, indicating that devices with carboxylated oligothiophene interface modifiers have a smoother, less aggregated P3HT layer.

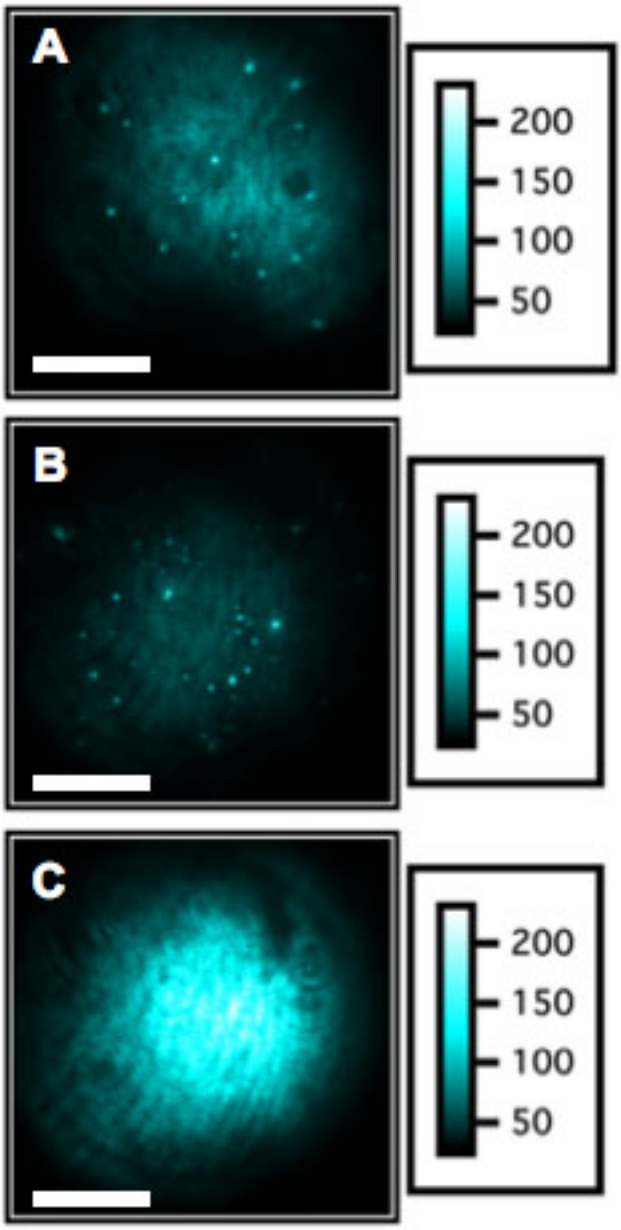

Figure A.2: Wide-field fluorescence images of P3HT layer for devices made with (A) P3HT–TiO_2 without an interface modifier (B) P3HT–oligothiophene–TiO_2 (C) P3HT–carboxylated oligothiophene–TiO_2. All scale bars are 300 μm and all intensity scales are the same (arbitrary units).

B. Reeja Jayan evaluated the V_{oc} and fill factor of the devices tested via ID-FVS (data not shown in this Appendix) and found that devices made with carboxylated

oligothiophene interface modifiers not only showed the smallest hysteresis (established by calculating the absolute area enclosed by the curve), but also showed the highest V_{oc} and fill factor when compared with P3HT–TiO_2 bilayer devices without an interface modifier.[50] This correlation between optical and electrical means of evaluating photovoltaic devices suggests that ID-FVS can be used as a diagnostic tool to study charge injection, transport, or trapping at interfaces within polymer solar cells.

A.2.2 Morphology and Surface Coverage

The terminal carboxyl moieties on the oligothiophene interface modifiers may improve photovoltaic device efficiency in hybrid P3HT–TiO_2 bilayer devices in one or more ways. First, based on our own observations of decreased aggregation in the P3HT layer when carboxylated oligothiophenes are introduced, and based on the observations of others, it is suggested that the presence of carboxyl moieties may promote the formation of a smooth, uniform, modifying layer on the TiO2 surface.[109] Aggregates in the P3HT layer provide shunting paths, which becomes apparent in low fill factor, or in extreme cases, device shorting.

Jayan also showed, through a series of X-ray photoelectron spectra (XPS) taken after varying rinse cycles with organic solvent (data not shown in this Appendix), that carboxylated oligothiophene remained on the TiO_2 surface after three rinsing steps with chlorobenzene, while unmodified oligothiophene was washed away. This result clearly demonstrates that there exists a chemical, not a physical, interaction between the carboxyl moiety and the TiO_2 surface.[109]

In addition to improved coating of the inorganic TiO_2 surface, the carboxyl moiety may also improve photovoltaic behavior through the surface passivation of charge traps.[100, 110, 111] XPS Ti 2*p* and O 1*s* spectra did not show new peaks or shifts after

exposure to carboxylated oligothiophene, though a model suggests that only 0.2-2% of the surface oxygen atoms likely to be probed by XPS were available to interact with the carboxyl moieties (data not shown in this Appendix), so one might not expect to observe changes in XPS spectra.[50] Similarly, there was no observable change in the TiO_2 absorption spectrum (data not shown in this Appendix). Taken together, these data suggest that carboxylated oligothiophene interface modifiers do not modify properties like the band gap of the TiO_2 layer. Improved adhesion between the organic and inorganic layers, however, might be responsible for the increase in fill factor observed upon introduction of carboxylated oligothiophene interface modifiers. It may also be the case that the local electric field introduced by the ordering of carboxyl dipoles at the organic-inorganic interface influences the behavior of charges at the interface and even assists in de-trapping of charges. Such improvements would become apparent in increased V_{oc}, and indeed, we observe that V_{oc} is higher in devices incorporating carboxylated oligothiophene interface modifiers.

A.2.3 ID-FVS for Mechanistic Investigations

In addition to providing an optical indicator of photovoltaic device behavior, ID-FVS can report on the thermodynamic or kinetic control of photovoltaic device behavior. In Figure A.3A, we show that the scan rate of the applied bias sweep was fixed, while the potential window varied from ±1 to ±4 V, in an ID-FVS experiment on the same P3HT–carboxylated oligothiophene–TiO_2 device. In Figure A.3C, there is no clear trend in the amount of hysteresis observed in the fluorescence intensity as a function of applied bias as a result of changing the potential window. By contrast, Figure A.3D shows that hysteresis in the fluorescence intensity as a function of applied bias increases when the

scan rate changes with the potential window and the period of the applied bias waveform is fixed (Figure A.3B).

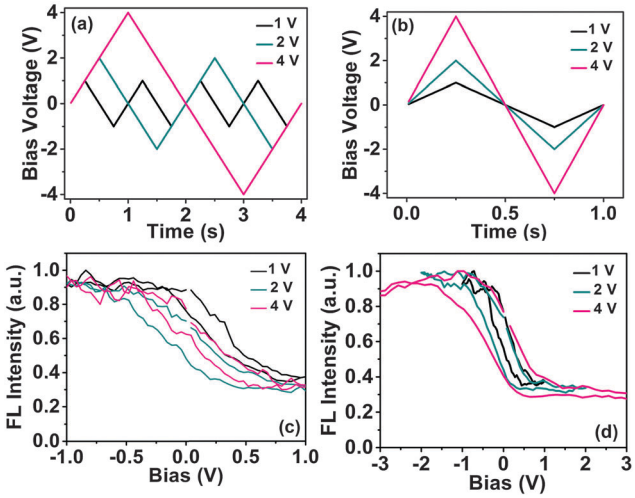

Figure A.3: Fluorescence intensity as a function of applied bias in a P3HT–carboxylated oligothiophene–TiO_2 device. (A) The potential window varied from ±1 to ±4 V with a fixed scan rate of 4 $V \cdot s^{-1}$. This gave cycle times of 0.5, 2, and 4 s for ±1, ±2, and ±4 V, respectively. (B) The scan rate varied with the potential window over a fixed cycle time of 1 s. The scan rates were 2, 8 and 16 $V \cdot s^{-1}$ for ±1, ±2, and ±4 V, respectively. Hysteresis increased with increasing scan rate (D), but showed no trend for varying potential window at a fixed scan rate (C). The legends indicate peak applied bias voltages.

Hysteresis in fluorescence intensity as a function of applied bias was typically observed to be absent in P3HT–carboxylated oligothiophene–TiO_2 devices under usual ID-FVS conditions of a ±1 V potential window and 4 $V \cdot s^{-1}$ scan rate. In modifying ID-FVS conditions, we observed hysteresis in P3HT–carboxylated oligothiophene–TiO_2 devices as the magnitude or scan rate of the applied bias increased. The results shown in Figure A.3C-D suggest that this hysteresis was primarily controlled by the rate of the bias changes and not by the magnitude of the applied potential.

ID-FVS can therefore provide insights into the mechanism of bias-dependent fluorescence modulation processes. As the rate of change of the applied bias increased,

the rate of backward electron transfer also apparently increased.[106-108] These data suggest that at these energies, these processes are dominated by kinetics, not by thermodynamics. Further, this introduction of hysteresis in response to varied experimental conditions demonstrates that the surface modifications and reduced aggregation in the P3HT layer caused by carboxylated oligothiophene interface modifiers were necessary but not sufficient for sustaining improved photovoltaic properties, especially during continued device operation. This could have implications for long-term stability of photovoltaic devices incorporating organic materials, and is worthy of further investigation.

A.3 Conclusions

Hybrid P3HT–TiO_2 bilayer solar cell prototype devices were used to evaluate the role of carboxylated oligothiophenes as interface modifiers. Devices with carboxylated oligothiophene modifying layers show improved photovoltaic properties. Correlated ID-FVS measurements show that hysteresis in fluorescence intensity as a function of applied bias is also greatly reduced in devices with carboxylated oligothiophene modifying layers, suggesting that the carboxyl moiety reduces traps, either in the polymer layer, or at the organic-inorganic interface. This hysteresis may be reintroduced, however, by varying the applied potential in ID-FVS experiments, suggesting that interfacial trapping is kinetically dominated and is not resolved by carboxylated oligothiophene interface modifiers. Collectively, theses results support the use of interface modifiers in hybrid organic-inorganic photovoltaic devices, and are expected to lead to the rational design of novel organic photovoltaic devices with long-term stability.

A.4 Acknowledgments

This work was supported as part of the program “Understanding Charge Separation and Transfer at Interfaces in Energy Materials and Devices (EFRC:CST)”, an

Energy Frontier Research Center funded by the U.S. Department of Energy Office of Science, Office of Basic Energy Sciences, under Award Number DE-SC0001091.

I would also like to reiterate that this was a collaborative project and acknowledge the contributions of my fellow collaborators, past and present: B. Reeja Jayan, Robert J. Ono, Takuji Adachi, David A. Vanden Bout, Christopher W. Bielawski, and Arumugam Manthiram.

A.5 References

24. Green, M. A., Third generation photovoltaics: Ultra-high conversion efficiency at low cost. *Progress in Photovoltaics: Research and Applications* **2001,** *9* (2), 123-135.
38. Chang, J. A.; Rhee, J. H.; Im, S. H.; Lee, Y. H.; Kim, H.-j.; Seok, S. I.; Nazeeruddin, M. K.; Gratzel, M., High-Performance Nanostructured Inorganic–Organic Heterojunction Solar Cells. *Nano Letters* **2010,** *10* (7), 2609-2612.
50. Reeja-Jayan, B.; Koen, K. A.; Ono, R. J.; Vanden Bout, D. A.; Bielawski, C. W.; Manthiram, A., Oligomeric interface modifiers in hybrid polymer solar cell prototypes investigated by fluorescence voltage spectroscopy. *Physical Chemistry Chemical Physics* **2015,** *17* (16), 10640-10647.
98. Lobez, J. M.; Andrew, T. L.; Bulović, V.; Swager, T. M., Improving the Performance of P3HT–Fullerene Solar Cells with Side-Chain-Functionalized Poly(thiophene) Additives: A New Paradigm for Polymer Design. *ACS Nano* **2012,** *6* (4), 3044-3056.
99. Lin, Y.-Y.; Chu, T.-H.; Li, S.-S.; Chuang, C.-H.; Chang, C.-H.; Su, W.-F.; Chang, C.-P.; Chu, M.-W.; Chen, C.-W., Interfacial Nanostructuring on the Performance of Polymer/TiO2 Nanorod Bulk Heterojunction Solar Cells. *Journal of the American Chemical Society* **2009,** *131* (10), 3644-3649.
100. Yu, J.; Shen, T.-L.; Weng, W.-H.; Huang, Y.-C.; Huang, C.-I.; Su, W.-F.; Rwei, S.-P.; Ho, K.-C.; Wang, L., Molecular Design of Interfacial Modifiers for Polymer-Inorganic Hybrid Solar Cells. *Advanced Energy Materials* **2012,** *2* (2), 245-252.
101. Weickert, J.; Auras, F.; Bein, T.; Schmidt-Mende, L., Characterization of Interfacial Modifiers for Hybrid Solar Cells. *The Journal of Physical Chemistry C* **2011,** *115* (30), 15081-15088.
102. Freitas, F. S.; Clifford, J. N.; Palomares, E.; Nogueira, A. F., Tailoring the interface using thiophene small molecules in TiO2/P3HT hybrid solar cells. *Physical Chemistry Chemical Physics* **2012,** *14* (34), 11990-11993.
103. Huang, Y.-C.; Yen, W.-C.; Liao, Y.-C.; Yu, Y.-C.; Hsu, C.-C.; Ho, M.-L.; Chou, P.-T.; Su, W.-F., Band gap aligned conducting interface modifier enhances the performance of thermal stable polymer-TiO2 nanorod solar cell. *Applied Physics Letters* **2010,** *96* (12), 123501.

104. Lee, M. M.; Teuscher, J.; Miyasaka, T.; Murakami, T. N.; Snaith, H. J., Efficient Hybrid Solar Cells Based on Meso-Superstructured Organometal Halide Perovskites. *Science* **2012,** *338* (6107), 643-647.
105. Liu, M.; Johnston, M. B.; Snaith, H. J., Efficient planar heterojunction perovskite solar cells by vapour deposition. *Nature* **2013,** *501* (7467), 395-398.
106. Reeja-Jayan, B.; Adachi, T.; Ono, R. J.; Vanden Bout, D. A.; Bielawski, C. W.; Manthiram, A., Effect of interfacial dipoles on charge traps in organic-inorganic hybrid solar cells. *Journal of Materials Chemistry A* **2013,** *1* (10), 3258-3262.
107. Coakley, K. M.; McGehee, M. D., Conjugated Polymer Photovoltaic Cells. *Chemistry of Materials* **2004,** *16* (23), 4533-4542.
108. Dang, X.; Hupp, J. T., Interfacial Charge-Transfer Pathways: Evidence for Marcus-Type Inverted Electron Transfer in Metal Oxide Semiconductor/Inorganic Dye Systems. *Journal of the American Chemical Society* **1999,** *121* (36), 8399-8400.
109. Ishibashi, T.-a.; Uetsuka, H.; Onishi, H., An Ordered Retinoate Monolayer Prepared on Rutile TiO2(110). *The Journal of Physical Chemistry B* **2004,** *108* (44), 17166-17170.
110. Johansson, E. M. J.; Schölin, R.; Siegbahn, H.; Hagfeldt, A.; Rensmo, H., Energy level alignment in TiO2/dipole-molecule/P3HT interfaces. *Chemical Physics Letters* **2011,** *515* (1–3), 146-150.
111. Goh, C.; Scully, S. R.; McGehee, M. D., Effects of molecular interface modification in hybrid organic-inorganic photovoltaic cells. *Journal of Applied Physics* **2007,** *101* (11), 114503.

References

1. Freakley, S.; He, Q.; Kiely, C.; Hutchings, G., Gold Catalysis: A Reflection on Where We are Now. *Catal Lett* **2015,** *145* (1), 71-79.
2. Liz-Marzán, L. M., Tailoring Surface Plasmons through the Morphology and Assembly of Metal Nanoparticles. *Langmuir* **2006,** *22* (1), 32-41.
3. Collaert, N.; Alian, A.; Arimura, H.; Boccardi, G.; Eneman, G.; Franco, J.; Ivanov, T.; Lin, D.; Loo, R.; Merckling, C.; Mitard, J.; Pourghaderi, M. A.; Rooyackers, R.; Sioncke, S.; Sun, J. W.; Vandooren, A.; Veloso, A.; Verhulst, A.; Waldron, N.; Witters, L.; Zhou, D.; Barla, K.; Thean, A. V. Y., Ultimate nano-electronics: New materials and device concepts for scaling nano-electronics beyond the Si roadmap. *Microelectronic Engineering* **2015,** *132* (0), 218-225.
4. Willets, K. A.; Van Duyne, R. P., Localized Surface Plasmon Resonance Spectroscopy and Sensing. *Annual Review of Physical Chemistry* **2007,** *58* (1), 267-297.
5. Angulo, A. M.; Noguez, C.; Schatz, G. C., Electromagnetic Field Enhancement for Wedge-Shaped Metal Nanostructures. *J. Phys. Chem. Lett.* **2011,** *2* (16), 1978-1983.
6. Hao, E.; Schatz, G. C., Electromagnetic fields around silver nanoparticles and dimers. *J. Chem. Phys.* **2004,** *120* (1), 357-366.
7. Kolloch, A.; Benner, D.; Baedicker, M.; Waitz, R.; Geldhauser, T.; Boneberg, J.; Leiderer, P.; Scheer, E., Characterization and applications of plasmon fields in metal nanostructures. *Proc. SPIE 8204*, 820404-820404-10.
8. Kleinman, S. L.; Bingham, J. M.; Henry, A.-I.; Wustholz, K. L.; Van Duyne, R. P., Structural and optical characterization of single nanoparticles and single molecule SERS. *Proc. SPIE* **2010,** *7757* (Plasmonics: Metallic Nanostructures and Their Optical Properties VIII), 77570J/1-77570J/10.
9. Wokaun, A., Surface-enhanced electromagnetic processes. *Solid State Phys.* **1984,** *38*, 223-94.
10. Chen, H. J.; Shao, L.; Woo, K. C.; Ming, T.; Lin, H. Q.; Wang, J. F., Shape-Dependent Refractive Index Sensitivities of Gold Nanocrystals with the Same Plasmon Resonance Wavelength. *Journal of Physical Chemistry C* **2009,** *113* (41), 17691-17697.
11. Slaughter, L.; Chang, W.-S.; Link, S., Characterizing Plasmons in Nanoparticles and Their Assemblies with Single Particle Spectroscopy. *J. Phys. Chem. Lett. 2* (16), 2015-2023.
12. Guo, H.; Ruan, F.; Lu, L.; Hu, J.; Pan, J.; Yang, Z.; Ren, B., Correlating the Shape, Surface Plasmon Resonance, and Surface-Enhanced Raman Scattering of Gold Nanorods. *J. Phys. Chem. C* **2009,** *113* (24), 10459-10464.
13. Hao, E.; Schatz, G. C.; Hupp, J. T., Synthesis and optical properties of anisotropic metal nanoparticles. *J. Fluoresc.* **2004,** *14* (4), 331-341.

14. Seney, C. S.; Gutzman, B. M.; Goddard, R. H., Correlation of Size and Surface-Enhanced Raman Scattering Activity of Optical and Spectroscopic Properties for Silver Nanoparticles. *J. Phys. Chem. C* **2009,** *113* (1), 74-80.
15. Tiwari, V. S.; Oleg, T.; Darbha, G. K.; Hardy, W.; Singh, J. P.; Ray, P. C., Non-resonance SERS effects of silver colloids with different shapes. *Chem. Phys. Lett.* **2007,** *446* (1-3), 77-82.
16. Brus, L., Noble metal nanocrystals: plasmon electron transfer photochemistry and single-molecule Raman spectroscopy. *Acc Chem Res* **2008,** *41* (12), 1742-9.
17. Dadosh, T.; Sperling, J.; Bryant, G. W.; Breslow, R.; Shegai, T.; Dyshel, M.; Haran, G.; Bar-Joseph, I., Plasmonic Control of the Shape of the Raman Spectrum of a Single Molecule in a Silver Nanoparticle Dimer. *ACS Nano* **2009,** *3* (7), 1988-1994.
18. Kleinman, S. L.; Bingham, J. M.; Henry, A.-I.; Wustholz, K. L.; Van, D. R. P., Structural and optical characterization of single nanoparticles and single molecule SERS. *Proc. SPIE 7757* (Plasmonics: Metallic Nanostructures and Their Optical Properties VIII), 77570J/1-77570J/10.
19. Kleinman, S. L.; Bingham, J. M.; Henry, A.-I.; Wustholz, K. L.; Van Duyne, R. P. In *Structural and optical characterization of single nanoparticles and single molecule SERS*, Plasmonics: Metallic Nanostructures and Their Optical Properties VIII, San Diego, California, USA, SPIE: San Diego, California, USA, pp 77570J-10.
20. Slaughter, L. S.; Chang, W. S.; Swanglap, P.; Tcherniak, A.; Khanal, B. P.; Zubarev, E. R.; Link, S., *J. Phys. Chem. C* **2010,** *114*, 4934.
21. Rycenga, M.; Camargo, P. H. C.; Li, W.; Moran, C. H.; Xia, Y., Understanding the SERS Effects of Single Silver Nanoparticles and Their Dimers, One at a Time. *J. Phys. Chem. Lett. 1* (4), 696-703.
22. Minaev, B.; Baryshnikov, G.; Agren, H., Principles of phosphorescent organic light emitting devices. *Physical Chemistry Chemical Physics* **2014,** *16* (5), 1719-1758.
23. Kreis, J.; Schwambera, M.; Keiper, D.; Gersdorff, M.; Long, M.; Heuken, M. In *Carrier-gas enhanced vapor phase deposition for organic thin films: addressing mass manufacturing requirements for OLED devices, and overcoming existing challenges with OVPD*, 2013; pp 88291C-88291C-11.
24. Green, M. A., Third generation photovoltaics: Ultra-high conversion efficiency at low cost. *Progress in Photovoltaics: Research and Applications* **2001,** *9* (2), 123-135.
25. Markov, D. E.; Amsterdam, E.; Blom, P. W. M.; Sieval, A. B.; Hummelen, J. C., Accurate Measurement of the Exciton Diffusion Length in a Conjugated Polymer Using a Heterostructure with a Side-Chain Cross-Linked Fullerene Layer. *The Journal of Physical Chemistry A* **2005,** *109* (24), 5266-5274.
26. Bolinger, J.; Lee, K.-J.; Palacios, R. E.; Barbara, P. F., Detailed Investigation of Light Induced Charge Injection into a Single Conjugated Polymer Chain. *The Journal of Physical Chemistry C* **2008,** *112* (47), 18608-18615.
27. Salleo, A.; Street, R. A., Light-induced bias stress reversal in polyfluorene thin-film transistors. *Journal of Applied Physics* **2003,** *94* (1), 471-479.
28. Habuchi, S.; Onda, S.; Vacha, M., Mapping the emitting sites within a single conjugated polymer molecule. *Chemical Communications* **2009,** (32), 4868-4870.

29. Bolinger, J. C.; Traub, M. C.; Adachi, T.; Barbara, P. F., Ultralong-Range Polaron-Induced Quenching of Excitons in Isolated Conjugated Polymers. *Science* **2011,** *331* (6017), 565-567.
30. Angulo, A. M.; Noguez, C.; Schatz, G. C., Electromagnetic Field Enhancement for Wedge-Shaped Metal Nanostructures. *J. Phys. Chem. Lett. 2* (16), 1978-1983.
31. Haran, G., Single-Molecule Raman Spectroscopy: A Probe of Surface Dynamics and Plasmonic Fields. *Acc. Chem. Res. 43* (8), 1135-1143.
32. Haynes, C. L.; Van, D. R. P., Nanosphere Lithography: A Versatile Nanofabrication Tool for Studies of Size-Dependent Nanoparticle Optics. *J. Phys. Chem. B* **2001,** *105* (24), 5599-5611.
33. Jain, P. K.; Lee, K. S.; El-Sayed, I. H.; El-Sayed, M. A., Calculated absorption and scattering properties of gold nanoparticles of different size, shape, and composition: Applications in biological imaging and biomedicine. *Journal of Physical Chemistry B* **2006,** *110* (14), 7238-7248.
34. Kelly, K. L.; Coronado, E.; Zhao, L. L.; Schatz, G. C., The optical properties of metal nanoparticles: The influence of size, shape, and dielectric environment. *Journal of Physical Chemistry B* **2003,** *107* (3), 668-677.
35. Mulvihill, M. J.; Ling, X. Y.; Henzie, J.; Yang, P., Anisotropic Etching of Silver Nanoparticles for Plasmonic Structures Capable of Single-Particle SERS. *J. Am. Chem. Soc. 132* (1), 268-274.
36. Sonnichsen, C.; Geier, S.; Hecker, N. E.; von, P. G.; Feldmann, J.; Ditlbacher, H.; Lamprecht, B.; Krenn, J. R.; Aussenegg, F. R.; Chan, V. Z. H.; Spatz, J. P.; Moller, M., Spectroscopy of single metallic nanoparticles using total internal reflection microscopy. *Appl. Phys. Lett.* **2000,** *77* (19), 2949-2951.
37. Alekseeva, A. V.; Bogatyrev, V. A.; Khlebtsov, B. N.; Mel'nikov, A. G.; Dykman, L. A.; Khlebtsov, N. G., Gold nanorods: Synthesis and optical properties. *Colloid J.* **2006,** *68* (6), 661-678.
38. Chang, J. A.; Rhee, J. H.; Im, S. H.; Lee, Y. H.; Kim, H.-j.; Seok, S. I.; Nazeeruddin, M. K.; Gratzel, M., High-Performance Nanostructured Inorganic–Organic Heterojunction Solar Cells. *Nano Letters* **2010,** *10* (7), 2609-2612.
39. Grecco, H. E.; Martinez, O. E., Experimental determination of distance and orientation of metallic nanodimers by polarization dependent plasmon coupling. *Pap. Phys. 2*, 020010, 9 pp.
40. Sheikholeslami, S.; Jun, Y.-w.; Jain, P. K.; Alivisatos, A. P., Coupling of optical resonances in a compositionally asymmetric plasmonic nanoparticle dimer. *Nano Lett 10* (7), 2655-60.
41. Guffey, M. J.; Miller, R. L.; Gray, S. K.; Scherer, N. F., Plasmon-Driven Selective Deposition of Au Bipyramidal Nanoparticles. *Nano Lett. 11* (10), 4058-4066.
42. Hu, D.; Yu, J.; Wong, K.; Bagchl, B.; Rossky, P. J.; Barbara, P. F., Collapse of stiff conjugated polymers with chemical defects into ordered, cylindrical conformations. *Nature (London)* **2000,** *405* (6790), 1030-1033.

43. Adachi, T.; Brazard, J.; Chokshi, P.; Bolinger, J. C.; Ganesan, V.; Barbara, P. F., Highly Ordered Single Conjugated Polymer Chain Rod Morphologies. *J. Phys. Chem. C* **2010,** *114* (48), 20896-20902.
44. Bolinger, J. C.; Traub, M. C.; Adachi, T.; Barbara, P. F., Ultralong-Range Polaron-Induced Quenching of Excitons in Isolated Conjugated Polymers. *Science (Washington, DC, U. S.)* **2011,** *331* (6017), 565-567.
45. Nikoobakht, B.; El-Sayed, M. A., Preparation and growth mechanism of gold nanorods (NRs) using seed-mediated growth method. *Chem. Mater.* **2003,** *15* (10), 1957-1962.
46. Mayer, K. M.; Lee, S.; Liao, H.; Rostro, B. C.; Fuentes, A.; Scully, P. T.; Nehl, C. L.; Hafner, J. H., A label-free immunoassay based upon localized surface plasmon resonance of gold nanorods. *ACS Nano* **2008,** *2* (4), 687-692.
47. Jin, R.; Cao, Y.; Mirkin, C. A.; Kelly, K. L.; Schatz, G. C.; Zheng, J. G., Photoinduced Conversion of Silver Nanospheres to Nanoprisms. *Science* **2001,** *294* (5548), 1901-1903.
48. Weber, M. L.; Willets, K. A., *J. Phys. Chem. Lett.* **2011,** *2*, 1766.
49. Bolinger, J. C.; Fradkin, L.; Lee, K.-J.; Palacios, R. E.; Barbara, P. F., Light-assisted deep-trapping of holes in conjugated polymers. *Proc. Natl. Acad. Sci. U. S. A., Early Ed.* **2009,** (Jan. 26 2009), 1-5, 5 pp.
50. Reeja-Jayan, B.; Koen, K. A.; Ono, R. J.; Vanden Bout, D. A.; Bielawski, C. W.; Manthiram, A., Oligomeric interface modifiers in hybrid polymer solar cell prototypes investigated by fluorescence voltage spectroscopy. *Physical Chemistry Chemical Physics* **2015,** *17* (16), 10640-10647.
51. Loewe, R. S.; Ewbank, P. C.; Liu, J.; Zhai, L.; McCullough, R. D., Regioregular, Head-to-Tail Coupled Poly(3-alkylthiophenes) Made Easy by the GRIM Method: Investigation of the Reaction and the Origin of Regioselectivity. *Macromolecules* **2001,** *34* (13), 4324-4333.
52. Tanaka, K.; Takimiya, K.; Otsubo, T.; Kawabuchi, K.; Kajihara, S.; Harima, Y., Development and Photovoltaic Performance of Oligothiophene-sensitized TiO₂ Solar Cells. *Chemistry Letters* **2006,** *35* (6), 592-593.
53. Reeja-Jayan, B.; Manthiram, A., Understanding the Improved Stability of Hybrid Polymer Solar Cells Fabricated with Copper Electrodes. *ACS Applied Materials & Interfaces* **2011,** *3* (5), 1492-1501.
54. Clark, K. A.; Krueger, E. L.; Vanden Bout, D. A., Direct Measurement of Energy Migration in Supramolecular Carbocyanine Dye Nanotubes. *The Journal of Physical Chemistry Letters* **2014,** *5* (13), 2274-2282.
55. Sherry, L. J.; Jin, R.; Mirkin, C. A.; Schatz, G. C.; Van Duyne, R. P., Localized Surface Plasmon Resonance Spectroscopy of Single Silver Triangular Nanoprisms. *Nano Letters* **2006,** *6* (9), 2060-2065.
56. Munechika, K.; Smith, J. M.; Chen, Y.; Ginger, D. S., Plasmon Line Widths of Single Silver Nanoprisms as a Function of Particle Size and Plasmon Peak Position. *J. Phys. Chem. C* **2007,** *111* (51), 18906-18911.

57. Knight, M. W.; Wu, Y.; Lassiter, J. B.; Nordlander, P.; Halas, N. J., Substrates Matter: Influence of an Adjacent Dielectric on an Individual Plasmonic Nanoparticle. *Nano Lett*. **2009,** *9* (5), 2188-2192.
58. Knight, M. W.; Fan, J.; Capasso, F.; Halas, N. J., Influence of excitation and collection geometry on the dark field spectra of individual plasmonic nanostructures. *Optics Express 18* (3), 2579-2587.
59. Soennichsen, C.; Alivisatos, A. P., Gold Nanorods as Novel Nonbleaching Plasmon-Based Orientation Sensors for Polarized Single-Particle Microscopy. *Nano Lett*. **2005,** *5* (2), 301-304.
60. Failla, A. V.; Qian, H.; Qian, H.; Hartschuh, A.; Meixner, A. J., Orientational Imaging of Subwavelength Au Particles with Higher Order Laser Modes. *Nano Letters* **2006,** *6* (7), 1374-1378.
61. Tang, W. T.; Yew, E. Y. S.; Sheppard, C. J. R., Polarization conversion in confocal microscopy with radially polarized illumination. *Opt Lett* **2009,** *34* (14), 2147-9.
62. Hao, E.; Schatz, G. C.; Hupp, J. T., Synthesis and Optical Properties of Anisotropic Metal Nanoparticles. *J. Fluoresc*. **2004,** *14* (4), 331-341.
63. Hiep, H. M.; Nakayama, T.; Saito, M.; Yamamura, S.; Takamura, Y.; Tamiya, E., A microfluidic chip based on localized surface plasmon resonance for real-time monitoring of antigen-antibody reactions. *Jpn. J. Appl. Phys*. **2008,** *47* (2, Pt. 2), 1337-1341.
64. Live, L. S.; Masson, J.-F., Optical properties of gold particles with near micron size: localized and propagating surface plasmons. *Proc. SPIE* **2009,** *7386* (Pt. 1, Photonics North 2009), 73861M/1-73861M/7.
65. Stiles, R. L.; Willets, K. A.; Sherry, L. J.; Roden, J. M.; Van Duyne, R. P., Investigating tip-nanoparticle interactions in spatially correlated total internal reflection plasmon spectroscopy and atomic force microscopy. *J. Phys. Chem. C* **2008,** *112* (31), 11696-11701.
66. Lu, G.; Li, W.; Zhang, T.; Yue, S.; Liu, J.; Hou, L.; Li, Z.; Gong, Q., Plasmonic-Enhanced Molecular Fluorescence within Isolated Bowtie Nano-Apertures. *ACS Nano*, Ahead of Print.
67. Stranahan, S. M.; Titus, E. J.; Willets, K. A., SERS Orientational Imaging of Silver Nanoparticle Dimers. *J. Phys. Chem. Lett. 2* (21), 2711-2715.
68. Yang, S.-C.; Kobori, H.; He, C.-L.; Lin, M.-H.; Chen, H.-Y.; Li, C.; Kanehara, M.; Teranishi, T.; Gwo, S., Plasmon Hybridization in Individual Gold Nanocrystal Dimers: Direct Observation of Bright and Dark Modes. *Nano Letters 10* (2), 632-637.
69. Chang, W.-S.; Ha, J. W.; Slaughter, L. S.; Link, S., Plasmonic nanorod absorbers as orientation sensors. *Proc. Natl. Acad. Sci. U. S. A*. **2010,** *107* (7), 2781-2786, S2781/1-S2781/3.
70. Tabor, C.; Van Haute, D.; El-Sayed, M. A., Effect of Orientation on Plasmonic Coupling between Gold Nanorods. *ACS Nano* **2009,** *3* (11), 3670-3678.
71. Kaplan-Ashiri, I.; Titus, E. J.; Willets, K. A., Subdiffraction-Limited Far-Field Raman Spectroscopy of Single Carbon Nanotubes: An Unenhanced Approach. *ACS Nano 5* (2), 1033-1041.

72. Kaplan-Ashiri, I.; Titus, E. J.; Willets, K. A., Subdiffraction-Limited Far-Field Raman Spectroscopy of Single Carbon Nanotubes: An Unenhanced Approach. *ACS Nano* **2011,** *5* (2), 1033-1041.
73. Jin, R.; Cao, Y.; Mirkin, C. A.; Kelly, K. L.; Schatz, G. C.; Zheng, J. G., Photoinduced conversion of silver nanospheres to nanoprisms. *Science (Washington, DC, U. S.)* **2001,** *294* (5548), 1901-1903.
74. Quinten, M.; Pack, A.; Wannemacher, R., Scattering and extinction of evanescent waves by small particles. *Appl. Phys. B: Lasers Opt.* **1999,** *68* (1), 87-92.
75. Tian, Y.-X.; Camacho, R.; Thomsson, D.; Reus, M.; Holzwarth, A. R.; Scheblykin, I. G., Organization of Bacteriochlorophylls in Individual Chlorosomes from Chlorobaculum tepidum Studied by 2-Dimensional Polarization Fluorescence Microscopy. *J. Am. Chem. Soc.* **2011,** *133* (43), 17192-17199.
76. Traub, M. C.; Lakhwani, G.; Bolinger, J. C.; Vanden Bout, D.; Barbara, P. F., Electronic Energy Transfer in Highly Aligned MEH-PPV Single Chains. *J. Phys. Chem. B* **2011,** *115* (33), 9941-9947.
77. Sherry, L. J.; Jin, R.; Mirkin, C. A.; Schatz, G. C.; Van Duyne, R. P., Localized Surface Plasmon Resonance Spectroscopy of Single Silver Triangular Nanoprisms. *Nano Lett.* **2006,** *6* (9), 2060-2065.
78. Munechika, K.; Smith, J. M.; Chen, Y.; Ginger, D. S., Plasmon Line Widths of Single Silver Nanoprisms as a Function of Particle Size and Plasmon Peak Position. *J. Phys. Chem. C* **2007,** *111* (51), 18906-18911.
79. Heckel, J. C.; Chumanov, G., Depolarized Light Scattering From Single Silver Nanoparticles. *J. Phys. Chem. C* **2011,** *115* (15), 7261-7269.
80. Soni, J.; Purwar, H.; Ghosh, N., Quantitative polarimetry of plasmon resonant spheroidal metal nanoparticles: A Mueller matrix decomposition study. *Opt. Commun.* **2012,** *285* (6), 1599-1607.
81. Blaber, M. G.; Henry, A.-I.; Bingham, J. M.; Schatz, G. C.; Van Duyne, R. P., LSPR Imaging of Silver Triangular Nanoprisms: Correlating Scattering with Structure Using Electrodynamics for Plasmon Lifetime Analysis. *J. Phys. Chem. C* **2012,** *116* (1), 393-403.
82. Kelly, K. L.; Coronado, E.; Zhao, L. L.; Schatz, G. C., The Optical Properties of Metal Nanoparticles: The Influence of Size, Shape, and Dielectric Environment. *J. Phys. Chem. B* **2003,** *107* (3), 668-677.
83. Aherne, D.; Ledwith, D. M.; Gara, M.; Kelly, J. M., Optical properties and growth aspects of silver nanoprisms produced by a highly reproducible and rapid synthesis at room temperature. *Adv. Funct. Mater.* **2008,** *18* (14), 2005-2016.
84. Green, M. A. In *Third generation photovoltaics: assessment of progress over the last decade*, Institute of Electrical and Electronics Engineers: 2009; pp 2125-2128.
85. Seeley, A. J. A. B.; Friend, R. H.; Kim, J.-S.; Burroughes, J. H., Trap-assisted hole injection and quantum efficiency enhancement in poly(9,9' dioctylfluorene-alt-benzothiadiazole) polymer light-emitting diodes. *J. Appl. Phys.* **2004,** *96* (12), 7643-7649.

86. Yakimov, A. V.; Savvate'ev, V. N.; Davidov, D., The role of traps in polymer-based light-emitting devices. *Synth. Met.* **2000,** *115* (1-3), 51-56.
87. Salleo, A.; Street, R. A., Light-induced bias stress reversal in polyfluorene thin-film transistors. *J. Appl. Phys.* **2003,** *94* (1), 471-479.
88. Gundlach, D. J.; Jackson, T. N.; Schlom, D. G.; Nelson, S. F., Solvent-induced phase transition in thermally evaporated pentacene films. *Appl. Phys. Lett.* **1999,** *74* (22), 3302-3304.
89. Bolinger, J.; Lee, K.-J.; Palacios, R. E.; Barbara, P. F., Detailed investigation of light induced charge injection into a single conjugated polymer chain. *J. Phys. Chem. C* **2008,** *112* (47), 18608-18615.
90. Yildiz, A.; Forkey, J. N.; McKinney, S. A.; Ha, T.; Goldman, Y. E.; Selvin, P. R., Myosin V Walks Hand-Over-Hand: Single Fluorophore Imaging with 1.5-nm Localization. *Science (Washington, DC, U. S.)* **2003,** *300* (5628), 2061-2065.
91. Yu, J.; Hu, D.; Barbara, P. F., Unmasking Electronic Energy Transfer of Conjugated Polymers by Suppression of O2 Quenching. *Science* **2000,** *289* (5483), 1327-1330.
92. Hu, D.; Yu, J.; Wong, K.; Bagchi, B.; Rossky, P. J.; Barbara, P. F., Collapse of stiff conjugated polymers with chemical defects into ordered, cylindrical conformations. *Nature* **2000,** *405* (6790), 1030-1033.
93. Adachi, T.; Brazard, J.; Chokshi, P.; Bolinger, J. C.; Ganesan, V.; Barbara, P. F., Highly Ordered Single Conjugated Polymer Chain Rod Morphologies†. *The Journal of Physical Chemistry C* **2010,** *114* (48), 20896-20902.
94. Bolinger, J. C.; Fradkin, L.; Lee, K.-J.; Palacios, R. E.; Barbara, P. F.; Barbara, P. F., Light-Assisted Deep-Trapping of Holes in Conjugated Polymers. *Proceedings of the National Academy of Sciences of the United States of America* **2009,** *106* (5), 1342-1346.
95. Yildiz, A.; Forkey, J. N.; McKinney, S. A.; Ha, T.; Goldman, Y. E.; Selvin, P. R., Myosin V Walks Hand-Over-Hand: Single Fluorophore Imaging with 1.5-nm Localization. *Science* **2003,** *300* (5628), 2061-2065.
96. Gesquiere, A. J.; Park, S.-J.; Barbara, P. F., F–V/SMS: A New Technique for Studying the Structure and Dynamics of Single Molecules and Nanoparticles†. *The Journal of Physical Chemistry B* **2004,** *108* (29), 10301-10308.
97. Escalante, M.; Lenferink, A.; Zhao, Y.; Tas, N.; Huskens, J.; Hunter, C. N.; Subramaniam, V.; Otto, C., Long-Range Energy Propagation in Nanometer Arrays of Light Harvesting Antenna Complexes. *Nano Letters* **2010,** *10* (4), 1450-1457.
98. Lobez, J. M.; Andrew, T. L.; Bulović, V.; Swager, T. M., Improving the Performance of P3HT–Fullerene Solar Cells with Side-Chain-Functionalized Poly(thiophene) Additives: A New Paradigm for Polymer Design. *ACS Nano* **2012,** *6* (4), 3044-3056.
99. Lin, Y.-Y.; Chu, T.-H.; Li, S.-S.; Chuang, C.-H.; Chang, C.-H.; Su, W.-F.; Chang, C.-P.; Chu, M.-W.; Chen, C.-W., Interfacial Nanostructuring on the Performance of Polymer/TiO2 Nanorod Bulk Heterojunction Solar Cells. *Journal of the American Chemical Society* **2009,** *131* (10), 3644-3649.

100. Yu, J.; Shen, T.-L.; Weng, W.-H.; Huang, Y.-C.; Huang, C.-I.; Su, W.-F.; Rwei, S.-P.; Ho, K.-C.; Wang, L., Molecular Design of Interfacial Modifiers for Polymer-Inorganic Hybrid Solar Cells. *Advanced Energy Materials* **2012,** *2* (2), 245-252.
101. Weickert, J.; Auras, F.; Bein, T.; Schmidt-Mende, L., Characterization of Interfacial Modifiers for Hybrid Solar Cells. *The Journal of Physical Chemistry C* **2011,** *115* (30), 15081-15088.
102. Freitas, F. S.; Clifford, J. N.; Palomares, E.; Nogueira, A. F., Tailoring the interface using thiophene small molecules in TiO2/P3HT hybrid solar cells. *Physical Chemistry Chemical Physics* **2012,** *14* (34), 11990-11993.
103. Huang, Y.-C.; Yen, W.-C.; Liao, Y.-C.; Yu, Y.-C.; Hsu, C.-C.; Ho, M.-L.; Chou, P.-T.; Su, W.-F., Band gap aligned conducting interface modifier enhances the performance of thermal stable polymer-TiO2 nanorod solar cell. *Applied Physics Letters* **2010,** *96* (12), 123501.
104. Lee, M. M.; Teuscher, J.; Miyasaka, T.; Murakami, T. N.; Snaith, H. J., Efficient Hybrid Solar Cells Based on Meso-Superstructured Organometal Halide Perovskites. *Science* **2012,** *338* (6107), 643-647.
105. Liu, M.; Johnston, M. B.; Snaith, H. J., Efficient planar heterojunction perovskite solar cells by vapour deposition. *Nature* **2013,** *501* (7467), 395-398.
106. Reeja-Jayan, B.; Adachi, T.; Ono, R. J.; Vanden Bout, D. A.; Bielawski, C. W.; Manthiram, A., Effect of interfacial dipoles on charge traps in organic-inorganic hybrid solar cells. *Journal of Materials Chemistry A* **2013,** *1* (10), 3258-3262.
107. Coakley, K. M.; McGehee, M. D., Conjugated Polymer Photovoltaic Cells. *Chemistry of Materials* **2004,** *16* (23), 4533-4542.
108. Dang, X.; Hupp, J. T., Interfacial Charge-Transfer Pathways: Evidence for Marcus-Type Inverted Electron Transfer in Metal Oxide Semiconductor/Inorganic Dye Systems. *Journal of the American Chemical Society* **1999,** *121* (36), 8399-8400.
109. Ishibashi, T.-a.; Uetsuka, H.; Onishi, H., An Ordered Retinoate Monolayer Prepared on Rutile TiO2(110). *The Journal of Physical Chemistry B* **2004,** *108* (44), 17166-17170.
110. Johansson, E. M. J.; Schölin, R.; Siegbahn, H.; Hagfeldt, A.; Rensmo, H., Energy level alignment in TiO2/dipole-molecule/P3HT interfaces. *Chemical Physics Letters* **2011,** *515* (1–3), 146-150.
111. Goh, C.; Scully, S. R.; McGehee, M. D., Effects of molecular interface modification in hybrid organic-inorganic photovoltaic cells. *Journal of Applied Physics* **2007,** *101* (11), 114503.